Title
Cell Motility and Deformability in the Pathogenesis of Lung Cancer

Author
Pagano, Paul Carmelo

Publication Date
2015

Peer reviewed|Thesis/dissertation

UNIVERSITY OF CALIFORNIA

Los Angeles

Cell Motility and Deformability in the Pathogenesis of Lung Cancer

A dissertation submitted in partial satisfaction of the requirements for the degree

Doctor of Philosophy in Molecular and Medical Pharmacology

by

Paul Carmelo Pagano

2015

ABSTRACT OF THE DISSERTATION

Cell Motility and Deformability in the Pathogenesis of Lung Cancer

by

Paul Carmelo Pagano

Doctor of Philosophy in Molecular and Medical Pharmacology

University of California, Los Angeles, 2015

Professor Steven M. Dubinett, Chair

Lung cancer is the leading cause of cancer death in the United States and the world. The most effective therapy is surgical resection, but lung cancer recurs in approximately 50% of patients, most commonly as metastatic disease. This suggests that micrometastatic disease is often already present at the time of surgery, but below current levels of clinical detection. This is consistent with the reports of circulating tumor cells (CTCs) in patients with Stage I non-small cell lung cancer (NSCLC). Although metastatic behavior is often considered a late event, these clinical findings suggest that the metastatic process is also operative early in the pathogenesis of the disease. These

clinical observations are consistent with recent laboratory-based investigations indicating that dissemination may occur during early tumor development. Furthermore, recent studies implicate the genetic program associated with epithelial-mesenchymal transition (EMT) in driving early metastatic behavior during pancreatic premalignancy. Herein we demonstrate that common NSCLC-associated mutations (p53 loss and KRAS activating mutation) and over-expression of Snail, a driver of the EMT program, results in enhanced motility in non-transformed human bronchial epithelial cells (HBECs). In analyzing motility at the single-cell level, great heterogeneity in velocity was unveiled; over an order of magnitude difference between the fastest and slowest moving cell exists. Our overarching hypothesis is that there are factors attributed to highly motile cells that extend beyond speed, particularly enhanced metastasis. We developed a novel selection technique involving migration through microporous membranes, and we successfully isolated cells with the highest and lowest migratory capacity. And while it is widely believed that cell migration is a transient and stochastic event, we show the intrinsic and heritable nature of this behavior. Concomitant with changes in migration were changes in biophysical properties such as cell volume, ability to spread, and deformability. Highly migratory and deformable cells also show increased survival in a murine model of metastasis, overcoming a crucial juncture in metastatic inefficiency first described by Leonard Weiss and observed by many others in the field. At the molecular level, highly migratory cells show increased activation of Rac1, a Rho-family GTPase involved in actin polymerization and cell motility. Pharmacological inhibition of Rac1 decreases motility in highly migratory cells. Inhibition of RhoA, a negative regulator of Rac1, enhances motility in both highly migratory and non-migratory HBECs. Highly

migratory cells form fewer and smaller colonies than unselected counterparts in an anchorage-independent growth assay. However, cells within colonies formed by micropore-selected cells move rapidly, whereas cells in unselected colonies remain stationary. This corroborates a “grow or go” phenotype described by others.

Metastasis is the predominate cause of cancer death in patients, and while tumor formation is attributed to uncontrolled cell growth, metastasis is more related to aberrant cell motility and deformability. Although a tumor is made up of many cancer cells, only a small percentage of these cells are metastatic. The work included in this dissertation has important implications in determining the mechanisms behind aberrant lung epithelial cell motility in both early and late stages of the disease, and provides the foundation for future research that may lead to preventative therapeutic approaches to thwart these processes.

The dissertation of Paul Carmelo Pagano is approved.

Steven Bensinger

Dino Di Carlo

Lily Wu

Steven M. Dubinett, Committee Chair

University of California, Los Angeles

2015

DEDICATION

For my family, who have loved and supported me unconditionally.

TABLE OF CONTENTS

LIST OF FIGURES, TABLES, AND VIDEOS

Chapter Two Figures and Tables

Chapter Three Figures, Tables, and Videos

***** Videos associated with this dissertation can be found in the supplemental files section on the ProQuest website.

ACKNOWLEDGEMENT

I would like to thank Steve Dubinett for his unwavering support throughout these years. He had taken many a chance on me, and I am truly appreciative of his patience, encouragement, and support in my optimistic attempts to explore every path I encountered during my research. During the many hours we spent in his office in deep discussion, I learned how to think about biology in the context of medicine, and importantly, how to be selective with the problems I would eventually embark upon in my career as an independent investigator. I would also like to thank my committee members Drs. Steven Bensinger, Dino Di Carlo, and Lily Wu. The advice each had provided was backed by wealth of knowledge and experience and will continue to have a positive influence on my growth and development as a scientist.

To the members of the Dubinett lab past and present, whom I have seen come and go, our interactions and experiences will never be forgotten. To Elvira and Stacy, my post-doctoral mentors, thank you for your guidance and support – your influence helped me to get the most out of my graduate school experience. You both challenged me and helped make me a stronger scientist. Thank you Kostyantyn for teaching me the importance of impeccable technique, and for being supportive (and brutally honest), especially in the early days of uncertainty when I was formulating my project. Tonya, I am thankful for your and Dr. Dubinett's efforts in training me in the art of grant writing, and helping me turn my original thesis proposal into the multiple grants that helped fund my work. I am a better writer because of it and will always be grateful. Many thanks to Rui, Linh, Zhe, Brian, and Gina for offering your expertise and feedback. Thank you

Jonathan, my undergraduate student researcher, for expressing an insatiable thirst for knowledge; you have more potential than you know. Thank you for rising to any challenge I presented you, taking the initiative, and producing quality results time and time again.

Lastly, I would like to thank my friends and family. I was lucky enough to make such great friends at UCLA and will always value our times together. Thank you to my parents who have always supported me and my endeavors without hesitation. Thank you to my Sita and Nonno for stressing the importance of education, and for making much of my early eudcation possible. To my wife, Stephanie: words simply cannot express how grateful I am to have had you by my side while I accomplish this goal. Thank you for supporting me in every facet, including my late nights and weekends in the laboratory. I know you have been looking forward to my graduation as much as I have (if not more). Now that it is here, I am ready to continue our adventures together.

Chapter two is a version of: Pagano PC, Sharma S, Bendris N, O'Byrne S, Tse HT, Tran LM, Hoech JW, Park SJ, Liclican EL, Jing Z, Li R, Krysan K, Larsen JE, Gimzewski JK, Di Carlo D, Minna JD, Walswer TC, Dubinett SM. (2015) "Ex-vivo micropore selection isolates a subpopulation of lung epithelial cells with altered biophysical, molecular, and metastatic properties." Cancer Prevention Research. *In submission.* PCP conceived the ideas and performed all experiments and analyses, SS helped with atomic force microscopy, NB performed the inverted invasion assay, SOB and HTT helped with deformability cytometry, LMT helped with bioinformatic analysis, JWH helped with ImageJ analysis, SJP, ELL, RL, KK, JEL, JKG, and DC provided

intellectual support, ZJ helped with qPCR, TCW performed tail vein injections, JDM provided assistance with manuscript preparation, SMD is the principle investigator.

Research reported in this publication was supported by: NIH/NCI #T32-CA009120-36, Department of Defense Congressionally Directed Medical Research Programs #LC130767, Department of Veteran Affairs #2I01BX000359-05A1, National Center for Advancing Translational Science UCLA CTSI Grant UL1TR000124, University of California Tobacco-Related Disease Research Program #22DT-0005. The content is solely the responsibility of the author and does not necessarily represent the official views of the National Institutes of Health, Department of Defense, Department of Veteran Affairs, or the Tobacco-Related Disease Research Program.

VITA

Education

2007 Bachelor of Science, Microbiology: Immunology track (high honors)
University of California, Santa Barbara

Positions and Employment

2004-05 Laboratory Technician, Quality, Amgen, Thousand Oaks, CA
2006-07 Organic Chemistry Tutor, Campus Learning Assistance Services at UCSB
2006-07 Research Assistant, Department of Chemistry and Biochemistry at UCSB
2007-10 Research Scientist, Cynvenio Biosystems, Westlake Village, CA

Honors and Awards

2010 Project of the Year - National Institute of Electrical and Electronic Engineers
2012 NIH-NCI Tumor Immunology Training Grant
2013 UCOP, Tobacco-Related Disease Research Program Dissertation Award
2013 Molecular and Medical Pharmacology Travel Award
2014 AACR-IASLC Scholar-In-Training Award
2014 Clinical Translational Science Institute Award
2014 3rd Place Poster Competition – UCLA Department of Medicine Research Day
2014 1st Place Poster Competition – UCLA Pharmacology Annual Retreat
2015 Graduate Program in Biosciences Fellowship Award

Peer-Reviewed Publications

1. **Pagano PC**, Sharma S, Bendris N, O'Byrne S, Tse HT, Tran LM, Hoech JW, Park SJ, Liclican EL, Jing Z, Li R, Krysan K, Larsen JE, Gimzewski JK, Di Carlo D, Minna JD, Walswer TC, Dubinett SM. (2015) "Ex-vivo micropore selection isolates a subpopulation of lung epithelial cells with altered biophysical, molecular, and metastatic properties." Cancer Prevention Research. *In submission.*
2. Lee MH, Kachroo P, **Pagano PC**, Yanagawa J, Wang G, Walser TC, Krysan K, Sharma S, St. John M, Dubinett SM, Lee JM. (2014) "Combination Treatment with Apricoxib and IL-27 Enhances Inhibition of Epithelial-Mesenchymal Transition in Human Lung Cancer Cells through a STAT1 dominant pathway." J of Can Sci and Ther. 6:468-477
3. Liclican EL, Walser TC, Hazra S, Krysan K, Park SJ, **Pagano PC**, *et al*. (2014). "Loss of miR125a Expression in a model of K-Ras Dependent Pulmonary Premalignancy." Can Prev Res 7(8) 845-855.
4. Winter-Jones JP, Vahidi B, Arquilevich N, Fang C, Ferguson S, Harkins D, Hill C, Klem E, **Pagano PC** *et al* (2014). "Circulating Tumor Cells: Clinically relevant molecular access based on a novel CTC flow cell." PLoS One 9(1): e86717.
5. Krysan K, Cui X, Gardner BK, Reckamp KL, Wang X, Hong L, Walser TC, Rodriguez NL, **Pagano PC**, Garon EB, Brothers JF, Elashoff D, Spira AE, Sharma S, Fishbein MC, Dubinett SM. (2013) "Elevated neutrophil gelatinase-associated lipocalin contributes to erlotinib resistance in non-small cell lung cancer." Am J Transl Res 5:481-96.
6. Kogot, JM, Zhang Y, Moore SJ, **Pagano P**, *et al*. (2011). "Screening of Peptide Libraries against Protective Antigen of Bacillus anthracis in a Disposable Microfluidic Cartridge." PLoS One 6(11): e26925.

Meeting Abstracts

1. **Pagano PC**, et al. (2014) Novel Methodologies to elucidate heterogeneity and overcome metastatic inefficiency in human bronchial epithelial cells [abstract]. In: UCLA Department of Medicine Research Day – October 11; Los Angeles, CA.
2. **Pagano PC**, *et al*. (2014) Novel Methodology to elucidate heterogeneity in oncogene-modified human bronchial epithelial cells [abstract]. In: SPORE Lung Cancer Workshop; July 25-26; Rockville, MD. Philadelphia.

3. **Pagano PC**, *et al*. (2014) Cell Motility and Deformability in the Pathogenesis of Lung Cancer [abstract]. In: Proceedings of the AACR-IASLC Joint Conference on The Molecular Origins of Lung Cancer; Jan 6-9; San Diego, CA. Philadelphia (PA): AACR Clin Cancer Res; 20(2Suppl): Abstract B15.
4. **Pagano PC**, *et al*. (2013) Cell Motility and Deformability in the Pathogenesis of Lung Cancer [abstract]. In: UCLA Department of Medicine Research Day – October 5; Los Angeles, CA.
5. **Pagano PC**, Sharma S, Tse HT, O'Byrne S, et al. (2013) Cell Motility and Deformability in the Pathogenesis of Lung Cancer [abstract]. In: Gordon Research Conference: Motile and Contractile Systems Biannual Meeting -- July 27-Aug 2; New London, NH. Abstract #B20
6. Zhang Y, Qian J, **Pagano P**, *et al*. (2008) Separation and enrichment of rare cells from peripheral blood using a microfluidic magnetic cell sorter [abstract]. In: Proceedings of the 99th AACR Annual Meeting-- Apr 12-16; San Diego, CA: AACR. Abstract #465.

Patents

1. **Pagano P**, Zhang Y, Qian J, Soh HT, Dempsey P, de Fusco A. Sheath flow devices and methods. US Patent #8,263,387. Issued September 11, 2012.
2. Chang-Yen D, Darabi J, Zhang Y, **Pagano P**, Gluck F. Magnetic separation system with pre and post processing modules. US Patent Application #2011/0137018 A1. Published June 9, 2011.
3. Turewicz M, **Pagano P**, de Fusco A, Sauvageau D. Flexible pouch and cartridge with fluidic circuits. US Patent Application #2010/0317093 A1. Published December 16, 2010.
4. Chang-Yen D, Darabi J, Zhang Y, **Pagano P**, Soh HT. Trapping magnetic sorting system for target species. US Patent Application #2009/0053799 A1. Published February 26, 2009.

Ongoing Research Support

22DT-0005 Dissertation Award — Pagano (Mentored PI) — 08/01/13-07/31/15
UCOP Tobacco-Related Disease Research Program
Cell Motility in the Pathogenesis of Lung Cancer

LC130767 — Dubinett — 09/01/14-08/31/15
Department of Defense – Congressionally Directed Medical Research Program
Epithelial Cell Deformability in Pulmonary Premalignancy

2I01BX000359-05A1 — Dubinett — 04/01/14-03/31/19
NIH – Veterans Affairs (VA) Merit Review
Cell Motility in the Pathogenesis of Lung Cancer

Pending Research Support

PAR-14-168 (application 7701) — Di Carlo/Dubinett — 04/01/15-03/31/20
NIH/NCI
Physical Sciences Oncology Network – Physical Sciences Oncology Center
UCLA Center for Translational Cancer Physomics. The goal is to bring technologies and biomarkers that leverage physical properties of cells, including motility and deformability, to practice in the clinic.

Completed Research Support

T32-CA009120-36 — Dubinett — 06/01/13-07/31/13
NIH-NCI
Ruth L. Kirschstein NRSA - Tumor Immunology Training Grant
Cell Motility and Deformability in the Pathogenesis of Lung Cancer

T32-CA009120-36 — Dubinett — 06/01/12-05/31/13
NIH-NCI
Ruth L. Kirschstein NRSA - Tumor Immunology Training Grant
Mechanisms of Erlotinib Resistance in Non-Small Cell Lung Cancer

CHAPTER ONE: A review of the literature

Lung Cancer and Premalignancy

The estimated new cases of lung cancer exceeded 224,000 in 2014, and the five year relative survival rate has increased meagerly from 11.4% in 1975 to 17.5% in 2007 (1,2). This is in part due to the lack of early detection and the fact that early stage disease is typically asymptomatic (only 15% of cases are diagnosed at early stage). As such, the majority of cases are caught in the later stages of disease when sufficient time to form large metastases has passed (3). While recent reports show a 20% reduction in lung cancer mortality as a result of low-dose CT screening in high-risk individuals (4,5), much work remains in stopping this deadly disease.

Lung cancer is divided into two types: small-cell lung cancer and non-small cell lung cancer (NSCLC), the latter of which accounts for greater than 85% of all cases. The information in this chapter, as well as the work discussed in this dissertation, relate to NSCLC. NSCLC is divided into three subtypes: adenocarcinoma, squamous cell carcinoma, and large cell carcinoma, all which have unique histological characteristics. Historically, treatment for lung cancer was based on the pathology of the tumor (6). While the cells of origin for these cancer types are under debate, it is known that adenocarcinomas and large cell carcinomas typically arise in the lung periphery, whereas squamous cell carcinomas typically arise in the central airway (7). Adenocarcinoma and squamous cell carcinoma, the two major subclasses of NSCLC, are typically differentiated by morphological criteria and immunohistochemistry, which aids in tailoring therapy (8,9). For example, bevacizumab improves survival in patients with adenocarcinoma; however, the drug is contraindicated for squamous cell carcinoma due to risk of pulmonary hemorrhaging (10). However, challenges do exist in

the morphological classification of lung tumors: tumors can present as having mixed subtypes, or as being poorly differentiated. As such, identification of molecular aberrations can be helpful in guiding a treatment strategy.

Great strides have been made in recent years in characterizing the genetic and molecular landscape of NSCLC, particularly with respect to the identification of mutations in oncogenes and tumor suppressors, as well as their associated pathways (11,12). For example, identification of mutations in epidermal growth factor receptor (*EGFR*) or gene rearrangements in anaplastic lymphoma kinase (*ALK*) and *RET* have led to new therapies that have had a dramatic impact on patient survival. However, it stands that the majority of lung cancers lack a known driver oncogene, or harbor mutations in genes that are common but currently not clinically actionable, such as in *KRAS* mutant lung cancers. In addition, resistance to targeted therapy is a constant battle. Resistance to treatment with gefitinib or erlotinib, first line treatments for lung cancers with known *EGFR* mutations, has been shown to occur by a variety of mechanisms, including secondary mutations in the *EGFR* kinase domain (T790M) or *MET* amplification (13-16). Although we have greatly expanded our knowledge of the molecular makeup of NSCLC, another confounding factor contributing toward its devastating disposition is our lack of understanding of the natural history of the disease, beginning with premalignancy.

Lung premalignancy is defined as the stepwise pathological progression and accompanying molecular alterations of otherwise histologically normal epithelium to hyperplasia, metaplasia, dysplasia, and carcinoma *in situ* (7,17), which are collectively

known as premalignant lesions. And while some of the genetic and molecular alterations have been defined at these various stages, including loss of the tumor suppressor *P53*, telomerase deregulation, and loss of expression of various cell cycle checkpoint factors, there is no set of defining features that will with high predictive value confirm which lesion will progress to frank malignancy. Uncertainties about the clinical behavior of premalignant lesions can lead to either inappropriate inaction or inappropriately aggressive treatment, both of which can result in harm to the patient. This is related to the fact that targeting premalignancy in lung is more complicated than in other more physically accessible tissues such as the skin, breast, or colon. Preliminary studies have been performed which look more deeply at the molecular events associated with progression of lung premalignant lesions through sequencing of laser-capture microdissected histologically-normal lung and premalignant lesions from the same specimen (18); however, much work remains to be performed to help determine what cellular and molecular events in early lesions will result in progression to invasive carcinoma. Because these lesions are challenging to track *in situ* longitudinally, human bronchial epithelial cells (HBECs) represent an attractive model for *in vitro* and *in vivo* studies.

HBECs serve as a preclinical model of early lung cancer pathogenesis, and they allow us to answer many questions that cannot be addressed in the context of studies with established lung cancer cells. HBECs isolated from patients who are at risk for lung cancer have been immortalized in the absence of viral oncoproteins using ectopic expression of human telomerase and cyclin-dependent kinase 4, two genetic aberrations that are characteristic of most premalignant lung lesions (19,20). At

baseline, HBECs are non-tumorigenic and closely resemble normal airway epithelium at histological and molecular levels. With the step-wise addition of *P53* silencing and *KRAS* activating mutations (HBEC-P53/KRAS), these cells more closely resemble at-risk epithelium (21). Work in our lab and others have described the genetic program of epithelial-mesenchymal transition at play in early lesions. With the subsequent addition of the EMT transcription factor Snail (HBEC-P53/KRAS/Snail), these cells acquire anchorage-independent growth (AIG) *in vitro* and give rise to tumors and metastases *in vivo* (22,23).

Epithelial-Mesenchymal Transition in Development and Cancer

Epithelial-mesenchymal transition (EMT) is a program first described in development as a process whereby epithelial cells, normally interacting with adjacent cells and a basement membrane, undergo a series of biological changes that lead to a more fibroblast- or mesenchymal-like phenotype, including loss of cell-cell contacts, dissolution of polarity, increased migration, and differentiation, which is fully reversible via mesenchymal-epithelial transition (MET). And while the majority of knowledge pertaining to EMT comes from studies in developmental biology, the focus of this section will be on EMT in adult tissue and in the context of disease, with only brief references to developmental processes. Snail and Twist family transcription factors are direct repressors of E-cadherin transcription, are critical to EMT, and many developmental processes do not occur in their absence (24). EMT in development involves both the migration and differentiation of cells. Migration of cells is regulated through various Rho family GTPases, which will be discussed in detail later on. Cell

differentiation occurs in response to factors in the microenvironment that allow for a more restricted differentiation program resulting in unique cell types. These factors include hepatocyte growth factor (HGF), fibroblast growth factor (FGF), and transforming growth factor beta (TGFß), and their signaling will eventually result in the formation of various organ systems (25,26). It is important to state that while epithelial migration and differentiation are critical in development, they are activated in few physiological processes in healthy adult tissue, such as in response to injury. During wound healing, keratinocytes at the border of the wound undergo a partial EMT, which allows them to migrate collectively with nearby cells in a *SNAI2*-dependent manner (27).

EMT plays an important role in cancer. Kalluri and Weinberg define three types of EMT: type 1, related to development, type 2, with wound healing, and type 3, with metastasis from tumors (28). Many of the signals that initiate and maintain EMT in development are also present in cancer-associated inflammation, such as TGFß, HGF, EGF, PDGF and IL-1ß (29,30). The factors induced by this signaling, including Snail, Slug, Twist, Zeb, Goosecoid, and FOXC2, are responsible alone or in concert to implement the EMT program, encompassing intricate relationships among transcriptional, translational, and epigenetic mechanisms (31).

Cell invasion and metastatic progression are hallmarks of cancer that are typically considered to be mediated by EMT and associated with late stage disease (28,32,33). Recent studies reveal that in addition to invasiveness, up-regulation of members of these transcriptional repressor families mediates a variety of important tumor-initiating and -promoting characteristics, including expansion of stem cell

phenotypes, angiogenesis, and apoptosis resistance (34). As per the “linear progression model,” EMT only occurs in rare cells at the leading invasive edge of advanced cancers, facilitating the final step in tumor progression (metastasis). Recently, several groups have demonstrated that EMT also drives malignant transformation and early dissemination in epithelial malignancies, including tobacco-related cancers (35-37). Furthermore, it was recently proposed that EMT promotes dissemination of lung epithelial cells prior to, or concomitant with, their malignant conversion (38). This process, now termed “the parallel progression model”, was highlighted by Sanchez-Garcia in the New England Journal of Medicine because it represents a paradigm shift in terms of our understanding of lung cancer development, progression, and metastasis. Most importantly, the parallel progression model represents a more accurate model of the clinical observation that 50% of patients with early stage lung cancer undergoing surgery return with metastatic disease, indicating that undetected micrometastatic disease was already present at the time of surgery. The mechanisms underlying EMT-driven parallel progression in the setting of lung cancer have not yet been determined.

Cell Polarity and Molecular Mechanisms in Motile Cells

While a variety of cell types necessitate movement at various points in developing and adult tissues, this review will focus on adult epithelial cells. With the exception of an EMT, normal epithelial cells are relatively stationary *in situ*, bound by neighboring cells and the basement membrane (28). Here, the cellular surface that interfaces with the external environment is called the “apical” surface, and the “basal” surface interacts with the basement membrane. This type of organization is known as

apical-basal polarity, and allows for directional transport of nutrients, ions, and waste products in and out of the body (39,40). In physiologically normal epithelium, bronchial epithelial cells are expected to remain rather stationary. However, in the instance of insult to the epithelium, epithelial cells have the potential to undergo cell death, thus leaving a gap in the cell layer. Vaughan *et al* show that a rare population of epithelial cells within the murine lung possessing progenitor capacity can migrate to the site of injury and repopulate the epithelium, thus filling the gap (41). Although not stated outright, it is likely that these cells initially transition to a different type of polarity, called "front-rear" polarity, during transit, and upon arrival switch back to apical-basal polarity in order to integrate and recreate a functional epithelium. This alternative form of polarity was first described *in vitro* in the context of motile cells in two dimensions, in which cells have a leading "front" edge, where intense actin polymerization takes place, and a trailing "rear" edge, where actomyosin contractility dominates to retract the rear (42).

The translocation of cells, whether in two or three dimensional space, is broadly defined as cell motility. For movement of cells to occur, polymerization of globular actin subunits into filamentous actin in spatially advantageous regions of the cell must transpire, such that any force generated by the filamentous actin on the cell membrane can be used for expansion of the cell membrane in the direction of actin polymerization (43). The expansion of multiple branched actin filaments away from the cell body creates a large "foot-like" structure at the leading edge of the cell known as the lamellipodium, which is a flat, thin protrusion mainly composed of polymerized and highly branched actin. Actin dynamics, the processes by which actin is polymerized, de-

polymerized, cleaved, cross-linked and otherwise structurally altered requires a multitude of factors, and it may be helpful to describe this process beginning with the molecular switches that regulate motility.

Rho family GTPases comprise 22 characterized members including RhoA, Rac1, and Cdc42, which are the best described. Collectively they act as molecular switches, cycling between the GTP-bound active state, and GDP-bound inactive state (44). It is in the GTP-bound active state that these GTPases can influence motility via a variety of effectors through binding-induced conformational changes. For example, RhoA-GTP binds Rho-associated kinase (ROCK) and Rac1-GTP or Cdc42-GTP bind p21-activated kinase (PAK), which then convey regulatory signals through phosphorylation of various downstream targets (45,46). Rac1 and Cdc42 drive actin polymerization through different Wiskott-Aldrich Syndrome Family Proteins (WAVE and WASP), which eventually activate the Arp2/3 complex. Arp2/3 has an actin binding domain that binds the fast growing end of an actin filament (barbed end) and can facilitate actin branching by introducing a new platform for globular actin to nucleate at a 70 degree angle to the original filament (actin branching) (47). Formin proteins mDia1 and mDia2, which bind the barbed-end of actin filaments, sequester profilin-bound actin subunits, serially adding them to the growing filament. As stated previously, polymerization of filaments with Arp2/3-mediated branching leads to the Rac1-dependent generation of lamellipodia, a structure involved in cell propulsion. Polymerization of filaments against the membrane in the absence of Arp2/3-mediated branching leads to the Cdc42-dependent generation of filopodia, structures that are involved in probing the extracellular environment and cell attachment (43). Filament elongation can be stopped

by non-severing capping proteins, which compete for filament binding with formins (48). Branching of filaments occurs with the help of actin depolymerization factor/cofilin (ADF/cofilin), which severs actin filaments and allows the binding of the Arp2/3 complex and subsequent polymerization in a branched fashion. This process is crucial for lamellipodium formation, which is orchestrated through Rac1 pathway activation. While Cdc42 and Rac1 are responsible for motile force due to actin polymerization and the production of filopodia and lamellipodia, respectively, activation of the RhoA pathway leads contractility-related force through actin stress-fiber formation (42). Stress fibers are composed of bundles of actin filaments and are associated with actin binding proteins and myosins (49). RhoA-GTP activates ROCK and myosin light chain kinase (MLCK), which facilitate phosphorylation of myosin regulatory light chain 2a (MLC2a). This is the dominant non-muscle myosin which when phosphorylated is activated for actomyosin contractility. Ventral stress fibers in a migrating cell terminate at focal adhesions, basal membrane-proximal multi-protein complexes that connect the cytoskeleton to the extracellular environment (50). RhoA pathway activation is also important in cell body contraction and retraction of the trailing edge of the cell, controlled by MLC2a-mediated contraction, which allows the cell to move forward.

Regulation of the actin cytoskeleton has evolved in such a way to rapidly respond to stimuli. Hesitation would result in immune cells inefficiently clearing a microbial infection, or epithelial cells incompetently closing a wound. As such, there is little currently known about transcriptional regulation of various cytoskeletal components (51). Simple polymerization of actin can release transcription co-factors to the nucleus, such as myocardin-related transcription factor (MRTF) cofactors, and allow transcription

of genes involved in cell motility regulation, including capping proteins and GTPase activating proteins (52,53). However, much of what is known about regulation is based on post-translational modifications, and enzymatic or scaffolding functions of various actin binding proteins. As mentioned previously, GTPases are the major regulators of actin dynamics, and their activity is regulated by exchange of GDP for GTP by guanine nucleotide exchange factors (GEFs) and GTP hydrolysis by GTPase activating proteins (GAPs). As activators of GTPases, GEFs are found downstream of cytokine and growth factor receptors, cell adhesion molecules, and integrins (54). Phosphorylation commonly regulates components of the actin cytoskeleton. For example, cofilin severs actin filaments. Upon phosphorylation by LIM kinase, severing ability is abolished due to inability to bind F-actin (55). Lipidation can also regulate various proteins involved in actin dynamics, including the Rho family GTPases themselves (56). Farnesyltransferase and geranylgeranyl isoprenoid transferase add farnesyl or geranyl lipids, respectively, to cysteine residues of various Rho family members, leading to increased hydrophobicity and their association with the lipid membrane. Without membrane localization, Rho will remain inactive in the cytosol (57).

Biophysical cells: Matrix stiffness, cellular deformability and confinement

Cell movement, including tumor cell metastasis, is largely facilitated through interaction with the extracellular matrix (ECM), which is the environment in which a cell interacts. The ECM is composed of fibrous proteins (collagen, and elastin) and glycoproteins (fibronectin, laminin, and proteoglycans) (58). The ECM provides a physical support for cells, as well as provides boundaries for various tissues and

organs. The composition of the ECM can vary depending on the physiological role or state of the tissue. Annoni *et al* determined that the ECM composition of patients with chronic obstructive pulmonary disease (COPD) contained fewer elastic fibers in all lung compartments compared to non-obstructed smokers and non-smoking individuals (59). As a result of the differing composition, different ECM stiffness profiles are obtained, which in the context of metastatic behavior has implications in cell motility and migration. Cells will migrate towards stiffer material when plated on a gradient of increasing stiffness, a process known as “durotaxis” (60,61). Many of the original findings related to durotaxis use 2-dimensional substrates; however, the environments a cell will encounter *in situ* are more often than not 3-dimensional matrices. So in addition to crawling along a gradient of increasing rigidity, cells must also posses deformability characteristics that will allow them to traverse confined space on the order of microns (62,63).

Cellular deformability is a property related to the elasticity and flexibility of a cell under load. Studies of cancer cell deformability date back to Leonard Weiss in 1965, where micropipette aspiration was used to determine the pressure required to deform a cell membrane (64). Growing evidence supports correlations between deformability and metastatic potential, cell cycle, and stem cell differentiation state (65-68). Multiple factors play a role in how deformable a cell is, including the cytoskeleton, nuclear architecture, and membrane composition.

The cytoskeleton is composed of actin filaments, intermediate filaments, and microtubules. Actin filaments, in conjunction with bundling proteins, form a dynamic

meshwork that provides the cell with mechanical stability (69). Gardel *et al* found that the mechanical stiffness can vary by several orders of magnitude with small changes in actin filament cross-linking concentration, and that upon application of an external stress, the amount of cross-linking can increase rapidly (70). Intermediate filaments include cytokeratins and vimentin, among others. Together with actin filaments, they have the largest contribution to overall cellular stiffness (71). Studies have shown that vimentin increases cellular stiffness, and stiffening occurs in response to applied stress *in vitro* (72). The nuclear lamins are distinct class of intermediate filaments, which will be discussed later. While actin filaments play a critical role in directly driving motility, as described earlier, microtubules are the unsung hero in motility and structural integrity of the cell. Microtubules are a hollow polymer composed of a helical distribution of alpha- and beta-tubulin subunits, and are canonically involved in transport of vesicles and macromolecules across the cell via dynein and kinesin motors. In a migrating cells, microtubules orient in the direction of movement, with the microtubule organizing center in front of the nucleus, as to provide factors necessary for actin polymerization rapidly. The bending stiffness, or resistance to bending deformation, of microtubules is over 100-fold compared to actin filaments (73). Microtubules appear to buckle when viewed in cells, suggesting they are under periodic compressive load, and studies have shown they can and do withstand large forces through reinforcement with the elastic cytoskeleton (74).

The nucleus contributes in different ways to overall cell stiffness, including nuclear size and membrane composition. Recent work by Wolf *et al* suggests that migration declines as a linear function of constriction size and with deformation of the

nucleus, with migratory arrest reached at ~10% of the nuclear cross section (7 μm^2, or 3 μm pore diameter for tumor cells) (75). They suggest that maximum compressibility is an absolute value (~10% of the nuclear cross section) irrespective of cell type, constitutive nuclear shape (including the multi-lobular nuclei of neutrophils), or nuclear rigidity. The authors also suggest a non-compressible intranuclear component (chromatin) in defining compression maximum and the physical limits of cell migration. Chromatin in the interphase nucleus can be loosely packaged in such a way that allows facile gene transcription (euchromatin) or densely packaged (heterochromatin), which typically contains inactive genes. Girlitz and Bustin published findings that upon induction of migration, the nucleus shrinks in size concomitant with the alteration of chromatin architectural proteins HMGN2, HMGA1 and histone H1, and further that preventing chromatin condensation resulted in decreased migration (76). Thus, cells with greater chromatin compaction have enhanced migration through constrictive space compared to cells with a lesser degree of compaction. Others show in addition to nuclear size and chromatin compaction, nuclear composition plays a role in successful migration. A major protein component of the nucleus is the nuclear lamina, and is composed of a type of intermediate filament called lamin. There are seven lamin splice variants derived from three genes: A-type lamins (Lamin-A, AΔ10, C and C2) are derived from alternative splicing of the *LMNA* gene, and B-type lamins (Lamin B1, B2-B3) are derived from *LMNB1* and *LMNB2* genes, respectively (77). Lamins are involved in DNA synthesis, transcription, and apoptosis, and it is the main structural component that gives the nucleus its shape (78). Rowat *et al* has determined that the composition of the nuclear lamina (Lamin A levels) and not the lobular shape of neutrophil nuclei is

critical for migration through micron-scale constrictions (79). Similarly, work from the Discher and Lammerding labs have shown that the Lamin A:B stoichiometry in various cell types contributes to migration through micropores: cells with high Lamin A migrate poorly; however, cells with too little Lamin A migrate well, but fail to survive which authors contribute to mechanical stress (80,81). These results suggest that in addition to nuclear size and chromatin compaction, nuclear lamina composition is a rate limiting factor for successful migration through constrictive space.

It was originally determined that the single most influential molecule affecting deformability of lipid membranes is cholesterol, and that addition of cholesterol to lipid bilayers increased stiffness (82). However, Byfield *et al* determined that methyl-beta-cyclodextrin-mediated depletion of cholesterol in bovine arterial cells increased cellular stiffness when measured by micropipette aspiration (83). While the depletion of membrane cholesterol resulting in increased stiffness challenges previously held beliefs, Hissa *et al* later went on to show that cholesterol depletion led to changes at the membrane-cytoskeleton interface, including stress fiber formation and actin polymerization/reorganization, all mediated by RhoA (84). Because micropipette aspiration cannot differentiate between stiffness due to membrane composition and stiffness due to changes in membrane-cytoskeleton interaction, Yang *et al* performed depth-sensing nano-indentation on cholesterol depleted/restored 3T3 membranes, which exclusively measures the membrane of live cells at a 20 nm analysis depth, and found that cholesterol depletion indeed makes membranes less stiff (85). There are implications for membrane fluidity, and likely lipid content, in cancer metastasis. In resected lung tumor specimens, analysis by electron paramagnetic resonance of

lipophilic-spin probe labeled membranes showed a negative correlation between plasma membrane fluidity and patient survival (86), and others have had corroborative results in mouse models (87,88). Recently, Edmond *et al* determined that down-regulation of ceramide synthase-6 occurs during EMT, which increases membrane fluidity by reducing the amount of C16:0 sphingomyelin in the plasma membrane (89). Sphingomyelin is known to decrease cell membrane fluidity, and so its absence leads to increased cell motility and migration; although a crucial next step for this study in particular would be to show activity in a murine model of metastasis. Membrane fluidity and deformability differ substantially, and their relationship to one another is currently ill defined. A firm appreciation of this relationship and connection to migration could have substantial effects on our understanding of metastasis.

Cell deformability can be measured by multiple techniques, including micropipette aspiration, magnetic twisting cytometry, optical tweezers stretching, and hydrodynamic stretching. Each takes into account different compartments of the cell (membrane, cytoskeleton, nucleus) and each has benefits and limitations. This review will touch on atomic force microscopy (AFM) and hydrodynamic stretching. AFM is a technique that probes individual cells using a micro-cantilever with a tip that glides over the cell surface (contact mode) (90). Deflection of the cantilever caused by differences in cell rigidity is measured by changes in deflection of laser light that is reflected off the tip of the cantilever onto a photodiode. The force required to maintain constant deflection over the cell surface is related to cellular elasticity. Work from the James Gimzewski lab and others have made extensive contributions to our understanding of mechanical stiffness in the context of metastatic potential and drug resistance using

AFM (91-93). These studies show that metastatic cells tend to be less stiff than non-metastatic ones, and that cisplatin-sensitive cancer cells show a dose-dependent increase in stiffness. While AFM is useful for measuring the contribution of membrane and cytoskeletal components to deformability, it is a low throughput method (one cell per minute) (94). Recently, a microfluidic-based hydrodynamic stretching technique, called deformability cytometry (DC), was developed at UCLA by Dino Di Carlo. This technique uses hydrodynamic forces to stretch cells uniformly in a microfluidic chip followed by high-speed imaging to discern changes in cell shape and size as a result of applied stress (94). Deformability (D) is a unitless measure defined as the maximum ratio of the long to short axis of a cell stretched with a standard stress, such that a cell with a lower stiffness will have a corresponding higher deformability. Deformations are recorded by a high-speed camera (500,000 frames per second) and image analysis programs report cell size and deformability. This method is capable of measuring several thousand cell deformations per second and is useful for distinguishing epigenetic changes, such as chromatin modification and nuclear architecture alterations (94), and has recently been used to diagnose malignant plural effusions (95). While it is high throughput and analyzes cells at the single cell level, it currently lacks the ability to measure cells while adherent and migrating. As mentioned previously, cell deformability has been correlated to the metastatic potential of cancer (65,92,96); lines with high metastatic potential are typically more deformable. However, the clinical observation that most cells attempting to cross the endothelial barrier succumb to shearing (97) implies that some level of rigidity is still required for survival. This suggests there is more to this story that we do not fully understand.

As mentioned briefly before, the mechanical properties of cells have also been correlated with malignancy. Work by Guck *et al* showed optically-induced surface forces that lead to trapping and stretching of single cells (optical stretching) was sensitive enough to monitor the subtle changes during malignant progression in both murine and human models of carcinogenesis (96). They determined that non-transformed tissue (mouse fibroblasts and human breast cells) were less deformable than fully transformed counterparts. Furthermore, work from the Guck group later showed that optical stretching could be used to differentiate normal versus malignant cells from patients with oral squamous cell carcinoma (98). Researchers have found that high deformability is a characteristic of tumor-initiating cells (TICs), cells capable of repopulating a tumor, within cancer cell lines (99). Specifically, utilizing a microfabricated device that uses barriers of decreasing permeability, breast cancer cells in suspension were sorted by deformability and analyzed for TIC properties, including CD44/CD24 expression and mammosphere formation. Significant limitations of this study were that the cells had already undergone transformation and that the cells did not pass through the barriers on their own accord (passive deformability), the latter being a property that is likely critical for passing the endothelial barrier. Questions remain on how active deformability relates to the TIC phenotype and how they relate to metastasis.

Recent studies by Hung *et. al.* provide a strong rationale to study deformability and motility in concert; cells migrating in confined channels utilize different signaling mechanisms from those in unrestricted spaces. In unconfined space, cells utilize Rac1-mediated mechanisms for motility. In confined space, Rac1 is inhibited through α4β1 integrins, which allows for RhoA-mediated myosin IIa contractility (100). It has been

suggested that these confined spaces are more physiologically relevant for assessment of migration (101) and thus metastatic behavior. Others have found that confinement of cells results in enhanced motility (102,103). In the absence of focal adhesions, mesenchymal cells under confinement can switch to fast amoeboid-type motility by two distinct processes: one involving a local protrusion and a second involving myosin-II-dependent mechanical instability of the cell cortex that leads to global cortical flow (104). Future work should attempt to recapitulate these observations in a context-specific manner *in vivo* (i.e. disease state or tissue location), perhaps by using intravital 2-photon microscopy. These studies will more fully materialize the impact of this work on our understanding of cell migration in development and disease.

Significance

Metastasis is the underlying cause of greater than 90% of cancer-related suffering and mortality (105). However, the inhibition of tumor growth remains the focus of therapeutic strategy and there are no FDA approved drugs that prevent metastasis (106). While the formation of a tumor is a problem of uncontrolled cell growth, metastasis is a problem of uncontrolled cell motility (107). Part of the problem is our lack of understanding of what drives movement in the human adult epithelium, a tissue that otherwise should be non-motile. While the vast majority of studies related to metastatic behavior involve tumor cells, we hypothesize that cells representative of lung premalignant lesions also have the capacity to move.

The physical properties of velocity and deformability in the context of EMT, cancer initiation and progression, and early metastatic dissemination have not been directly explored due to our previous lack of a reliable means to isolate and subsequently characterize cells based on these properties: there is an incredible amount of heterogeneity with respect to behavioral and biomechanical properties amongst otherwise homogenous cell populations. An initial description of how motility drives metastatic behavior of pulmonary lesions is desperately needed in order to direct therapeutics towards the rare but lethal metastatic cell subpopulation.

The natural history of pulmonary premalignancy and progression to lung cancer remain obscure. The information in this dissertation extends the histological studies of premalignancy that Auerbach began 50 years ago (108) by beginning to define the underlying molecular determinants of enhanced motility that characterizes a subset of

premalignant pulmonary epithelial cells. In the long-term, this research will contribute to establish definable properties of pulmonary premalignant lesions that predict the likelihood of progression to lung cancer and early dissemination. Translation of these results could profoundly change the way in which we address the clinical problem of the individual at high risk for lung cancer or the patient at risk for recurrence of the disease following surgery. Discovery of the molecular determinants of cell motility in early stage lung cancer pathogenesis could lead to the development of agents that target the metastatic phenotype in patients at risk in the perioperative period.

References

1. DeSantis CE, Lin CC, Mariotto AB, Siegel RL, Stein KD, Kramer JL, Alteri R, Robbins AS, Jemal A. Cancer treatment and survivorship statistics, 2014. CA Cancer J Clin 2014;64(4):252-71.

2. Siegel R, Ma J, Zou Z, Jemal A. Cancer statistics, 2014. CA Cancer J Clin 2014;64(1):9-29.

3. Howlader N, Noone A, Krapcho M, Garshell J, Miller D, Altekruse S, Kosary C, Yu M, Ruhl J, et al. SEER Cancer Statistics Review, 1975-2011, National Cancer Institute. Bethesda, MD. 2013.

4. National Lung Screening Trial Research T, Aberle DR, Adams AM, Berg CD, Black WC, Clapp JD, Fagerstrom RM, Gareen IF, Gatsonis C, et al. Reduced lung-cancer mortality with low-dose computed tomographic screening. N Engl J Med 2011;365(5):395-409.

5. National Lung Screening Trial Research T, Church TR, Black WC, Aberle DR, Berg CD, Clingan KL, Duan F, Fagerstrom RM, Gareen IF, et al. Results of initial low-dose computed tomographic screening for lung cancer. N Engl J Med 2013;368(21):1980-91.

6. Kris MG, Johnson BE, Berry LD, Kwiatkowski DJ, Iafrate AJ, Wistuba, II, Varella-Garcia M, Franklin WA, Aronson SL, et al. Using multiplexed assays of oncogenic drivers in lung cancers to select targeted drugs. Jama 2014;311(19):1998-2006.

7. Wistuba, II, Gazdar AF. Lung cancer preneoplasia. Annu Rev Pathol 2006;1:331-48.

8. Rekhtman N, Ang DC, Sima CS, Travis WD, Moreira AL. Immunohistochemical algorithm for differentiation of lung adenocarcinoma and squamous cell carcinoma based on large series of whole-tissue sections with validation in small specimens. Modern pathology : an official journal of the United States and Canadian Academy of Pathology, Inc 2011;24(10):1348-59.

9. Aisner DL, Marshall CB. Molecular pathology of non-small cell lung cancer: a practical guide. American journal of clinical pathology 2012;138(3):332-46.

10. Hellmann MD, Chaft JE, Rusch V, Ginsberg MS, Finley DJ, Kris MG, Price KA, Azzoli CG, Fury MG, et al. Risk of hemoptysis in patients with resected squamous cell and other high-risk lung cancers treated with adjuvant bevacizumab. Cancer chemotherapy and pharmacology 2013;72(2):453-61.

11. Cancer Genome Atlas Research N. Comprehensive genomic characterization of squamous cell lung cancers. Nature 2012;489(7417):519-25.

12. Cancer Genome Atlas Research N. Comprehensive molecular profiling of lung adenocarcinoma. Nature 2014;511(7511):543-50.

13. Lynch TJ, Bell DW, Sordella R, Gurubhagavatula S, Okimoto RA, Brannigan BW, Harris PL, Haserlat SM, Supko JG, et al. Activating mutations in the epidermal growth factor receptor underlying responsiveness of non-small-cell lung cancer to gefitinib. N Engl J Med 2004;350(21):2129-39.

14. Pao W, Miller VA, Politi KA, Riely GJ, Somwar R, Zakowski MF, Kris MG, Varmus H. Acquired resistance of lung adenocarcinomas to gefitinib or erlotinib is associated with a second mutation in the EGFR kinase domain. PLoS Med 2005;2(3):e73.

15. Engelman JA, Zejnullahu K, Mitsudomi T, Song Y, Hyland C, Park JO, Lindeman N, Gale CM, Zhao X, et al. MET amplification leads to gefitinib resistance in lung cancer by activating ERBB3 signaling. Science 2007;316(5827):1039-43.

16. Krysan K, Cui X, Gardner BK, Reckamp KL, Wang X, Hong L, Walser TC, Rodriguez NL, Pagano PC, et al. Elevated neutrophil gelatinase-associated lipocalin contributes to erlotinib resistance in non-small cell lung cancer. American journal of translational research 2013;5(5):481-96.

17. Gazdar AF, Brambilla E. Preneoplasia of lung cancer. Cancer Biomark 2010;9(1-6):385-96.

18. Ooi AT, Gower AC, Zhang KX, Vick JL, Hong L, Nagao B, Wallace WD, Elashoff DA, Walser TC, et al. Molecular profiling of premalignant lesions in lung squamous cell carcinomas identifies mechanisms involved in stepwise carcinogenesis. Cancer prevention research 2014;7(5):487-95.

19. Ramirez RD, Sheridan S, Girard L, Sato M, Kim Y, Pollack J, Peyton M, Zou Y, Kurie JM, et al. Immortalization of human bronchial epithelial cells in the absence of viral oncoproteins. Cancer Res 2004;64(24):9027-34.

20. Hirsch FR, Franklin WA, Gazdar AF, Bunn PA, Jr. Early detection of lung cancer: clinical perspectives of recent advances in biology and radiology. Clin Cancer Res 2001;7(1):5-22.

21. Sato M, Vaughan MB, Girard L, Peyton M, Lee W, Shames DS, Ramirez RD, Sunaga N, Gazdar AF, et al. Multiple oncogenic changes (K-RAS(V12), p53 knockdown, mutant EGFRs, p16 bypass, telomerase) are not sufficient to confer a full malignant phenotype on human bronchial epithelial cells. Cancer Res 2006;66(4):2116-28.

22. Gomperts BN, Spira A, Massion PP, Walser TC, Wistuba, II, Minna JD, Dubinett SM. Evolving concepts in lung carcinogenesis. Semin Respir Crit Care Med 2011;32(1):32-43.

23. Grant JL, Fishbein MC, Hong LS, Krysan K, Minna JD, Shay JW, Walser TC, Dubinett SM. A novel molecular pathway for Snail-dependent, SPARC-mediated invasion in non-small cell lung cancer pathogenesis. Cancer prevention research 2013.

24. Carver EA, Jiang R, Lan Y, Oram KF, Gridley T. The mouse snail gene encodes a key regulator of the epithelial-mesenchymal transition. Mol Cell Biol 2001;21(23):8184-8.

25. Maina F, Pante G, Helmbacher F, Andres R, Porthin A, Davies AM, Ponzetto C, Klein R. Coupling Met to specific pathways results in distinct developmental outcomes. Molecular cell 2001;7(6):1293-306.

26. Tanimizu N, Miyajima A. Molecular mechanism of liver development and regeneration. International review of cytology 2007;259:1-48.

27. Arnoux V, Nassour M, L'Helgoualc'h A, Hipskind RA, Savagner P. Erk5 controls Slug expression and keratinocyte activation during wound healing. Molecular biology of the cell 2008;19(11):4738-49.

28. Kalluri R, Weinberg RA. The basics of epithelial-mesenchymal transition. J Clin Invest 2009;119(6):1420-8.

29. Heinrich EL, Walser TC, Krysan K, Liclican EL, Grant JL, Rodriguez NL, Dubinett SM. The inflammatory tumor microenvironment, epithelial mesenchymal transition and lung carcinogenesis. Cancer Microenviron 2012;5(1):5-18.

30. Jechlinger M, Grunert S, Beug H. Mechanisms in epithelial plasticity and metastasis: insights from 3D cultures and expression profiling. Journal of mammary gland biology and neoplasia 2002;7(4):415-32.

31. Tam WL, Weinberg RA. The epigenetics of epithelial-mesenchymal plasticity in cancer. Nat Med 2013;19(11):1438-49.

32. Hanahan D, Weinberg RA. The hallmarks of cancer. Cell 2000;100(1):57-70.

33. Hanahan D, Weinberg RA. Hallmarks of cancer: the next generation. Cell 2011;144(5):646-74.

34. Guo W, Keckesova Z, Donaher JL, Shibue T, Tischler V, Reinhardt F, Itzkovitz S, Noske A, Zurrer-Hardi U, et al. Slug and Sox9 cooperatively determine the mammary stem cell state. Cell 2012;148(5):1015-28.

35. Mani SA, Guo W, Liao MJ, Eaton EN, Ayyanan A, Zhou AY, Brooks M, Reinhard F, Zhang CC, et al. The epithelial-mesenchymal transition generates cells with properties of stem cells. Cell 2008;133(4):704-15.

36. Rhim AD, Mirek ET, Aiello NM, Maitra A, Bailey JM, McAllister F, Reichert M, Beatty GL, Rustgi AK, et al. EMT and dissemination precede pancreatic tumor formation. Cell 2012;148(1-2):349-61.

37. Rhim AD, Thege FI, Santana SM, Lannin TB, Saha TN, Tsai S, Maggs LR, Kochman ML, Ginsberg GG, et al. Detection of circulating pancreas epithelial cells in patients with pancreatic cystic lesions. Gastroenterology 2014;146(3):647-51.

38. Sanchez-Garcia I. The crossroads of oncogenesis and metastasis. N Engl J Med 2009;360(3):297-9.

39. Marchiando AM, Graham WV, Turner JR. Epithelial barriers in homeostasis and disease. Annu Rev Pathol 2010;5:119-44.

40. Manninen A. Epithelial polarity - Generating and integrating signals from the ECM with integrins. Exp Cell Res 2015.

41. Vaughan AE, Brumwell AN, Xi Y, Gotts JE, Brownfield DG, Treutlein B, Tan K, Tan V, Liu FC, et al. Lineage-negative progenitors mobilize to regenerate lung epithelium after major injury. Nature 2015;517(7536):621-5.

42. Jaffe AB, Hall A. Rho GTPases: biochemistry and biology. Annu Rev Cell Dev Biol 2005;21:247-69.

43. Mattila PK, Lappalainen P. Filopodia: molecular architecture and cellular functions. Nat Rev Mol Cell Biol 2008;9(6):446-54.

44. Schmidt A, Hall A. Guanine nucleotide exchange factors for Rho GTPases: turning on the switch. Genes Dev 2002;16(13):1587-609.

45. Ohashi K, Nagata K, Maekawa M, Ishizaki T, Narumiya S, Mizuno K. Rho-associated kinase ROCK activates LIM-kinase 1 by phosphorylation at threonine 508 within the activation loop. J Biol Chem 2000;275(5):3577-82.

46. Cau J, Hall A. Cdc42 controls the polarity of the actin and microtubule cytoskeletons through two distinct signal transduction pathways. J Cell Sci 2005;118(Pt 12):2579-87.

47. Millard TH, Sharp SJ, Machesky LM. Signalling to actin assembly via the WASP (Wiskott-Aldrich syndrome protein)-family proteins and the Arp2/3 complex. Biochem J 2004;380(Pt 1):1-17.

48. Edwards M, Zwolak A, Schafer DA, Sept D, Dominguez R, Cooper JA. Capping protein regulators fine-tune actin assembly dynamics. Nat Rev Mol Cell Biol 2014;15(10):677-89.

49. Tojkander S, Gateva G, Lappalainen P. Actin stress fibers--assembly, dynamics and biological roles. J Cell Sci 2012;125(Pt 8):1855-64.

50. Gardel ML, Schneider IC, Aratyn-Schaus Y, Waterman CM. Mechanical integration of actin and adhesion dynamics in cell migration. Annu Rev Cell Dev Biol 2010;26:315-33.

51. Olson EN, Nordheim A. Linking actin dynamics and gene transcription to drive cellular motile functions. Nat Rev Mol Cell Biol 2010;11(5):353-65.

52. Vartiainen MK, Guettler S, Larijani B, Treisman R. Nuclear actin regulates dynamic subcellular localization and activity of the SRF cofactor MAL. Science 2007;316(5832):1749-52.

53. Xin M, Small EM, Sutherland LB, Qi X, McAnally J, Plato CF, Richardson JA, Bassel-Duby R, Olson EN. MicroRNAs miR-143 and miR-145 modulate cytoskeletal dynamics and responsiveness of smooth muscle cells to injury. Genes Dev 2009;23(18):2166-78.

54. Raftopoulou M, Hall A. Cell migration: Rho GTPases lead the way. Dev Biol 2004;265(1):23-32.

55. Arber S, Barbayannis FA, Hanser H, Schneider C, Stanyon CA, Bernard O, Caroni P. Regulation of actin dynamics through phosphorylation of cofilin by LIM-kinase. Nature 1998;393(6687):805-9.

56. Mitin N, Roberts PJ, Chenette EJ, Der CJ. Posttranslational lipid modification of Rho family small GTPases. Methods Mol Biol 2012;827:87-95.

57. Michaelson D, Silletti J, Murphy G, D'Eustachio P, Rush M, Philips MR. Differential localization of Rho GTPases in live cells: regulation by hypervariable regions and RhoGDI binding. J Cell Biol 2001;152(1):111-26.

58. Mecham RP. Overview of extracellular matrix. Current protocols in cell biology / editorial board, Juan S Bonifacino [et al] 2012;Chapter 10:Unit 10 1.

59. Annoni R, Lancas T, Yukimatsu Tanigawa R, de Medeiros Matsushita M, de Morais Fernezlian S, Bruno A, Fernando Ferraz da Silva L, Roughley PJ, Battaglia S, et al. Extracellular matrix composition in COPD. The European respiratory journal 2012;40(6):1362-73.

60. Lo CM, Wang HB, Dembo M, Wang YL. Cell movement is guided by the rigidity of the substrate. Biophys J 2000;79(1):144-52.

61. Wang Z, Geng Y. Unidirectional cell crawling model guided by extracellular cues. Journal of biomechanical engineering 2015;137(3).

62. Pathak A, Kumar S. Independent regulation of tumor cell migration by matrix stiffness and confinement. Proc Natl Acad Sci U S A 2012;109(26):10334-9.

63. Chen J, Irianto J, Inamdar S, Pravincumar P, Lee DA, Bader DL, Knight MM. Cell mechanics, structure, and function are regulated by the stiffness of the three-dimensional microenvironment. Biophys J 2012;103(6):1188-97.

64. Weiss L. STUDIES ON CELL DEFORMABILITY : I. Effect of Surface Charge. J Cell Biol 1965;26(3):735-9.

65. Xu W, Mezencev R, Kim B, Wang L, McDonald J, Sulchek T. Cell stiffness is a biomarker of the metastatic potential of ovarian cancer cells. PLoS One 2012;7(10):e46609.

66. Thery M, Bornens M. Get round and stiff for mitosis. HFSP journal 2008;2(2):65-71.

67. Maddox AS, Burridge K. RhoA is required for cortical retraction and rigidity during mitotic cell rounding. J Cell Biol 2003;160(2):255-65.

68. Pajerowski JD, Dahl KN, Zhong FL, Sammak PJ, Discher DE. Physical plasticity of the nucleus in stem cell differentiation. Proc Natl Acad Sci U S A 2007;104(40):15619-24.

69. Stamenovic D, Ingber DE. Models of cytoskeletal mechanics of adherent cells. Biomech Model Mechan 2002;1(1):95-108.

70. Gardel ML, Shin JH, MacKintosh FC, Mahadevan L, Matsudaira P, Weitz DA. Elastic Behavior of cross-linked and bundled actin networks. Science 2004;304(5675):1301-05.

71. Gladilin E, Gonzalez P, Eils R. Dissecting the contribution of actin and vimentin intermediate filaments to mechanical phenotype of suspended cells using high-throughput deformability measurements and computational modeling. Journal of biomechanics 2014;47(11):2598-605.

72. Janmey PA, Euteneuer U, Traub P, Schliwa M. Viscoelastic Properties of Vimentin Compared with Other Filamentous Biopolymer Networks. Journal of Cell Biology 1991;113(1):155-60.

73. Gittes F, Mickey B, Nettleton J, Howard J. Flexural Rigidity of Microtubules and Actin-Filaments Measured from Thermal Fluctuations in Shape. Journal of Cell Biology 1993;120(4):923-34.

74. Brangwynne CP, MacKintosh FC, Kumar S, Geisse NA, Talbot J, Mahadevan L, Parker KK, Ingber DE, Weitz DA. Microtubules can bear enhanced compressive loads in living cells because of lateral reinforcement. Journal of Cell Biology 2006;173(5):733-41.

75. Wolf K, Te Lindert M, Krause M, Alexander S, Te Riet J, Willis AL, Hoffman RM, Figdor CG, Weiss SJ, et al. Physical limits of cell migration: control by ECM space and nuclear deformation and tuning by proteolysis and traction force. J Cell Biol 2013;201(7):1069-84.

76. Gerlitz G, Bustin M. Efficient cell migration requires global chromatin condensation. J Cell Sci 2010;123(Pt 13):2207-17.

77. Goldman RD, Gruenbaum Y, Moir RD, Shumaker DK, Spann TP. Nuclear lamins: building blocks of nuclear architecture. Gene Dev 2002;16(5):533-47.

78. Capco DG, Penman S. Mitotic Architecture of the Cell - the Filament Networks of the Nucleus and Cytoplasm. Journal of Cell Biology 1983;96(3):896-906.

79. Rowat AC, Jaalouk DE, Zwerger M, Ung WL, Eydelnant IA, Olins DE, Olins AL, Herrmann H, Weitz DA, et al. Nuclear Envelope Composition Determines the Ability of Neutrophil-type Cells to Passage through Micron-scale Constrictions. Journal of Biological Chemistry 2013;288(12):8610-18.

80. Harada T, Swift J, Irianto J, Shin JW, Spinler KR, Athirasala A, Diegmiller R, Dingal PCDP, Ivanovska IL, et al. Nuclear lamin stiffness is a barrier to 3D migration, but softness can limit survival. Journal of Cell Biology 2014;204(5):669-82.

81. Davidson PM, Denais C, Bakshi MC, Lammerding J. Nuclear Deformability Constitutes a Rate-Limiting Step During Cell Migration in 3-D Environments. Cell Mol Bioeng 2014;7(3):293-306.

82. Needham D, Nunn RS. Elastic deformation and failure of lipid bilayer membranes containing cholesterol. Biophys J 1990;58(4):997-1009.

83. Byfield FJ, Aranda-Espinoza H, Romanenko VG, Rothblat GH, Levitan I. Cholesterol depletion increases membrane stiffness of aortic endothelial cells. Biophys J 2004;87(5):3336-43.

84. Hissa B, Pontes B, Roma PM, Alves AP, Rocha CD, Valverde TM, Aguiar PH, Almeida FP, Guimaraes AJ, et al. Membrane cholesterol removal changes mechanical properties of cells and induces secretion of a specific pool of lysosomes. PLoS One 2013;8(12):e82988.

85. Yang YT, Liao JD, Lin CCK, Chang CT, Wang SH, Ju MS. Characterization of cholesterol-depleted or -restored cell membranes by depth-sensing nano-indentation. Soft Matter 2012;8(3):682-87.

86. Sok M, Sentjurc M, Schara M, Stare J, Rott T. Cell membrane fluidity and prognosis of lung cancer. Annals of Thoracic Surgery 2002;73(5):1567-71.

87. Taraboletti G, Perin L, Bottazzi B, Mantovani A, Giavazzi R, Salmona M. Membrane Fluidity Affects Tumor-Cell Motility, Invasion and Lung-Colonizing Potential. International Journal of Cancer 1989;44(4):707-13.

88. Zeisig R, Koklic T, Wiesner B, Fichtner I, Sentjurc M. Increase in fluidity in the membrane of MT3 breast cancer cells correlates with enhanced cell adhesion in vitro and increased lung metastasis in NOD/SCID mice. Arch Biochem Biophys 2007;459(1):98-106.

89. Edmond V, Dufour F, Poiroux G, Shoji K, Malleter M, Fouque A, Tauzin S, Rimokh R, Sergent O, et al. Downregulation of ceramide synthase-6 during epithelial-to-mesenchymal transition reduces plasma membrane fluidity and cancer cell motility. Oncogene 2015;34(8):996-1005.

90. Reed J, Mishra B, Pittenger B, Magonov S, Troke J, Teitell MA, Gimzewski JK. Single molecule transcription profiling with AFM. Nanotechnology 2007;18(4):44032.

91. Cross SE, Jin YS, Rao J, Gimzewski JK. Nanomechanical analysis of cells from cancer patients. Nature nanotechnology 2007;2(12):780-3.

92. Cross SE, Jin YS, Tondre J, Wong R, Rao J, Gimzewski JK. AFM-based analysis of human metastatic cancer cells. Nanotechnology 2008;19(38):384003.

93. Sharma S, Santiskulvong C, Bentolila LA, Rao J, Dorigo O, Gimzewski JK. Correlative nanomechanical profiling with super-resolution F-actin imaging reveals novel insights into mechanisms of cisplatin resistance in ovarian cancer cells. Nanomedicine : nanotechnology, biology, and medicine 2012;8(5):757-66.

94. Gossett DR, Tse HT, Lee SA, Ying Y, Lindgren AG, Yang OO, Rao J, Clark AT, Di Carlo D. Hydrodynamic stretching of single cells for large population mechanical phenotyping. Proc Natl Acad Sci U S A 2012;109(20):7630-5.

95. Tse HT, Gossett DR, Moon YS, Masaeli M, Sohsman M, Ying Y, Mislick K, Adams RP, Rao J, et al. Quantitative diagnosis of malignant pleural effusions by single-cell mechanophenotyping. Sci Transl Med 2013;5(212):212ra163.

96. Guck J, Schinkinger S, Lincoln B, Wottawah F, Ebert S, Romeyke M, Lenz D, Erickson HM, Ananthakrishnan R, et al. Optical deformability as an inherent cell marker for testing malignant transformation and metastatic competence. Biophys J 2005;88(5):3689-98.

97. Wirtz D, Konstantopoulos K, Searson PC. The physics of cancer: the role of physical interactions and mechanical forces in metastasis. Nat Rev Cancer 2011;11(7):512-22.

98. Remmerbach TW, Wottawah F, Dietrich J, Lincoln B, Wittekind C, Guck J. Oral cancer diagnosis by mechanical phenotyping. Cancer Res 2009;69(5):1728-32.

99. Zhang W, Kai K, Choi DS, Iwamoto T, Nguyen YH, Wong H, Landis MD, Ueno NT, Chang J, et al. Microfluidics separation reveals the stem-cell-like deformability of tumor-initiating cells. Proc Natl Acad Sci U S A 2012;109(46):18707-12.

100. Hung W-C, Chen S-H, Paul CD, Stroka KM, Lo Y-C, Wang JT, Kostantopoulos K. Distinct signaling mechanisms regulate migration in unconfined versus confined spaces. The Journal of Cell Biology 2013;202:807-24.

101. Leslie M. Crawling cells feel the squeeze. The Journal of Cell Biology 2013;202:721.

102. Welch MD. Cell migration, freshly squeezed. Cell 2015;160(4):581-2.

103. Ruprecht V, Wieser S, Callan-Jones A, Smutny M, Morita H, Sako K, Barone V, Ritsch-Marte M, Sixt M, et al. Cortical contractility triggers a stochastic switch to fast amoeboid cell motility. Cell 2015;160(4):673-85.

104. Liu YJ, Le Berre M, Lautenschlaeger F, Maiuri P, Callan-Jones A, Heuze M, Takaki T, Voituriez R, Piel M. Confinement and low adhesion induce fast amoeboid migration of slow mesenchymal cells. Cell 2015;160(4):659-72.

105. Mehlen P, Puisieux A. Metastasis: a question of life or death. Nat Rev Cancer 2006;6(6):449-58.

106. Stock AM, Troost G, Niggemann B, Zanker KS, Entschladen F. Targets for anti-metastatic drug development. Current pharmaceutical design 2013;19(28):5127-34.

107. Wang W, Goswami S, Sahai E, Wyckoff JB, Segall JE, Condeelis JS. Tumor cells caught in the act of invading: their strategy for enhanced cell motility. Trends Cell Biol 2005;15(3):138-45.

108. Auerbach O, Stout AP, Hammond EC, Garfinkel L. Changes in bronchial epithelium in relation to cigarette smoking and in relation to lung cancer. N Engl J Med 1961;265:253-67.

CHAPTER TWO: Ex-vivo micropore selection isolates a subpopulation of lung epithelial cells with altered biophysical, molecular, and metastatic properties

Abstract

Lung cancer is heterogeneous both among different tumors and in terms of the properties of cells within an individual tumor. However, little is known regarding cellular heterogeneity for biophysical properties such as cell motility and deformability and their relationship to metastatic behavior, especially in early disease pathogenesis. In this study, we isolated a subpopulation of premalignant lung epithelial cells with high migratory capacity, and found these cells to have over 100-fold enhanced migration rates through microporous constrictions which are Rac1-dependent, and to maintain this phenotype through multiple cell divisions (heritability) for greater than 8-weeks post-isolation. This lung epithelial subpopulation stably exhibited unique stiffness profiles measured by deformability cytometry and atomic force microscopy, and an increased cell spreading morphology. In a murine model of metastatic seeding, similar selected cells show greater survival in the lung, overcoming an important aspect of “metastatic inefficiency,” first described by Leonard Weiss.

Significance: Overall, our results indicate that among premalignant epithelial cells, subpopulations with heritable migration-related biophysical properties may facilitate metastatic capacity early in the pathogenesis of lung cancer. Understanding and targeting/preventing these critical molecular and biophysical mechanisms provide a new therapeutic approach to prevent metastases in early stage lung cancer.

Introduction

The most effective therapy for early stage lung cancer is surgical resection, however ~50% of these patients will still die of metastatic disease (1). Thus, micrometastatic disease must already be present at the time of surgery, but below current levels of clinical detection. This is consistent with the reports of circulating tumor cells in patients with Stage I non-small cell lung cancer (NSCLC) (2,3). Although metastatic behavior is often considered a late event, these findings suggest that the metastatic process is also operative in early stage disease, and are consistent with laboratory-based investigations indicating that dissemination may occur during early tumor development, particularly in the context of epithelial-mesenchymal transition (EMT) (4-8).

A major question is whether all cells within a tumor are capable of metastases or whether this crucial property resides in only a subset of cells and thus represents clinically important intra-tumor heterogeneity. While cells derived from a clonal population can vary widely in their gene expression profile (9), an important and overlooked level of heterogeneity is in biophysical and behavioral properties of cells such as stiffness, motility, and migration. Recently, Liu et al. and Ruprecht et al. described how confinement in a 3-dimensional space and contractility influence motility mode plasticity (where low adhesion induced “fast” amoeboid migration of “slow” mesenchymal cells) and instigate a mode termed “stable bleb migration” in embryonic and tumor cells (10-12).

Cell stiffness correlates with the metastatic potential in a variety of malignancies (13-15), and recent attempts to isolate highly deformable cells established an

association between deformability and breast cancer stem cell phenotypes (16). Few attempts have been made to isolate cells based on motile behavior *in vitro* or *in vivo* (17-19). While these studies yielded important findings, critical questions remain unanswered including whether migration properties are heritable (from one cell generation to the next), whether cells with an inherent migratory ability (in the absence of stimulatory agents) can be isolated, how factors such as cell size or ability to deform under constrictive space are related to enhanced migration, what genes are functionally important for migratory epithelial cells especially in the earliest stages of carcinogenesis, and how these properties relate to eventual metastatic potential.

Here, we describe the isolation of highly migratory cells from oncogene-modified human bronchial epithelial cells (HBECs), a robust model of the pulmonary airway epithelium and its associated malignant transformation (20,21), and demonstrate that migratory behavior is heritable across cell generations. These highly migratory cells show increased deformability, the ability to arrest successfully in the lung using a murine experimental metastasis model, and to have Rac1-dependent migration. Isolation of non-transformed epithelial cells with the highest migratory capacity has allowed for a more complete understanding of their behavioral, physical, and genetic attributes, which will ultimately lead to a better understanding of how to combat the molecular drivers of epithelial cell migration therapeutically in order to intervene in a preventative manner at the earliest stages of lung cancer dissemination.

Results

SNAIL enhances motility and migration of human bronchial epithelial cells

We and others have shown that expression of SNAIL, a transcription factor known to drive the epithelial-mesenchymal transition (EMT) program (22), in various cancer cell lines leads to increased migration and invasion both *in vitro* and *in vivo* (23,24). In order to model EMT in pulmonary premalignancy, we created HBEC lines that ectopically express *SNAIL* with or without various mutations found in lung premalignancy and cancer (*P53*-loss and *KRAS*-activating mutations, **Table 2.1**) (21,25). Phase contrast imaging shows that SNAIL-expressing HBECs (HBEC-Snail) have a morphological phenotype indicative of motile and migratory capacities, including membrane ruffling and lamellipodia formation (**Figure 2.1**).

To determine if a behavioral function coincides with this morphological phenotype, HBEC-Snail and vector control cells were subjected to a motility assay. On average, HBEC-Snail cells move with up to 50% higher velocity compared to vector control cells and an order of magnitude difference exists between the fastest and slowest moving cells (**Figures 2.2 and 2.3**). In addition, we performed a migration assay utilizing transwell membranes of various pore size in the absence of a chemoattractant (basal growth media on both sides in order to eliminate chemotactic responses). At the 5- and 3 μm pore sizes, H3mut-Snail cells showed more than a 10- and 20-fold increase in migration rate, respectively, compared to vector control cells (**Figure 2.4**). Importantly, although migration through 3 μm transwells was 20-fold greater with *SNAIL* expression, the absolute number of migratory cells was very low,

accounting for less than 0.1% of the total number of cells plated. These cells represent the most migratory cells in the population.

Cells with inherently higher rates of migration can be enriched from a heterogeneous population and exhibit heritability of this phenotype

To isolate such highly migratory cells, we devised a selection strategy using a series of microporous membranes (**Figure 2.5**). Cells were initially seeded on 8 μm-pore transwell membranes with basal growth medium in top and bottom chambers and incubated for 48 hours. Because the number of cells in the top chamber exceeds that of the bottom chamber, the nutrients in the top chamber will be exhausted faster and cells might be artificially driven to the bottom chamber where nutrients are in higher concentration. To avoid inadvertent generation of a chemotactic gradient due to nutrient depletion (26), media in both chambers was replaced after 24 hours. After 48 hours, the cells in the bottom chamber were isolated by trypsinization and propagated in a new dish. They were re-plated onto a new membrane, and the process repeated. The pore size was serially decreased, first to 5-μm and then 3-μm pores. It is noteworthy that an insufficient quantity of cells migrated through 5- or 3 μm pores within 48 hours to justify immediate selection at these sizes, thus negating the possibility of skipping *a priori* selection through 8 μm pores (**Figure 2.4**). Cells obtained following selection are denoted HM (highly migratory).

Cells were then subjected to a migration assay using 8, 5 and 3 μm pore membranes, and differentially stained to simultaneously observe migration rate and viability. H3mut-Snail-HM and H3mut-Vector-HM both had 5-fold higher migration rates

through 8 μm pores, 20- and 30-fold higher migration rates through 5 μm pores, and 59- and 124-fold higher migration rates through 3 μm pores, compared to their unselected counter parts (**Figure 2.6**)**.** Similar results were seen in the H3 and H4 cell line pairs as well as A549-Snail/Vector pairs (**Figure 2.7**). By dual staining for live/dead cell analysis, we found that without prior selection, migration through 3 μm pores results in a high incidence of cell death, accounting for approximately 50% viability in the unselected lines (**Figures 2.8 and 2.9**). While unique mechanisms are required for migration versus invasion, we wanted to determine if highly migratory cells were also highly invasive. H3mut-Snail and H3mut-Vector cells showed no difference in invasion through collagen following selection. However, invasion rates at baseline in the H3mut cell lines were already high. H4-Snail-HM and H4-Vector-HM cells showed enhanced invasion in a collagen matrix compared to parental cells (**Figure 2.10**).

In order to determine if the migratory phenotype would be sustained through many generations, the transwell migration assay was carried out after 40 population doublings (up to 8 weeks) following selection. Over this time the selected cells remain highly migratory when compared to their unselected counterparts (**Figures 2.11 and 2.12**), indicating that the selected migration phenotype is heritable and thus, can be exploited to expand such cells for downstream functional analysis.

Selection isolates cells capable of overcoming a critical juncture in metastatic inefficiency

Leonard Weiss first described the concept of “metastatic inefficiency”, which has been observed by others (27,28). Chambers *et al* have extended these studies by

describing points in the metastatic cascade that typically result in cell death, which include intravasation and extravasation (29). These findings and the results from our post-migration viability studies prompted us to test our selected cells in an *in vivo* model that would examine the transition from the intravascular space to the lung parenchyma. $5x10^5$ H3mut-Snail or H3mut-Snail-HM cells were injected into the tail vein of SCID mice. After 72 hours, total DNA was extracted from lung homogenates. A PCR-based method described by Malek *et al* was used to quantify the number of human cells that arrested in the mouse lung (30). Mice injected with the micropore-selected H3mut-Snail-HM cells showed greater than 2.5-fold more human DNA in the mouse lungs on average compared to mice injected with H3mut-Snail cells (**Figure 2.13**). Taken together with the *in vitro* viability studies, this suggests that the selected cells have overcome this stage of metastatic inefficiency.

Biophysical characterization of highly migratory cells shows no selection bias and cell spreading mediated by SNAIL

Because we and others have shown that SNAIL leads to enhanced motility and migration, we sought to determine if highly migratory cells had greater SNAIL expression than their unselected counterparts but found no differences in protein levels (**Figure 2.14**). Another reason for enhanced migration potential of these cells is ability to spread. Cells with the capacity to alter morphology to the “spread” phenotype might reflect greater control over their shape and thus more readily pass through constrictive space. Images of highly migratory cells were taken using phase contrast microscopy. Using ImageJ (31), outlines were made of each cell (**Figure 2.15**) and the

corresponding areas were calculated. H3mut-Vector-HM cells were approximately the same size as unselected cells (**Figure 2.16 and Table 2.2**). H3mut-Snail-HM cells were approximately 30% larger in area than their unselected counterparts, indicating a more "spread" phenotype. Although H4-Snail cells had a decrease in cell area, the corresponding Feret's diameter, (defined as the longest stretch between two edges of the cell), was increased by approximately 35%. Additionally, because dual staining shows that nuclear damage is possible as a result of migration through small pores (**Figure 2.8**), we measured the size of the nucleus by staining nuclear membrane proteins Lamin B1, which highlight the nuclear boundary, to determine if nuclear size was a rate-limiting factor for successful migration. H4-Snail-HM cells have decreased nuclear area and H4-Vector-HM cells have an increase in nuclear area, while H3mut cells show no significant difference in nuclear size (**Figure 2.17**). Together, these data indicate that our selection strategy does not select for smaller cells or nuclei. Increases in cell spreading suggest that HM cells may have greater control over morphology which would aid migration through constrictive space.

Determining the association of cell size and deformability in migration

When attached to tissue culture plastic, H3mut cells can span greater than 150 μm in length, and the nuclei alone can be as large as 30 μm in diameter. We hypothesized that there could be a deformability component to cell migration required in order to traverse increasingly smaller pore sizes that are a fraction of the cell volume. To assess cellular deformability, we utilized deformability cytometry (DC). This technique uses hydrodynamic forces to stretch cells uniformly in a microfluidic chip

followed by high-speed imaging to discern changes in cell shape and size as a result of applied stress (32). Deformability (D) is a unitless measure defined as the maximum ratio of the long to short axis of a cell stretched with a standard stress, such that a cell with a lower stiffness will have a corresponding higher deformability. As expected, although there is heterogeneity from cell to cell, H3mut-Snail-HM cells were on average slightly more deformable than unselected counterparts (D = 1.529±0.009 vs. 1.489±0.003, respectively, with n>1000 cells for each measurement **Figure 2.18 and Table 2.2**). However, H3mut-Vector-HM cells were less deformable than H3mut-Vector cells (1.274±0.003 vs. 1.329±0.011, respectively). The inverse phenotype is observed with H4 cells, such that H4-Snail-HM is less deformable and H4-Vector-HM is more deformable than unselected counterparts. A secondary readout of DC is size when the cells are in suspension just prior to entering the deformation region in the chip. Along with being more deformable, H3mut-Snail-HM cells had approximately 5% larger diameter (15% larger volume) than unselected cells, in agreement with the larger spread area of these cells. Consistent with this, H3mut-Vector-HM cells were less deformable and 12% smaller than unselected cells (**Figure 2.18 and Table 2.2**). Again, we see the inverse relationship with respect to H4-HM cells (H4-Snail-HM is smaller and H4-Vector-HM is larger). This indicates that the selection strategy does not bias towards biophysical properties, such as size or deformability, but rather selects based on migratory behavior more specifically. These results also suggest, at least in the described system, that high deformability is not the only mechanism by which cells can traverse confined space.

Determining the role of cell stiffness in migration

DC measures deformability while cells are in suspension and may be a good measurement of cytoskeletal components or changes in nuclear stiffness (32). Conversely, atomic force microscopy (AFM) measures cells while adherent, therefore, it is an indicator of the stiffness of a motile cell. 24 hours after plating, cells were probed using an AFM coupled to an optical microscope, which allows for force measurements to be made directly over the nucleus, which were then converted to stiffness. The Young's modulus of the H3mut-Snail cells is 1607± 40.87 Pascals (Pa), whereas the H3mut-Snail-HM cells have a Young's Modulus of 1250±48.29 Pa, representing a 23% reduction in stiffness. Consistent with DC, AFM confirms that H3mut-Snail-HM cells are less stiff than unselected H3mut-Snail cells (**Figure 2.19**). Measurements on H3mut-Vector-HM cells show no difference when compared to the unselected counterparts.

Fluorescence microscopy reveals SNAIL-mediated changes to the actin cytoskeleton and myosin localization in lung epithelial cells with the highest migratory potential

H3mut-Snail-HM cells were more deformable by both DC and AFM, whereas the H3mut-Vector-HM cells were less deformable by DC and showed no change by AFM. The AFM predominately measures stiffness of the actin cytoskeleton, as the probe only penetrates ~500 nm into the cell. We hypothesized there may be SNAIL-dependent changes to actin in the highly migratory cells. To test this, we grew selected and unselected cells on cover slips and stained them using fluorescent phalloidin. H3mut-Snail-HM cells showed more F-actin bundles in the lamellipodia than unselected counterparts (**Figure 2.20**). While H4-Snail-HM cells did not show similar F-actin structures, they show a striking change in morphology (**Figure 2.20**); conversely,

H3mut-Vector-HM and H4-Vector-HM cells showed no apparent difference in F-actin structures (**Figure 2.21**). Because of the well-described relationship between F-actin and myosin, we stained cells for phosphorylated (activated) myosin light chain II (pMLC2). H3mut-Snail-HM cells showed pMLC2 that localized to the periphery, whereas the other lines tested (H3mut-Snail and vector controls) showed perinuclear localization (**Figure 2.22**). In measuring the pixel intensity, spikes in pMLC2 staining overlap with spikes in F-actin staining in the H3mut-Snail HM cells (**Figure 2.23**). These results suggest that there are SNAIL-mediated changes to the cytoskeleton in the cells with the highest migratory potential.

Rac1 activity contributes to the high migratory phenotype and can be pharmacologically inhibited

Rho-family GTPases are major regulators of the actin cytoskeleton, and their signaling facilitates processes such as cell polarity and motility (33). We next determined the activation status of three well-characterized GTPases, RhoA, Rac1 and Cdc42, to determine if they are altered in the high migration rate phenotype. Whole-cell lysates were utilized in a pull-down assay with agarose beads conjugated to Rhotekin or p21-activated kinase binding domain (PAK), which recognizes GTP-bound (activated) RhoA or Rac1 and Cdc42, respectively. We observed no detectible change in RhoA or Cdc42 activity, but a 2-fold increase in activated Rac1 (**Figure 2.24**). To verify enhanced Rac1 activity drives migration in HM cells, we pharmacologically inhibited Rac1 in these cells in a migration assay (using concentration of inhibitor that did not prevent cell growth) (**Figure 2.25**). Inhibition of Rac1 activation by NSC-23766, an

inhibitor of a Rac1-specific guanine nucleotide exchange factor (GEF), perturbed cell migration compared to treatment controls (**Figure 2.26**). These results suggest that Rac1 pathway activation is at least partially responsible for the highly migratory phenotype and that the phenotype can be targeted pharmacologically by attacking Rac1.

Gene expression analysis reveals subtle changes attributable to the highly migratory phenotype

To determine if there was any correlation in gene expression between the highly migratory phenotype and publically-available clinically-relevant databases, we isolated total RNA from selected and unselected cells and performed microarray mRNA profiling. Gene expression analysis identified 278 genes whose expression associated with either *SNAI1* expression or migration or both based on pair-wise comparison between two conditions. The majority of identified genes were deregulated by over-expressing *SNAI1* (**Figure 2.27**, left panel), and very few associated with high mobility as a result of selection (**Figure 2.27**, right panel). Interestingly, deregulated mobility-dependent genes (cluster 1 and cluster 5 in **Figure 2.27**, right panel) were actually a subgroup of *SNAI1*- (or EMT-) associated genes. To be able to move faster than parental cells, highly migratory cells reverse the expression of a small group of EMT-associated genes, while the expression of the majority of EMT-associated genes remained unchanged. For instance, expression epithelial marker *CDH1* was unaffected in high mobility cells, but that of mesenchymal marker *CDH2* in highly migratory cells was decreased as compared to parental *SNAI1* cells, even though expression was still higher than the

basal level in vector cells. Gene set enrichment analysis (GSEA) revealed genes correlated with the highly migratory phenotype were as enriched in gene sets associated with poor overall survival in NSCLC, and recurrent disease in clinical breast cancer and melanoma samples (**Figure 2.28**) (34-36).

Discussion

We have identified a small subpopulation of cells with a highly motile and metastatic phenotype, demonstrated using *in vitro* and *in vivo* methods, and found this phenotype is heritable over 40 population doublings. We have also identified a previously unknown bimodal nature of deformability with respect to enhanced migration – cells can have high or low deformability and still be highly migratory. The highly migratory phenotype is related to cell spreading and mediated by Rac1. This system thus provides an important new preclinical model to understand mechanisms and develop therapeutics targeting premalignant lung epithelial cells migration and metastasis.

By isolating highly migratory cells from both *SNAIL*-overexpressing and control populations we are able to study *SNAIL*-dependent and *SNAIL*-independent mechanisms of migration. This allowed us to model the *SNAIL*-mediated EMT program, which is known to drive migratory behavior, and is clinically relevant because SNAIL is present in lung premalignant lesions (37). We found that *SNAIL* expression in H3mut cells increases cellular deformability by both Deformability Cytometry and AFM, and that cells with the highest migratory capacity exhibited the greatest deformability. Our results are in alignment with other studies showing cells expressing the EMT program are

highly metastatic, and that migration and metastasis correlate with increased cellular deformability (5,13,38). However, increased stiffness in H4 Snail-HM cells suggest that inter-individual variations may exist in which cellular deformability is not always requisite for the highly motile phenotype. Heterogeneity amongst individuals adds an element of complexity to be defined in further investigations. For example, Liu *et al* have recently described different migration modes existing amongst cells within a single population, which they ascribe to subtle molecular differences (10). The biophysical property related to cell spreading appears to be another determinant of migratory potential. In fact, the H4-Snail-HM cells had a larger Feret's diameter and the H3mut-Snail-HM cells had a larger cell area, both of which are indicators of morphological changes in spreading that might benefit migration through confined space. It is known that the majority of cancer cells that attempt to pass through the endothelial barrier succumb to shearing (39), and we have found that the majority of HBEC cells attempting to pass through 3 μm pore sizes will die without prior selection. We found that Rac1 activity mediates enhanced migration, that pharmacologic inhibition of Rac1 activation, reduced migration in the selected highly migratory cells. Rac1 activity has been associated with carcinogenesis, EMT, and metastasis, and is a candidate therapeutic target (40,41). Genes whose expression was up-regulated in our highly migratory cells also was correlated with poor overall survival in NSCLC and increased recurrence in breast cancer and melanoma. Although not stated outright, it could be that recurrence is related to micrometastatic disease present at the time of resection, but not detected.

Metastasis is the predominate cause of cancer death in patients (42), and while a tumor is made up of many cancer cells, only a small percentage of these cells become

metastatic (19,43,44). The current studies provide a new approach using a defined and easily manipulated preclinical human model system that has employed a micropore selection system, followed by detailed interrogation of biophysical properties to identify a small subpopulation of cells with innate migratory capacity and altered properties that facilitate metastases. As part of this, mechanisms and therapeutic targets can be systematically studied.

Materials and Methods

General Cell Culture

Each parental HBEC line was derived from the large airway of an individual patient and immortalized in the absence of viral oncogenes, as previously described (20). Cell culture maintenance and creation of HBEC-Snail and vector control lines are described elsewhere (24). The cells were genotyped (STR profiling) before and after selection at the UCLA Genotyping and Sequencing Core and tested to be free of mycoplasma contamination.

Western Blot

Cells grown to 80% confluence in T25 flasks were washed with ice-cold PBS and lysed with RIPA buffer using standard methods. Twenty μg of each cell lysate was loaded per lane, and proteins were resolved by SDS-PAGE and transferred to an Immobilon-P Transfer Membrane (Millipore, Billerica, MA). The membranes were blocked with 5% milk and then incubated with primary antibodies diluted in blocking solution according to the manufacturer's recommendations. Horseradish peroxidase-conjugated secondary

antibodies (Bio-Rad, Hercules, CA) and enhanced chemiluminescence (ECL) reagent (Amersham Biosciences, Piscataway, NJ) were used for protein detection. Primary antibodies were from the following sources: TUBULIN and SNAIL (Cell Signaling Technologies, Danvers, MA); RHOA, RAC1 and CDC42 (Cytoskeleton Inc, Denver, CO). Densitometry performed in ImageJ using the “Analyze Gels” function.

Motility Assay

Cells were plated in 12-well plates at 25 cells/mm^2. After overnight attachment, cells were stained with 1 μg/mL Hoechst-33342, washed and incubated 8 hours prior to imaging in SFM. Three random fields in duplicate wells were imaged on a Nikon Eclipse Ti inverted microscope fitted with a temperature and CO_2 controlled stage at 100x total magnification for 12 hours (Nikon 10x PlanFluor, 0.30 NA). Images were taken with a Cascade II EM-CCD (Photometrics, Tucson, AZ) at a 30 ms exposure with maximum gain, controlled by Nikon Elements AR software. UV exposure was minimized using neutral density filters. The image sequence was imported into ImageJ, thresholded, and binary objects were then tracked using Mtrack plugin (45). Data shown represent the average cell speed across the entire experiment. Experiments were repeated at least three times.

Transwell migration assay

Cells were seeded into the top chamber of 12-well format Millicell inserts at 75,000 cells/well in 0.5 mL complete medium (Millipore, Billerica, MA) and incubated at 37°C. Media in both chambers was replaced after 24 hours. After 48 hours, the transwells were swabbed, fixed in 4% Paraformaldehyde (PFA) and stained with Hoechst. Plating

density was determined in un-swabbed transwells by staining with Hoechst, washing in PBS 3x5 minutes, then the entire well was imaged at 40x total magnification on a Nikon Eclipse Ti inverted microscope (Nikon 4x PlanFluor PhL DL 0.13 NA). Images were captured on a 1024x1024 pixel Cascade II EM-CCD camera with equal exposure times using Nikon Elements AR software. The cell density was determined by fluorescence intensity using the “histogram” function in ImageJ. Cell counts described below were normalized to fluorescence intensity of the respective well. To determine the number of cells that entered the bottom chamber, cells were stained with NucRed Live647 (stains all cells) and 1 µg/mL DAPI simultaneously for 20 minutes in complete medium at 37°C (Life Technologies). After staining cells were washed then fixed with 4% PFA. Within two hours of staining, at least 25 fields in each well were captured using a 10x objective (Nikon PlanFluor Ph1 DLL 0.30 NA). Cells were enumerated using the “threshold” and “analyze particles” functions in ImageJ. Viability is reported as total cells minus dead cells, divided by total cells. Experiments were repeated at least three times.

3D cell invasion assay

Experiments were performed according to previously published protocols (46). Assays were performed in 96-well plates (Black wells, clear bottom, PerkinElmer). Briefly, ice-cold serum-free liquid bovine collagen (PureCol) was prepared at 1 mg/ml concentration. After trypsinization, cells were added to the collagen suspension at a final concentration of $5x10^4$cells/ml. 100 µL aliquots were dispensed into the wells and cells were subsequently spun down, then incubated in a 37°C/5% CO2 tissue-culture incubator to allow the collagen to solidify. Finally, the collagen plug was covered by 30

µL of a mixture of appropriate culture medium diluted 1:1 with PBS. After 48 hours, cells were fixed with 4% PFA (final concentration) and stained with 10 µg/ml Hoechst-33342 (Life Technologies). Images of nuclei staining were obtained on an inverted microscope operated by Nikon Elements Software, using a 20x air objective. 25 adjacent images covering ~85% well area were taken from 0 µm (bottom of the plate) to 150 µm up in the collagen plug, with a 25 µm step. Quantification of nuclei/well was obtained using the object count feature of Nikon Elements Software. Invasion ratio was calculated as the sum of cell counts at 50, 75, 100, 125 and 150 µm over cell counts at 0 µm. Each of the 3 independent experiments consisted of 5 replicates for each condition. Bar charts are plotted as mean of the 3 experiments ± SEM.

Selection of highly migratory cells

300,000 cells/well were seeded in 6-well format Millicell inserts in 2 mL medium. After 24 hours, media in both chambers were replaced. After 48 hours, the transwell bottoms alone were harvested (trypsinization at 37°C followed by centrifugation and resuspension in medium) and cells added to the bottom chamber of the original plate; the cells were then grown to confluence. Cells were expanded to a T75 flask, and propagated until 70% confluent, after which they were plated for a subsequent round of selection. Cells were selected for three rounds through 8 µm pores, then three rounds through 5 µm pores, and finally five rounds through 3 µm pores.

Deformability Cytometry (DC)

The deformability cytometry (DC) microfluidic devices were fabricated following standardized polydimethylsiloxane (PDMS) replica molding techniques (47).

Documented channel design schematics were also followed for the DC chip master molds (32). Dissociated cell samples were diluted with media to achieve a concentration between 100,000-200,000 cells/mL. The samples were introduced to the DC chip at 800 μL/min using a Harvard Apparatus syringe pump. A Vision Research Phantom v711 high-speed camera recorded videos with the following parameters: 208x32 pixel resolution, 500,000 frames per second sample rate, 290 ns exposure time, and 290 ns EDR. A custom MATLAB script was used for the image analysis of recordings. Metrics extracted from the videos included cell size, maximum aspect ratio (deformability), and time spent in the extensional flow region. Additional details on experimental design and post processing analysis are available in previous reports (32). Experiments were repeated three times. At least 1000 cells were analyzed per sample.

Atomic Force Microscopy (AFM)

Cells were plated in 60 mm dishes in complete medium and incubated overnight for complete attachment. One hour prior to analysis, the medium was replaced with complete medium containing 25 mM HEPES (for pH control when performing AFM) and equilibrated in a 5% CO_2 controlled incubator. All measurements were conducted using a Catalyst AFM (Bruker Instruments, Santa Barbara, California) with a combined inverted optical/confocal microscope (Zeiss, Corp, Thornwood, New York). This combination permits lateral positioning of the AFM tip over the cell center with submicron precision. The AFM tip was always precisely positioned (within micron range) on top of the nucleus using motorized stage and inverted optical view of the combined confocal-AFM microscope. Mechanical measurements were collected in contact mode

using silicon nitride cantilevers with experimentally determined spring constants of 0.02 N/m and a tip radius of 20 nm. Mechanical measurements were obtained at 37°C with force measurements recorded at a pulling rate of 1 Hz. Force-displacement curves were recorded for determination of Young's modulus. Conversion of force-displacement curves to force-indentation curves allows the determination of cell surface elasticity or “stiffness” (Young's modulus, E) as described elsewhere (48). The primary measurement outcome was averaged E value. AFM measurements were obtained from at least 60 cells in three different experiments.

Cell area and Feret’s diameter Determination

Cells were plated in 6-well plates and grown for 48 hours. Three random fields were imaged at 200x total magnification (Nikon 20x S PlanFluor, ELWD 0.45 NA). Images were imported into ImageJ, where the cell perimeter was outlined using the pencil tool. The images were converted to binary using the “threshold” function, followed by “fill holes.” Cell area and Feret’s diameter was determined using the “analyze particles” function. At least 45 cells were analyzed per group.

Fluorescence Microscopy

Cells were grown on 12 mm glass cloverslips (Electron Microscopy Sciences, Hatfield, PA) in complete medium. Cells were fixed and permeabilized using 4% PFA and 0.1% Triton X-100 using standard methods. Cells were blocked for 30 minutes in 1% BSA. For nuclear size determination, cells were labeled in blocking buffer with 1:1000 mouse anti-Lamin B1 (AbCAM, Cambridge, MA) for 30 minutes at room temperature, followed by 3x5 minute 0.5% Tween-20/PBS washes. Cells were stained for 30 minutes at room

temperature in secondary antibody (goat anti-mouse Alexafluor488, Life Technologies), then washed in 0.5% Tween-20/PBS. For cytoskeleton fluorescence, cells were incubated overnight at 4°C with anti-phospho-myosin light chain (Cell Signaling, Danvers MA) at 1:100 in blocking buffer. Cells were washed and incubated with secondary antibody as described before. Cells were stained with phalloidin-AlexaFluor647 (Life Technologies) and counterstained with DAPI according to the manufacturer's instructions. ProLong Gold (Life Technologies) was used to mount the coverslips. Cells were imaged at room temperature using a Nikon Eclipse 90i upright fluorescent microscope and 10x or 20x objective (Nikon 10x PlanFluor DIC L/N1, 0.30 NA; Nikon 20x Plan Apo VC DIC N2, 0.75 NA). Images were captured using a Nikon Digital Sight DS-Qi1Mc camera at 1024x1024 or 1280x1024 pixel resolution. To quantify nuclear size, the images were thresholded using ImageJ. The "analyze particles" function was used to determine the nuclear area. At least 60 cells of each type were analyzed for nuclear size. Pixel intensity mapping was performed in ImageJ using the RGB Profiler plugin.

Metastatic inefficiency model in NSG mice and qPCR analysis

Pathogen-free NOD-SCID gamma (NSG) mice were purchased from Jackson Labs and maintained in the UCLA vivarium. All studies were approved by the institution's animal review board. Cells were harvested and washed twice with sterile saline for injection, and finally suspended at a concentration of $5x10^5$ cells in 50 µL. Mice were restrained and injected with 50 µL of the cell suspension via tail vein. After 72 hours, mice were asphyxiated using a CO_2 chamber. The whole left lung lobe was harvested and

genomic DNA was isolated using DNeasy Blood & Tissue Kit (Qiagen, Limburg, Netherlands) with slight modification: The tissue was incubated in 360 µl ATL buffer with 40 µl proteinase K (20 mg/ml) for full digestion at 56°C. Next, 400 µl of AL buffer was added and homogenized thoroughly by using Kontes Pellet pestle motor (Fisher scientific) followed by 10 minute incubation at 56°C. Then 400 µl of absolute ethanol was added and mixed completely. The mixture was transferred into the DNesay spin column and washed with 700 µl of AW1 and AW2 separately. The column was eluted with 200 µl AE buffer. qPCR analysis was performed as previously described (30), with the exception that 100 ng DNA was used.

Activated GTPase pull down

Cells were plated 10 cm dishes and grown until ~80% confluent and in growth phase. Cell lysates were harvested according to the manufacturer's protocol and using kit components (Activation Assay Combo Kit Cytoskeleton Inc, Denver, CO). 700 µg of lysate was used for each sample in the pull-down assay, as determined by BCA assay. Activated GTPase was eluted from the beads using 15 µL of 2x loading dye and proteins were resolved by SDS-PAGE and transferred to PVDF membranes. Membranes blocked in 0.1% milk and blotted for RhoA, Rac1 or Cdc42 using antibodies supplied in the kit (1:500 dilution). Densitometry performed in ImageJ. Values normalized to TUBULIN in "total lysate" fraction.

Proliferation and migration assays using inhibitors

Proliferation assay: 1000 cells were seeded in 4 replicate 96-well plates and incubated overnight. Plates were decanted and various concentrations of NSC-23766 (Cayman

Chemical, Ann Arbor, MI) were added. ATPlite assay (PerkinElmer, Waltham, MA) was used to measure ATP levels, which correlates with cell number, at 24 hour intervals. Migration assay: 10,000 cells per well were seeded in 96-well transwells (Corning Inc, Corning, NY). After overnight attachment, media in the top and bottom compartments was decanted and replaced with medium containing inhibitor. After additional 24 hour incubation, the tops of the transwells were swabbed, and cells were fixed, stained and imaged as described earlier. Values were normalized to plating density.

RNA isolation and gene expression analysis

HBECs were cultured in 10 cm dishes for 3 days. Lysates were harvested using 700 µL Qiazole (Qiagen) and RNA extracted according to manufacturer's protocol. RNA was purified using miRNeasy kit (Qiagen). Gene expression was investigated by Affymetrix GeneChip HTA 2.0 Array at the UCLA Clinical Microarray Core. Normalization at gene-based level was done by Affymetrix Expression Console using RMA approach. Non-annotated transcripts were then filtered out from the data before further analysis. Bioconductor *limma* package was used for gene expression analysis. A gene was defined as being differentially expressed by two conditions, (1) its fold change was greater than 1.5 and (2) two-tail t-test p-value was less than 0.1. Cluster 3.0 was used for clustering analysis. Gene set enrichment analysis (GSEA) was used for identifying deregulated pathways and biological processes associated with deregulated genes.

Statistical Analysis

Samples were plated and run in triplicate, unless otherwise indicated, and all experiments were performed at least three times. Statistical analyses were performed

on all data sets, and results from one representative experiment or image are shown. All statistical analyses were performed in Prism 6 (GraphPad, La Jolla, CA) unless noted. All results are reported as mean ± SEM, unless indicated. The statistical significance of these data was determined using an unpaired, parametric *t*-test with 95% confidence interval. The statistical significance of the viability data set was determined using the Mann-Whitney test (two-tailed, 95% confidence interval). Data were reported significant as follows: * if $p \leq 0.05$, ** if $p \leq 0.01$, and *** if $p \leq 0.001$.

Acknowledgments

The authors wish to acknowledge Ying Lin for technical assistance, the UCLA Genotyping/Sequencing Core for genotyping and microarray services, Jessica Byrne of the Clinical and Translational Science Institute (CTSI) for help with figure preparation. We would like to thank the CTSI, as well as the UCLA California Nanosystems Institute Advanced Light Microscopy/Spectroscopy Cores for microscopy resources.

Figures and Tables

Table 2.1: List of isogenic HBEC lines with corresponding genetic information and migration rates. For immortalization, all HBEC lines over-express *TERT* and *CDK4*.

Cell Line Name	Genetic Status	Migration Rate (average cells/field)
H3-Snail	Snail over-expression	8μm pore - 664.9 ± 47.89 5μm pore - 706.5 ± 38.69 3μm pore - 67.92 ± 5.000
H3-Snail-HM	Snail over-expression	8μm pore - 1821 ± 70.61 5μm pore - 1449 ± 95.66 3μm pore - 194.4 ± 18.22
H3-Vector	Empty vector for Snail	8μm pore - 516.3 ± 22.08 5μm pore - 227.7 ± 12.57 3μm pore - 15.72 ± 1.009
H3-Vector-HM	Empty vector for Snail	8μm pore - 1090 ± 16.17 5μm pore - 921.2 ± 15.96 3μm pore - 285.9 ± 16.73
H3mut-Snail	p53-shRNA $KRAS^{V12}$ over-expression Snail over-expression	8μm pore - 142.4 ± 12.38 5μm pore - 27.31 ± 3.395 3μm pore - 0.2449 ± 0.9002
H3mut-Snail-HM	p53-shRNA $KRAS^{V12}$ over-expression Snail over-expression	8μm pore - 811.2 ± 8.514 5μm pore - 572.2 ± 11.90 3μm pore - 14.59 ± 0.9006
H3mut-Vector	p53-shRNA $KRAS^{V12}$ over-expression Empty vector for Snail	8μm pore - 127.7 ± 5.483 5μm pore - 9.776 ± 1.383 3μm pore - 0.0204 ± 0.0204
H3mut-Vector-HM	p53-shRNA $KRAS^{V12}$ over-expression Empty vector for Snail	8μm pore - 780.3 ± 15.06 5μm pore - 290.7 ± 22.31 3μm pore - 2.531 ± 0.4257
H4-Snail	Snail over-expression	8μm pore - 107.6 ± 5.784 5μm pore - 12.36 ± 1.273 3μm pore - 1.800 ± 0.4320
H4-Snail-HM	Snail over-expression	8μm pore - 476.3 ± 10.15 5μm pore - 361.9 ± 6.460 3μm pore - 52.56 ± 2.629
H4-Vector	Empty vector for Snail	8μm pore - 938.3 ± 16.04 5μm pore - 114.7 ± 14.74 3μm pore - 13.12 ± 1.174
H4-Vector-HM	Empty vector for Snail	8μm pore - 1666 ± 18.21 5μm pore - 497.7 ± 19.81 3μm pore - 98.04 ± 9.335

Figure 2.1: Snail expression in HBECs increases the abundance of membrane structures commonly associated with a migratory phenotype. Phase contrast images of H4-Snail and H3mut-Snail show lamellipodia and membrane ruffling, which are highlighted by arrows and arrowheads, respectively. These structures are largely absent in the vector control cells. 200x total magnification; scale bars are 100 μm.

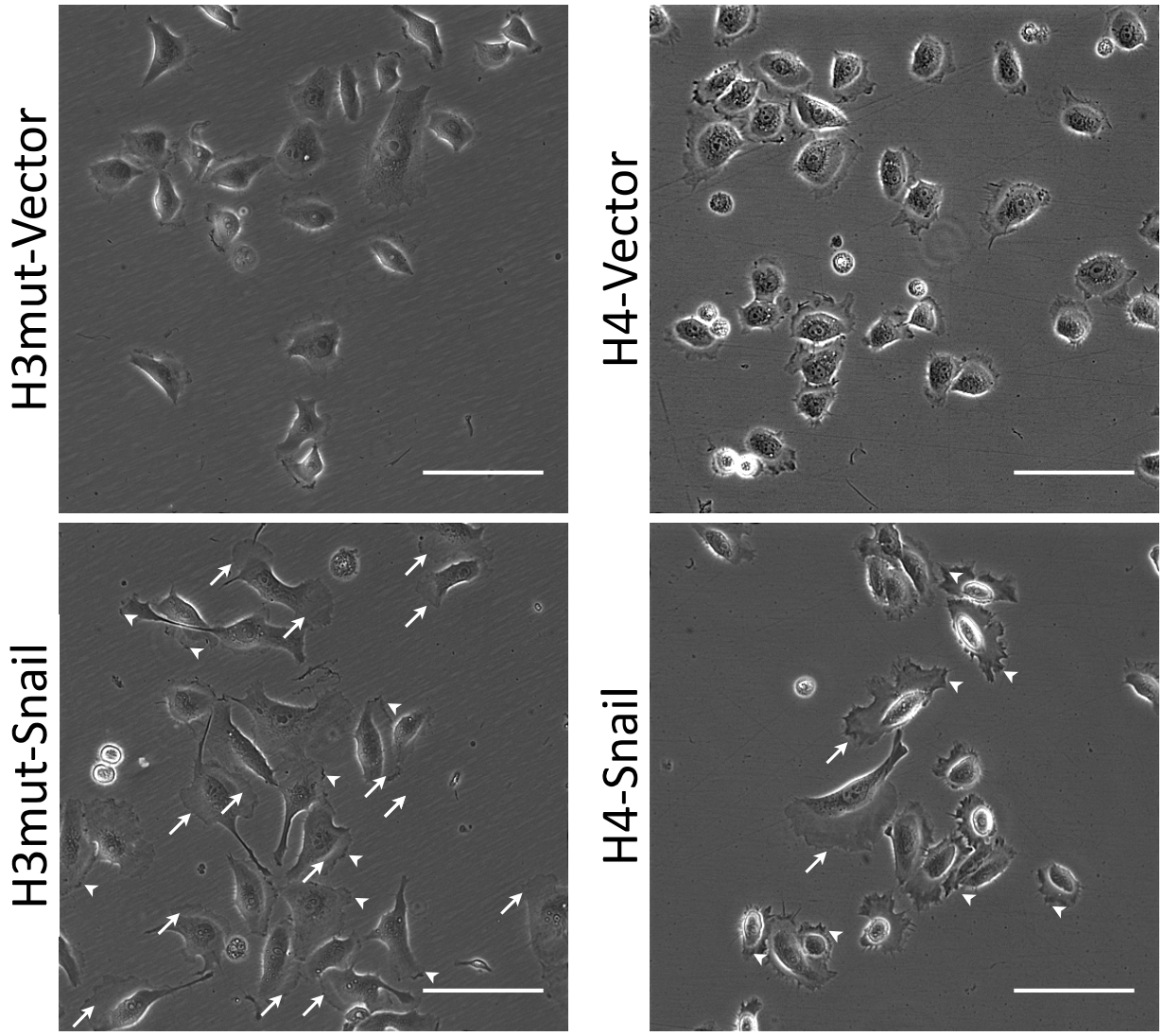

Figure 2.2: HBEC-Snail cells have increased average velocity compared to Vector cells as determined by the motility assay. Cells were plated at 25 cells/mm^2 and imaged every 5 minutes for 12 hours. 50-150 cells were analyzed per group. Data representative of three independent experiments.

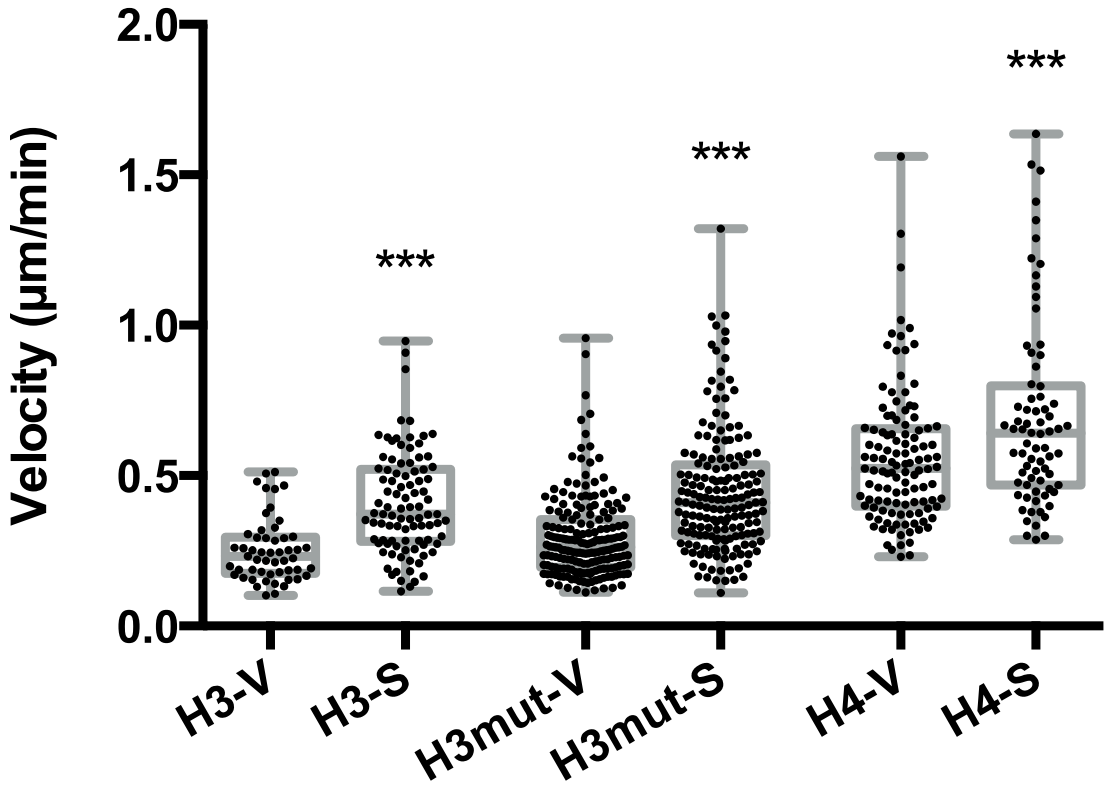

Figure 2.3: Velocity distribution profile shows great heterogeneity in motility. A 10-fold difference is observed between the fastest and slowest H3mut-Snail cell, denoted by the dotted lines. Cells were tracked for 12 hours and the average velocity for each cell was plotted as a distribution profile.

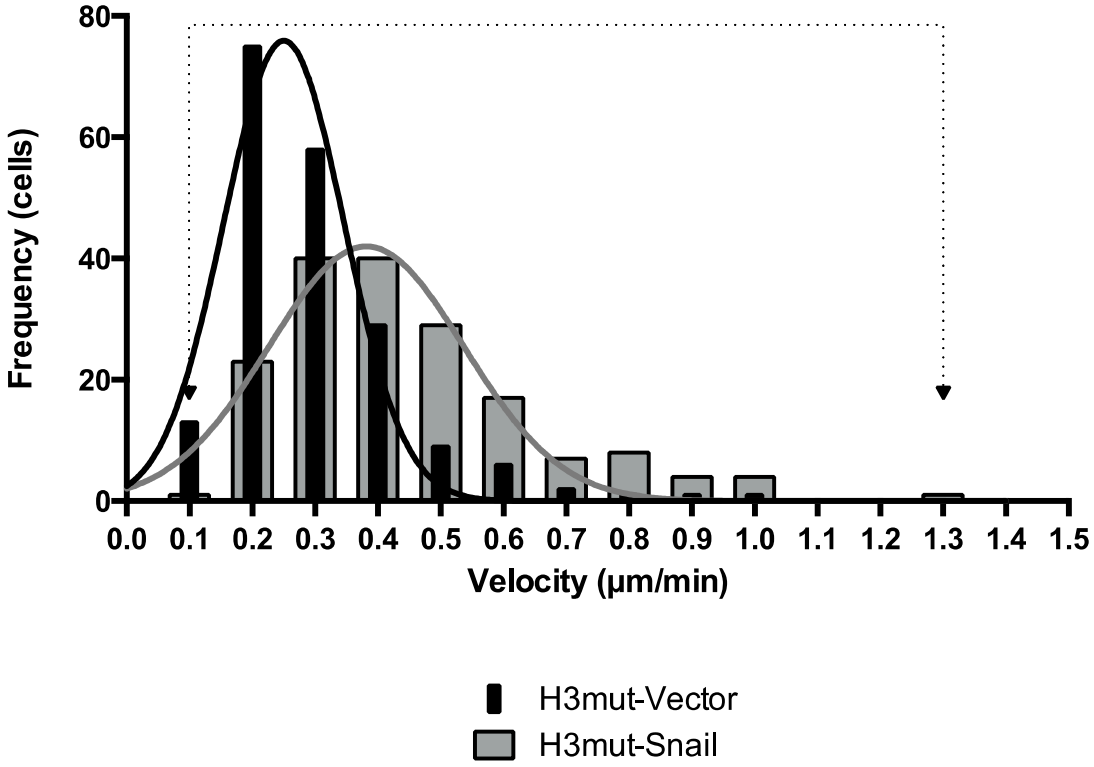

Figure 2.4: Migratory advantage through transwell membranes conferred by Snail expression increases with decreasing pore size. Migration assay results of H3mut-Snail cell movement through 8, 5, or 3 μm pore membranes reported as average cells/field. 100 fields were analyzed.

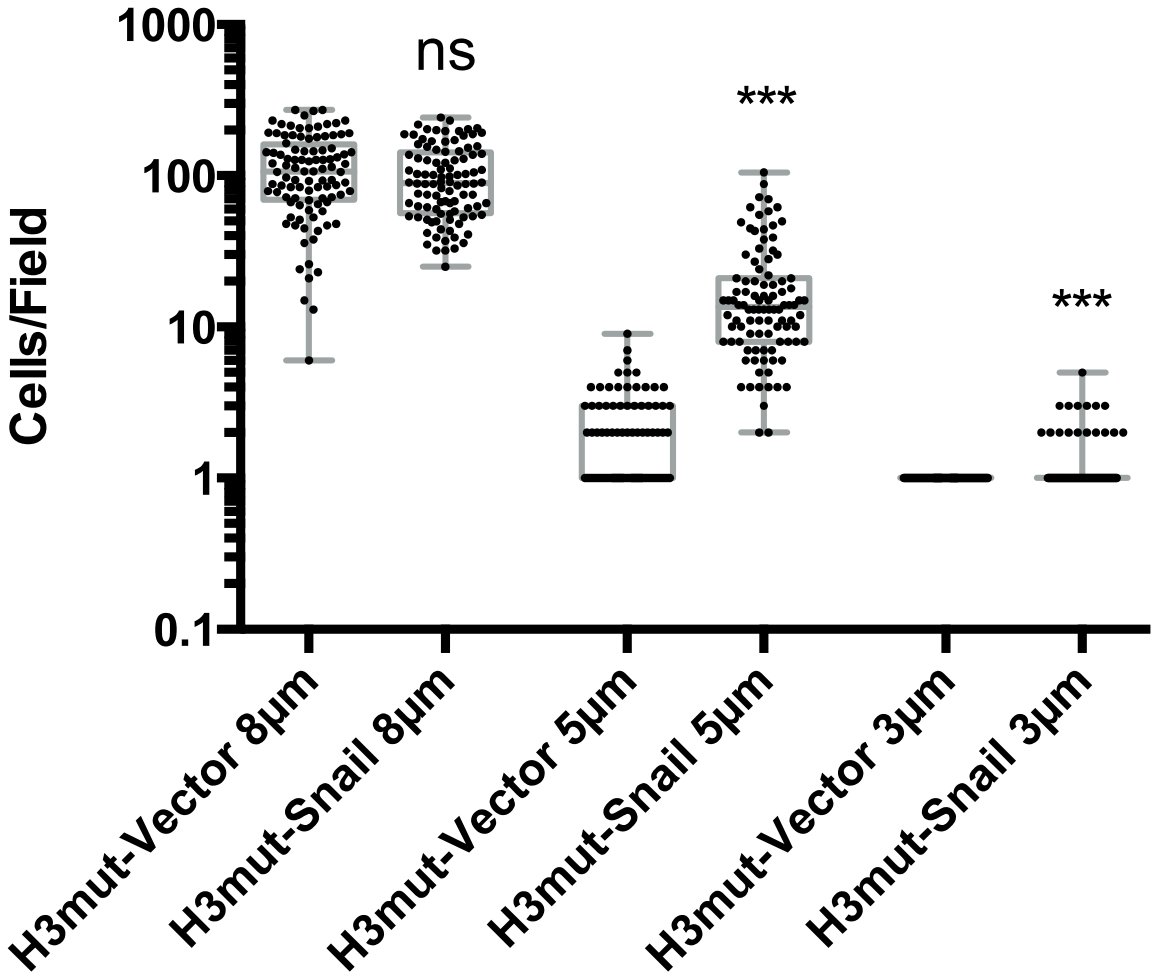

Figure 2.5: Selection schematic used to enrich highly migratory cells. Cells are seeded into 6-well transwells containing basal growth medium in both upper and lower chambers. After 48 hours, cells that passed through to the bottom well are propagated until a sufficient quantity is obtained to repeat the process. To increase the selection pressure, cells are serially selected through 8, 5 then 3 μm pore membranes.

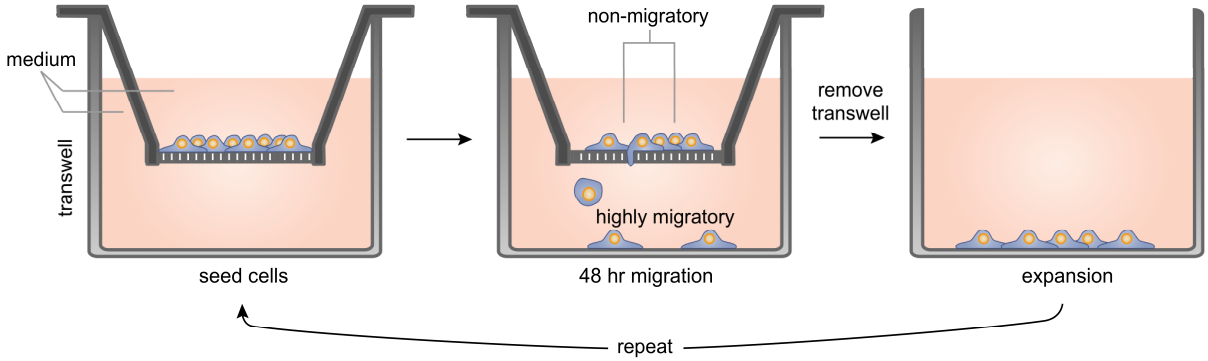

Figure 2.6: H3mut- and H4-Snail/Vector cells selected through increasingly smaller pores have enhanced migratory capacity. Cells were seeded in 12-well transwells using 8, 5 and 3 μm pore sizes with basal growth medium in both chambers. After migration, cells were fixed and stained for quantification.

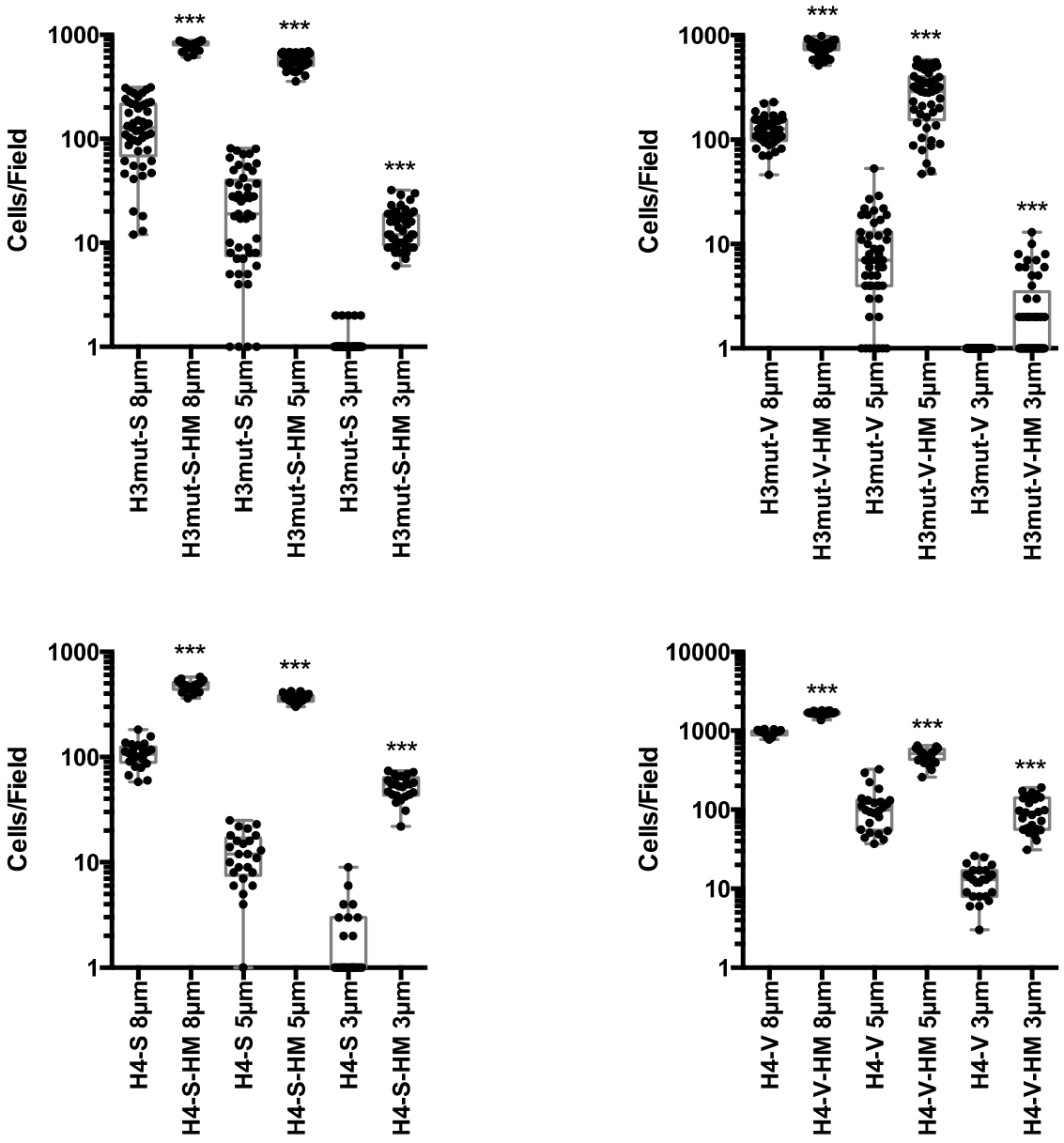

Figure 2.7: Selection of H3-Snail/Vector and A549-Snail/Vector cells through increasingly smaller pore sizes results in isolation of a highly migratory subpopulation. Isolated cells were seeded in 12-well transwells as before and migration quantified by microscopy and ImageJ analysis.

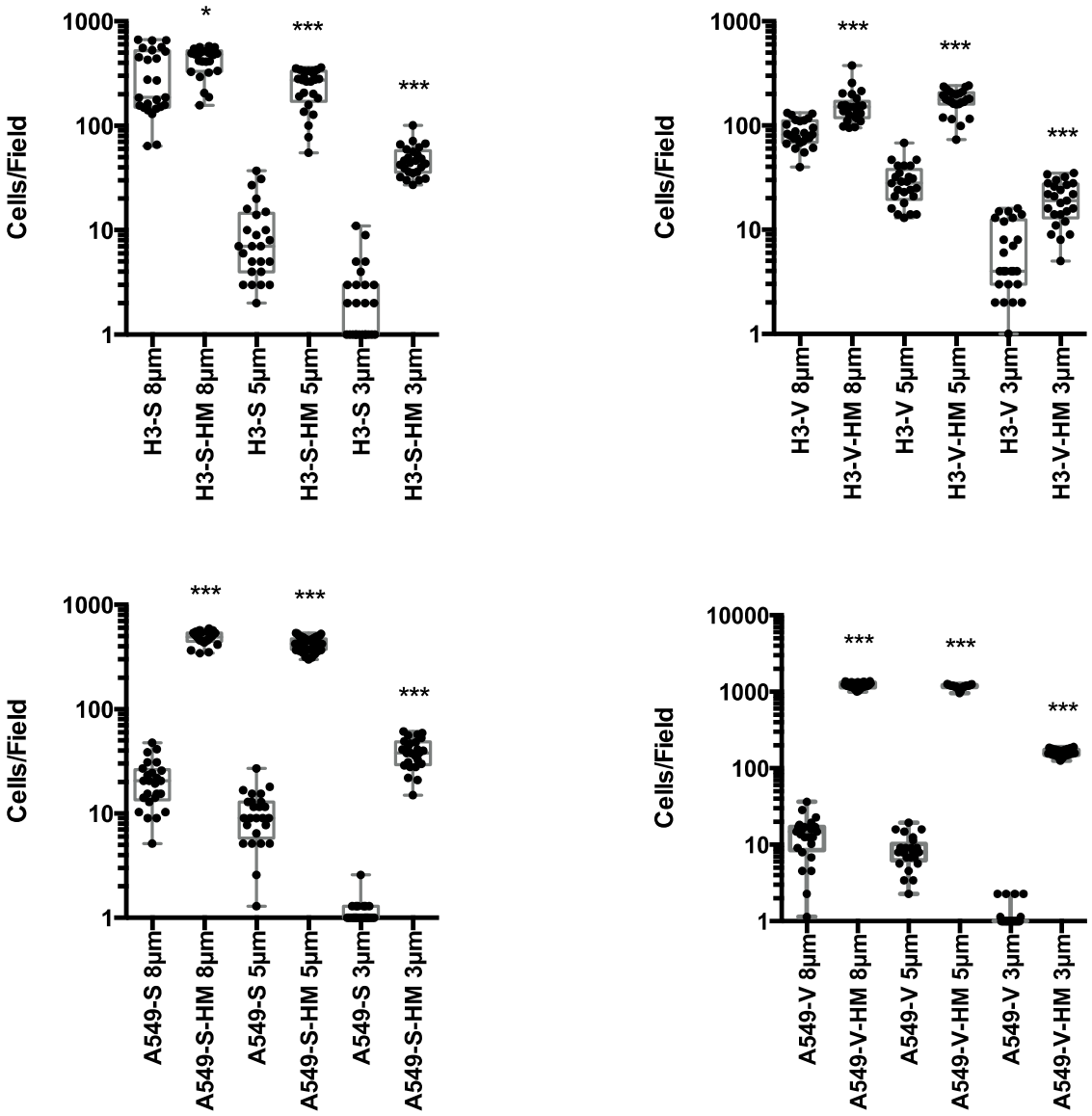

Figure 2.8: Dual live/dead cell stain reveals cell viability is compromised soon after migration through 3 μm pores without prior selection. After migration, cells in the bottom chamber were stained with NucRed (all cells) and DAPI (dead cells). Fluorescence imaging took place within 2 hours following staining. This representative image is of H3mut-Vector cells. 200x total magnification. Scale bar equals 50 μm.

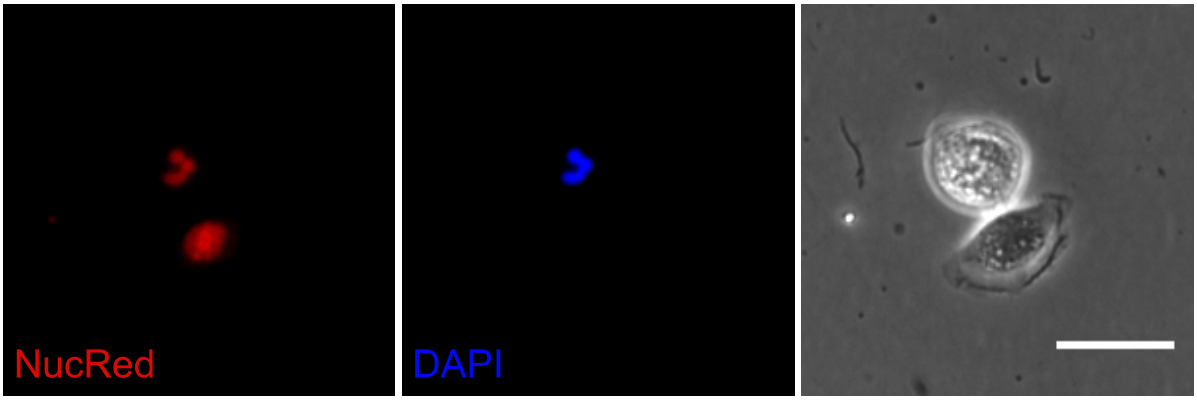

Figure 2.9: Without prior selection, less than 50% of cells maintain viability after passing through 3 μm pores. The percentage of live cells in the bottom chamber after a migration assay through 8 or 3 μm pores was calculated as the total cells minus the dead cells divided by the total cells. At least 25 different fields were analyzed. Error bars are standard deviation from four independent experiments.

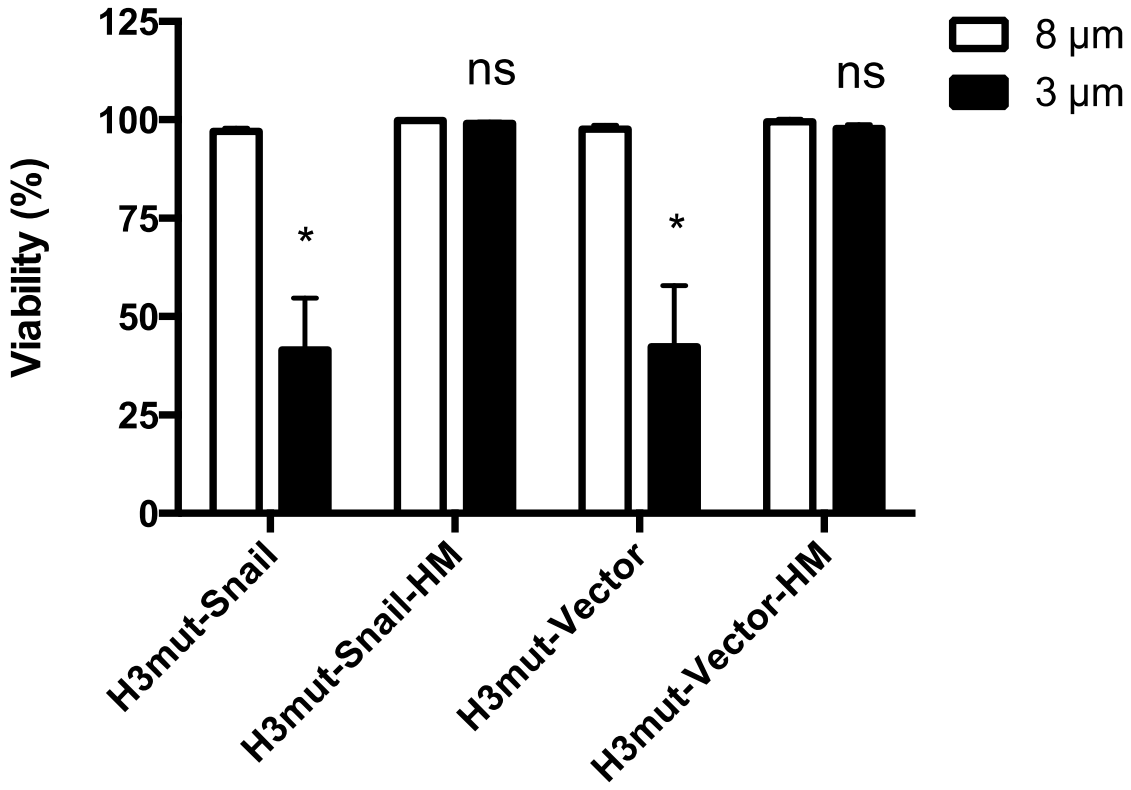

Figure 2.10: Highly migratory cells have characteristics that allow for enhanced invasion. Inverted invasion assay showing the invasion ratio (number of cells invaded divided by number of non-invasive cells). Error bars represent standard error of the mean.

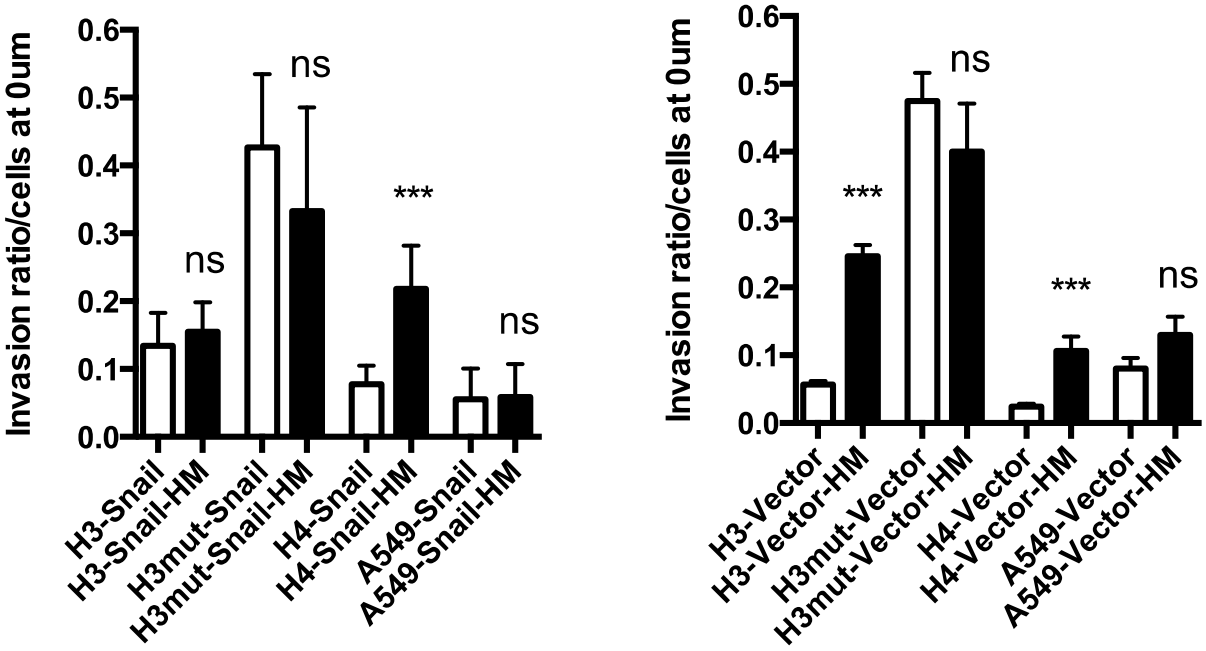

Figure 2.11 Highly migratory phenotype remains stable eight weeks post-selection. Migration assay showing fold-change in the number of cells/field that migrated to the bottom chamber at week 1 (empty bars) and week 8 (filled bars) after selection. Migration through 3 μm pores shown for both H4-HM and H3mut-HM Snail/Vector pairs. At least 25 fields were analyzed. Error bars represent standard error of the mean.

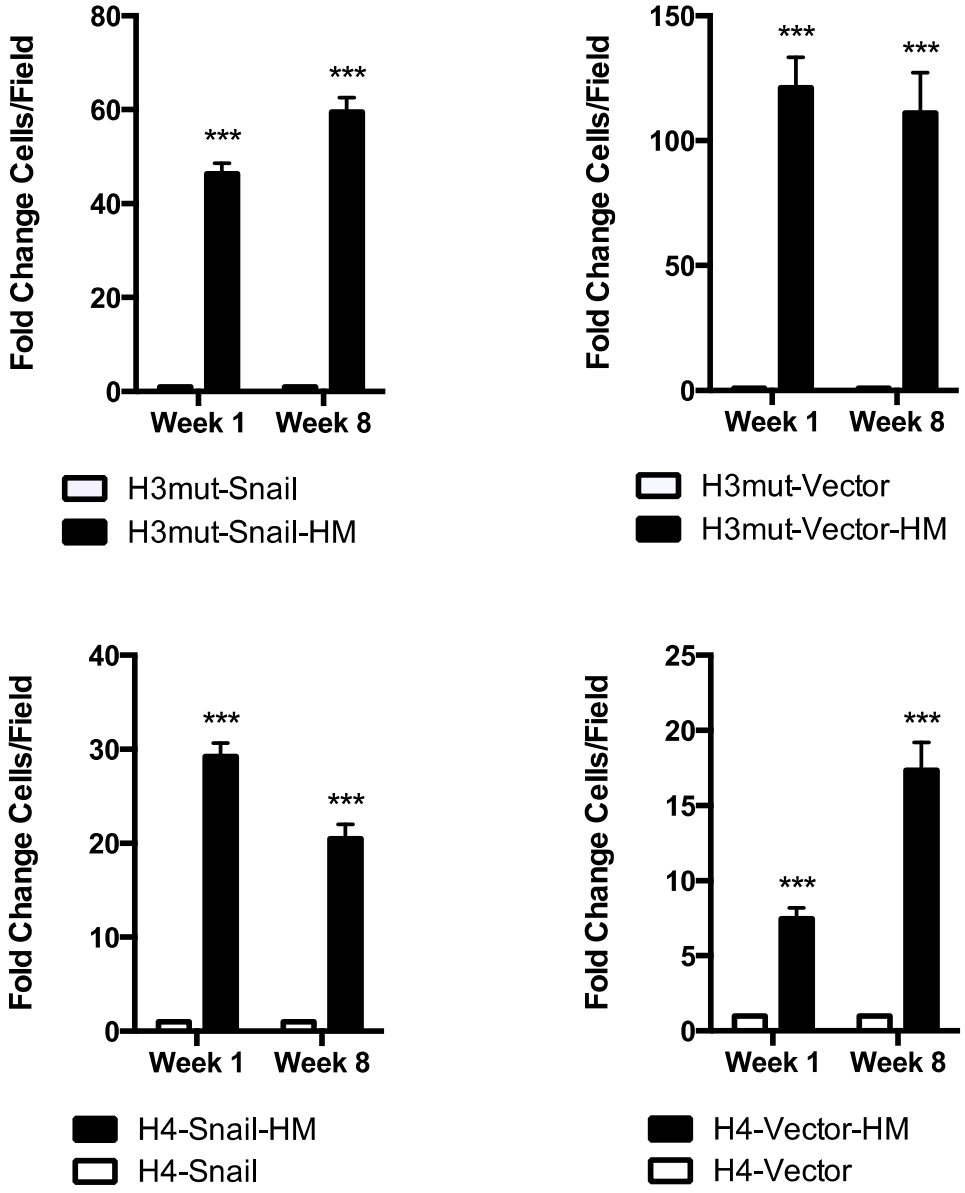

Figure 2.12: Highly migratory phenotype remains stable at least eight weeks post-selection at all pore sizes. Migration assay showing fold-change in the number of cells/field that migrated to the bottom chamber at week 1 (empty bars) and week 8 (filled bars) after selection. Error bars represent standard error of the mean.

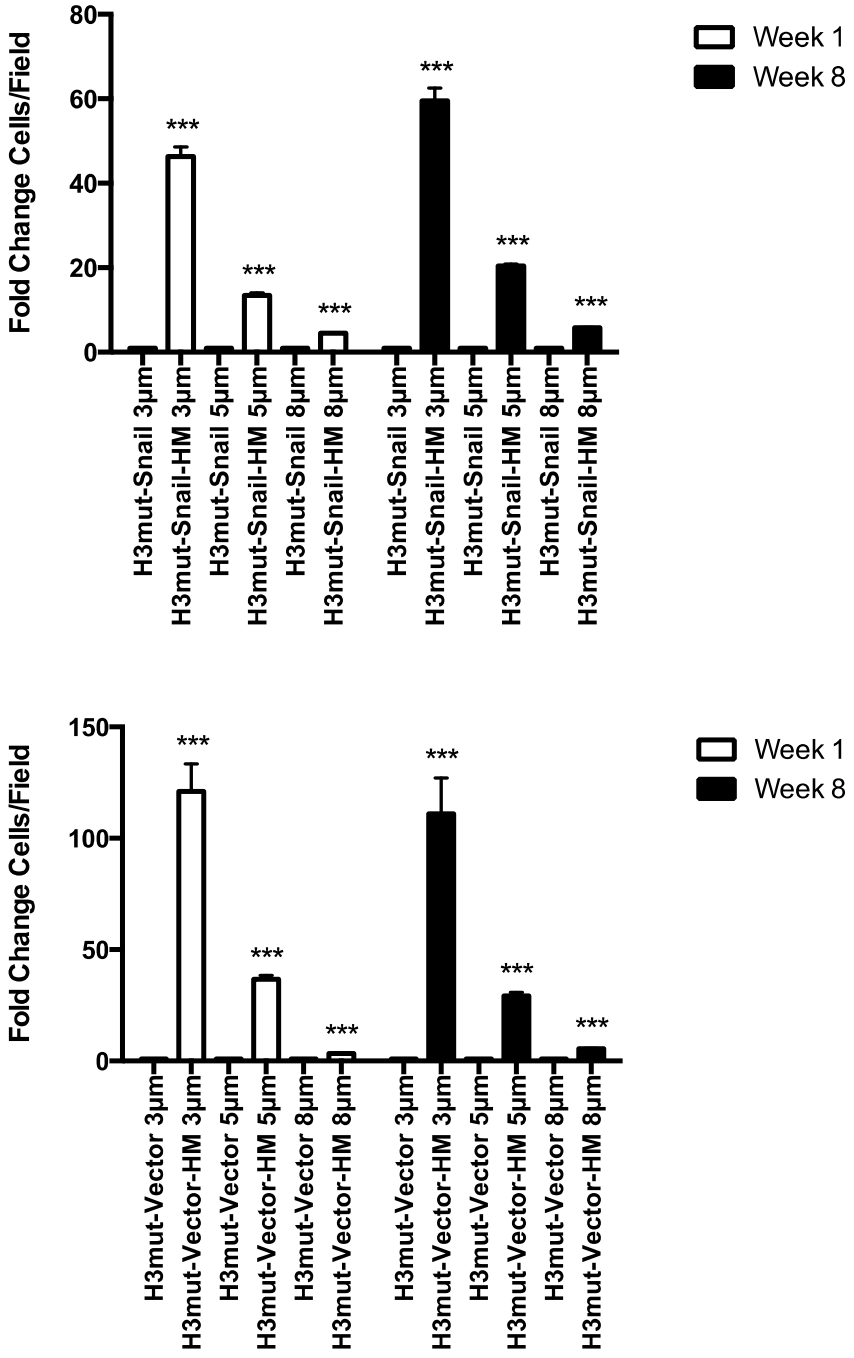

Figure 2.13: Selection results in increased persistence of cells in the mouse lung following tail vein injection. $5x10^5$ H3mut-Snail or H3mut-Snail-HM cells were injected intravenously. Lungs were harvested after 72 hours and DNA extracted. Quantitative PCR was performed using human and mouse specific primers and C_t values converted to (%) human cells using published methods (30). Error bars represent standard deviation; n=8 mice per group.

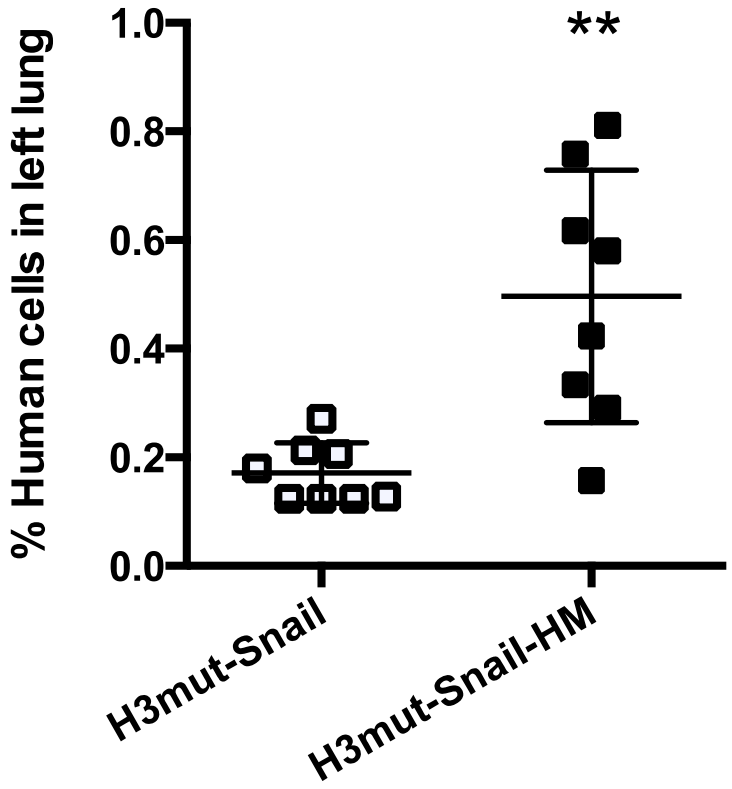

Figure 2.14: Increased Snail expression is not a consequence of selection through microporous membranes. (a) Western blot for Snail protein shows no significant change in protein expression. (b) Densitometry of blots shown in (a). Data representative of three independent western blots.

A)

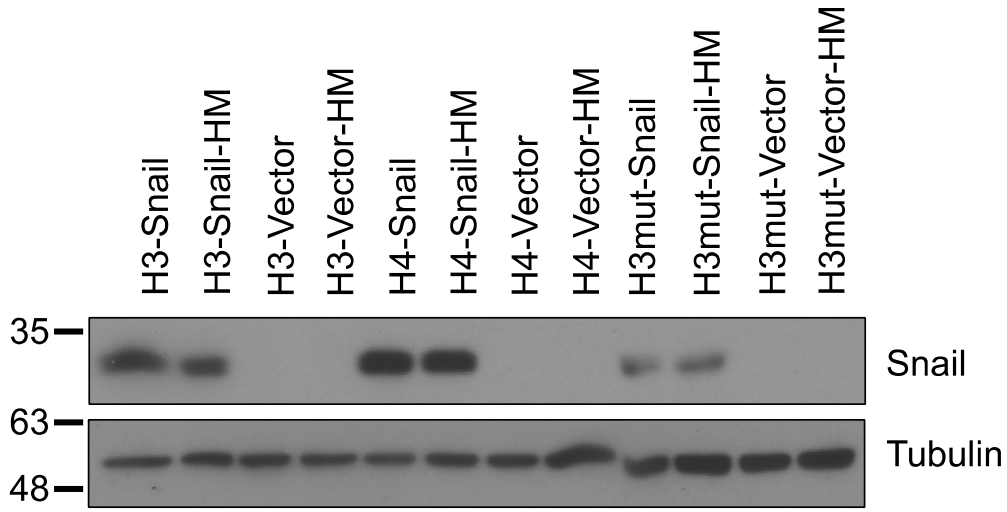

B)

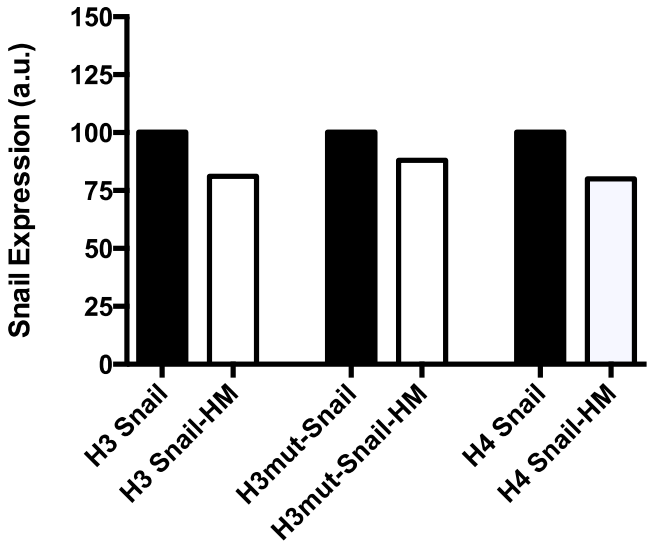

Figure 2.15: Photomicrograph of Snail-expressing cells before and after selection showing the overlaid outlines produced in ImageJ on top of phase contrast images. Cells without clear borders, or that were on edges were excluded. 200x total magnification. Scale bars are 50 μm.

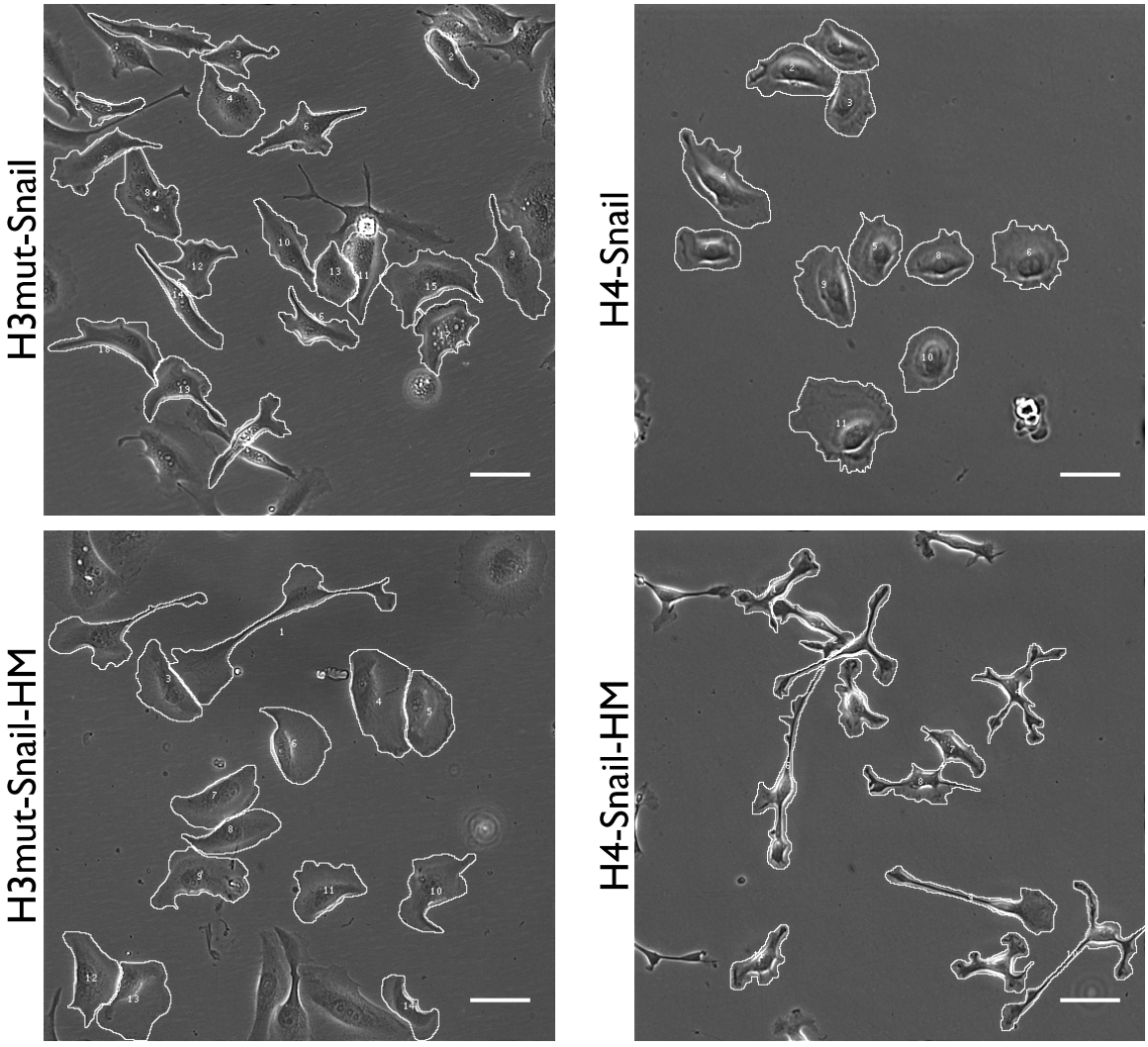

Figure 2.16: Selection through small pores results in cells having greater ability to spread or stretch. The area and Feret's diameter (maximum distance between two edges) of each cell was determined using ImageJ. Individual cell values were averaged. Error bars represent standard error of the mean. At least 45 cells were analyzed per group.

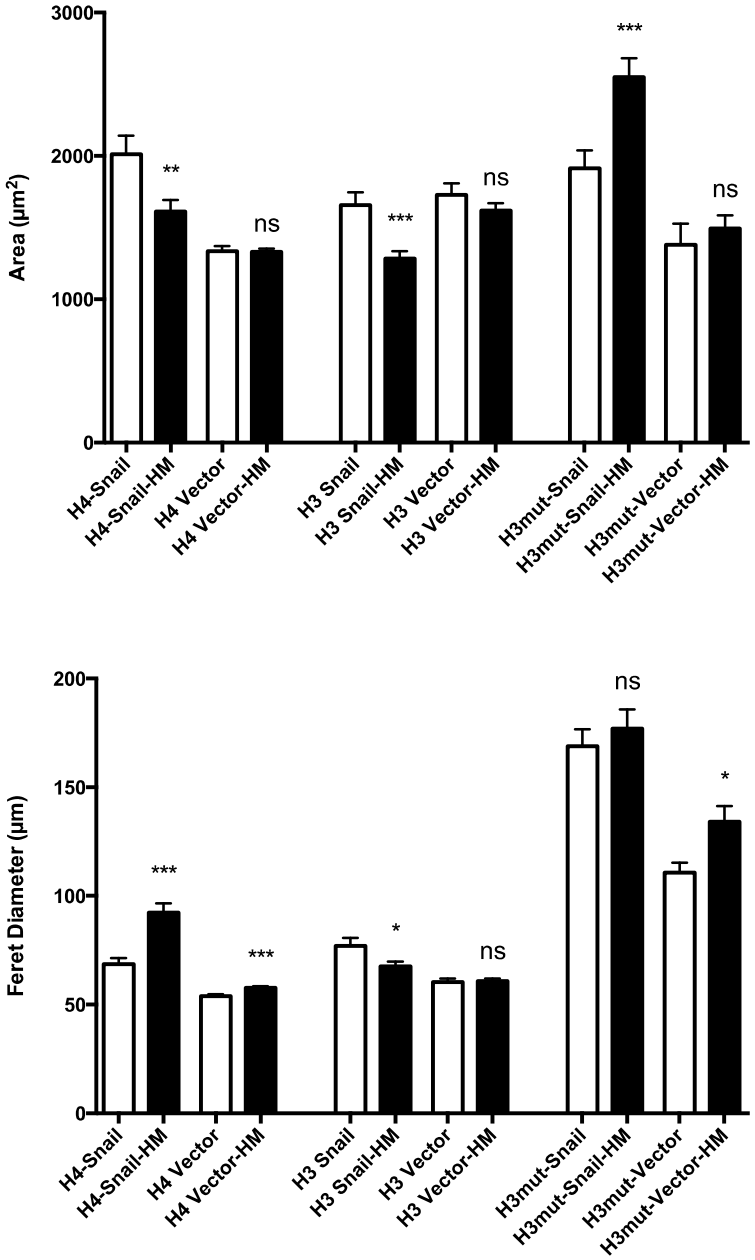

Figure 2.17: Selection does not bias nuclear size as determined by post-migration size analysis. Graphical representation of the nuclear area as determined by Lamin B1 immunofluorescence, showing no significant difference between H3mut selected and unselected cells. H4-Snail-HM and H4-Vector-HM have smaller or larger nuclear area, respectively. Error bars represent standard error of the mean. At least 60 cells were analyzed per group.

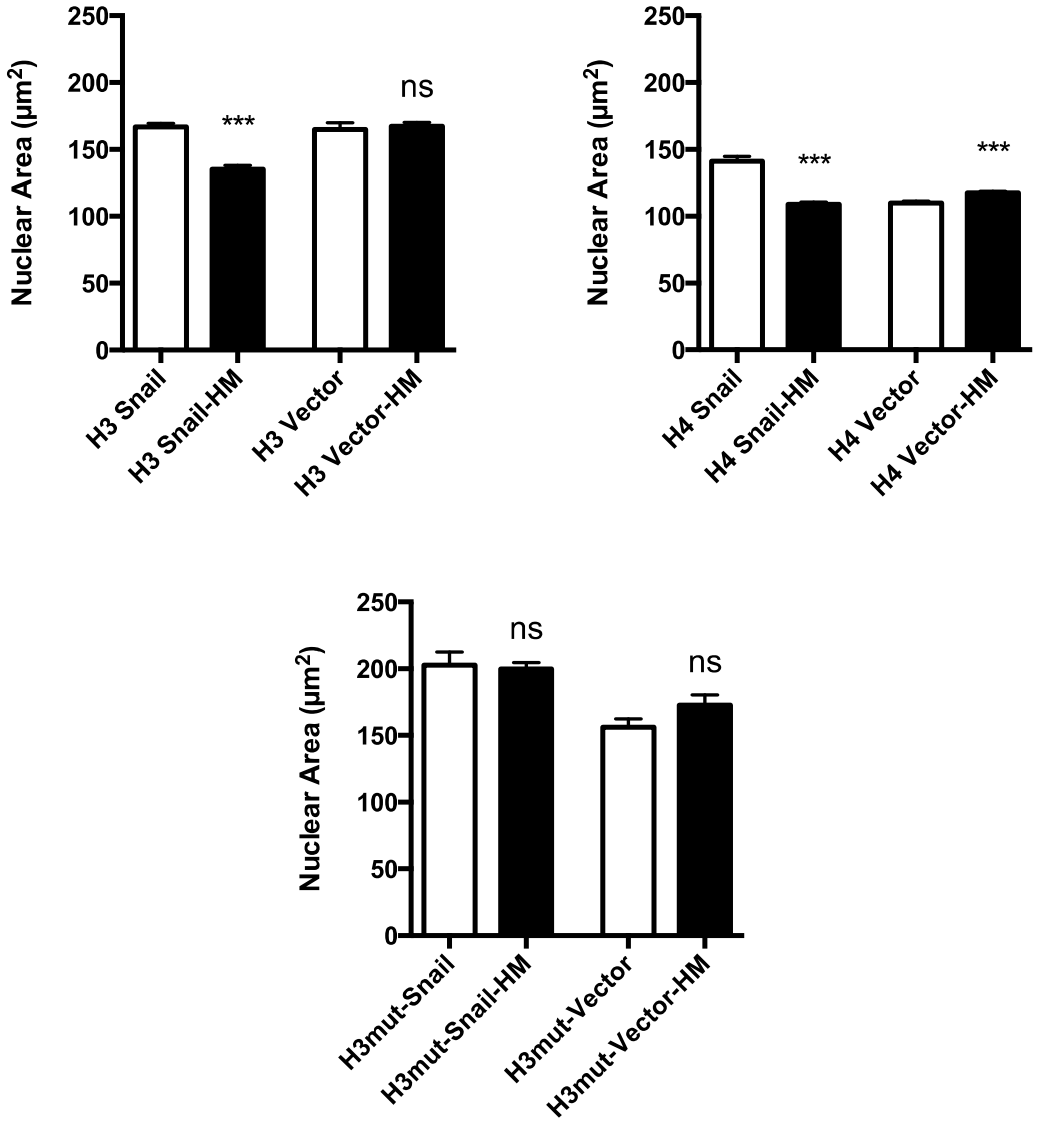

Figure 2.18: Deformability Cytometry (DC) reveals opposite deformability phenotypes coinciding with highly migratory behavior. Error bars represent SEM.

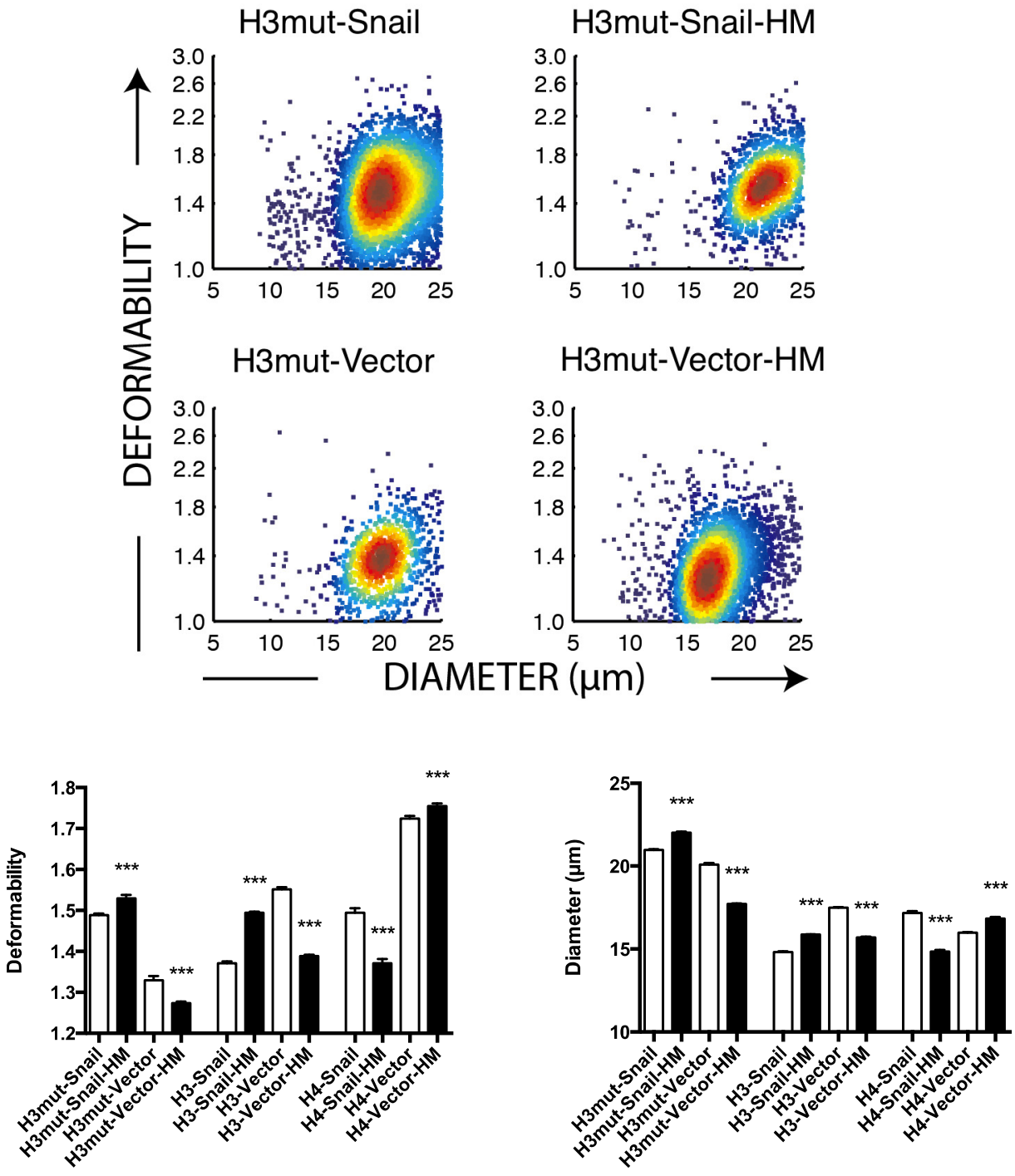

Table 2.2: Summary of biophysical properties in highly migratory cell lines displayed as fold-change over unselected (delta, ∆).

Cell Line	∆Deformability (DC)	∆Diameter (DC)	∆Spreading
H3-Snail-HM	+8.97%	+7.09%	Area: -22.51% Feret: -12.26%
H3-Vector-HM	-10.5%	-10.2%	Area: -6.30% Feret: +0.679%
H3mut-Snail-HM	+2.69%	+4.86%	Area: +33.24% Feret: +4.86%
H3mut-Vector-HM	-4.14%	-11.8%	Area: +8.26% Feret: +21.1%
H4-Snail-HM	-8.24%	-13.5%	Area: -19.88% Feret: +34.51%
H4-Vector-HM	+1.74%	+5.44%	Area: -0.374% Feret: +7.09%

Figure 2.19: Atomic force microscopy measures stiffness in motile cells. Selected and unselected cells were plated in 60 mm dishes and analyzed with an atomic force microscope. Force measurements were taken above the nucleus at approximately 500 nm depth, and the force-displacement curves generated were converted to Young's moduli (E) as a measure of cell stiffness. AFM measurements were obtained from at least 60 cells.

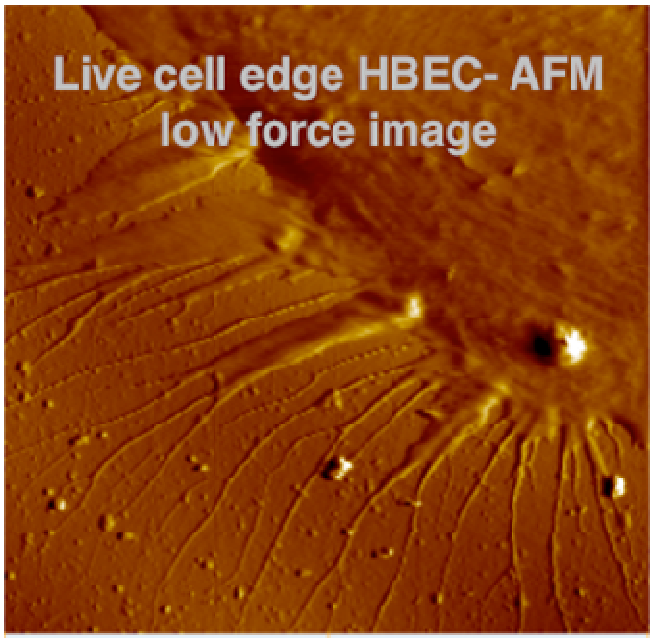

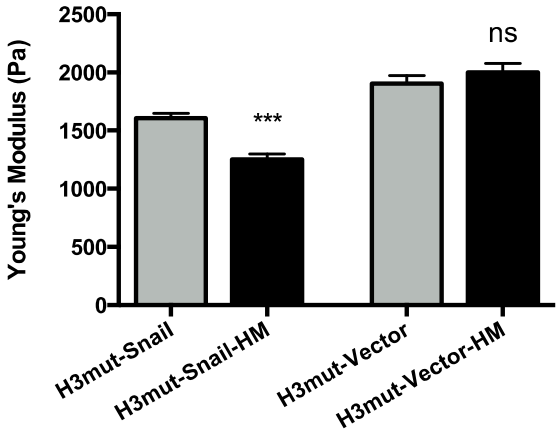

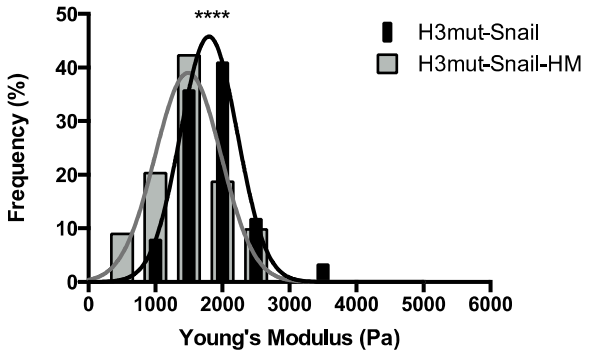

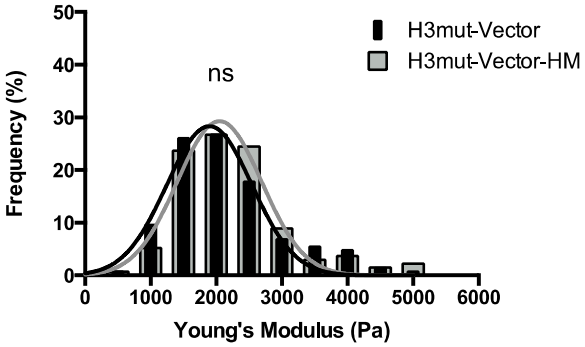

Figure 2.20a: Actin filament structures are abundant in highly migratory cells that express Snail. Fluorescence micrographs showing F-actin (green) and nucleus (blue). H3mut-Snail cells show small lamellipodia compared to H3mut-Snail-HM (Figure 2.22b). 200x total magnification. Scale bar is 50 microns.

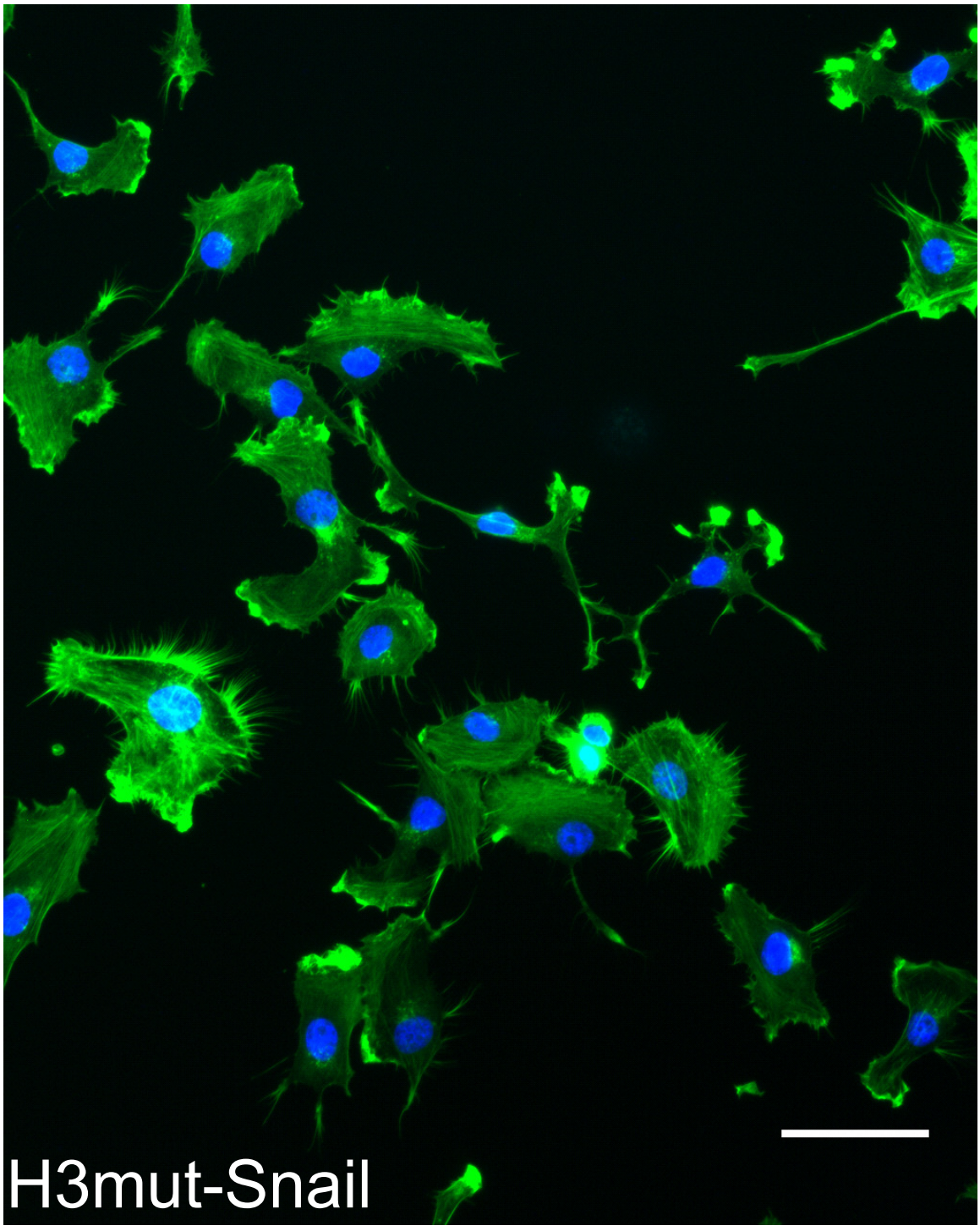

Figure 2.20b: Actin filament structures are abundant in highly migratory cells that express Snail. Fluorescence micrographs showing F-actin (green) and nucleus (blue). H3mut-Snail-HM cells have ventral actin-arcs located in the lamellipodia, which are absent in the unselected cells. 200x total magnification. Scale bar is 50 microns.

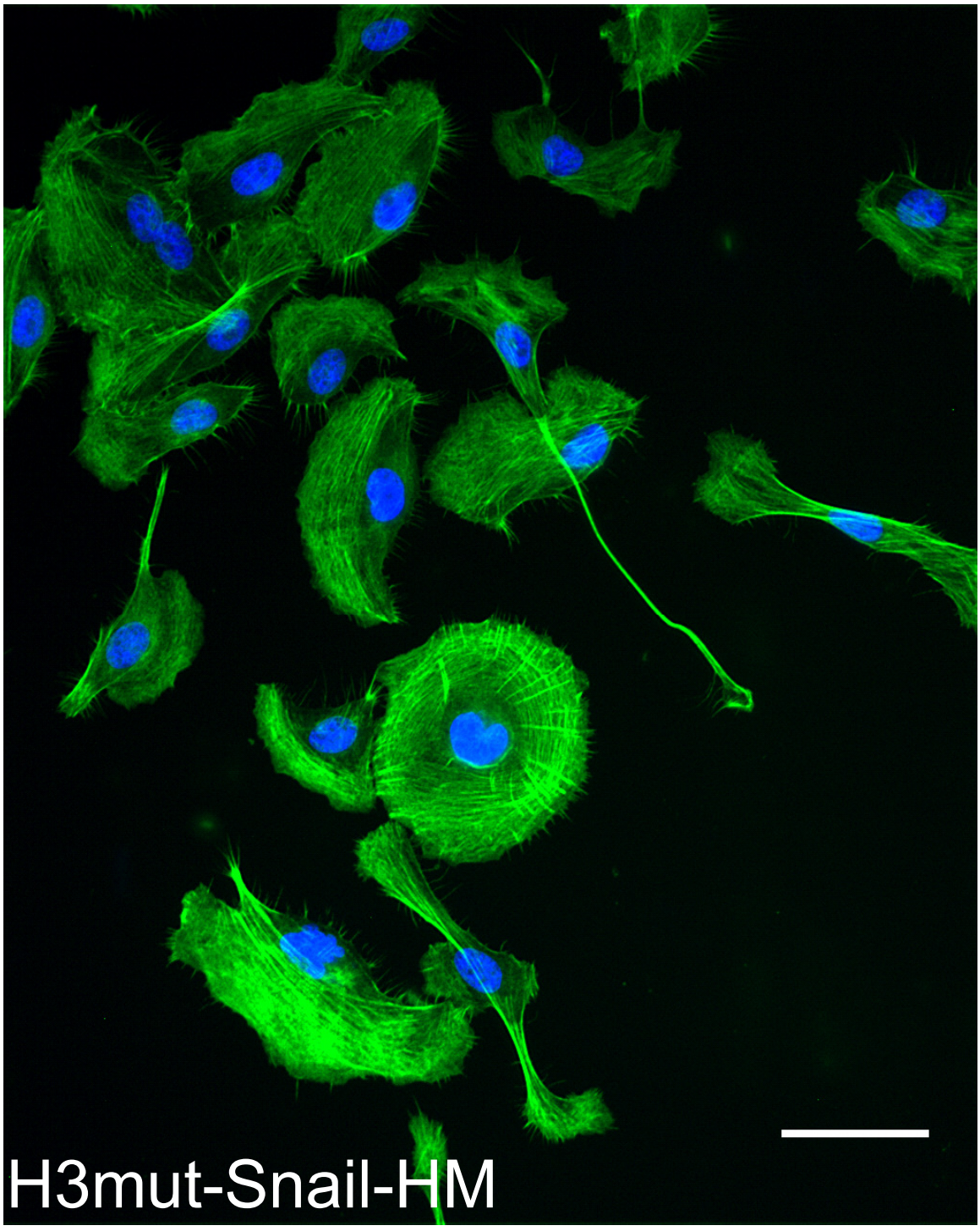

Figure 2.20c: Actin reorganization is apparent in highly migratory cells that express Snail. Fluorescence micrographs showing F-actin (green) and nucleus (blue). 200x total magnification. Scale bar is 50 μm.

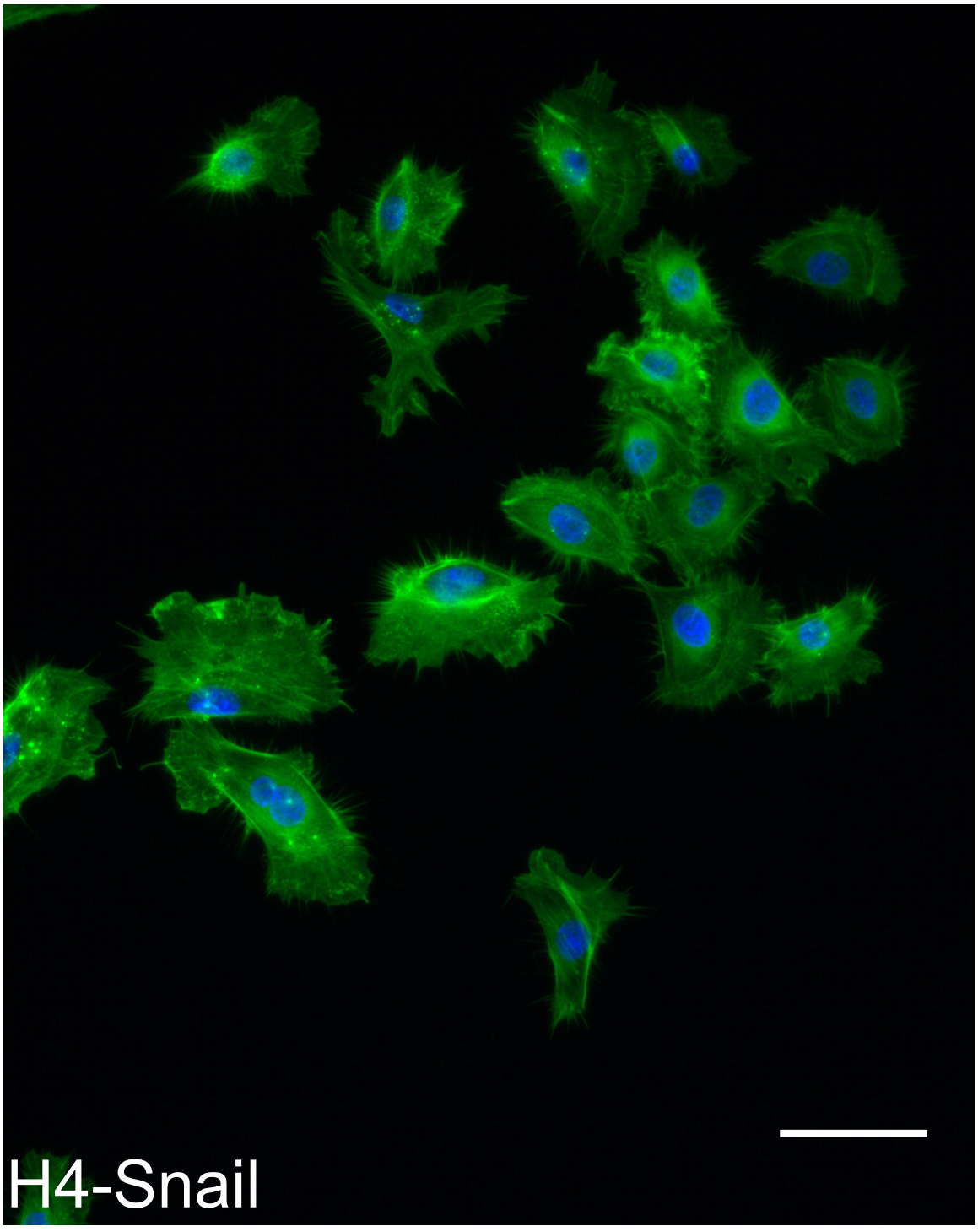

Figure 2.20d: Actin reorganization is apparent in highly migratory cells that express Snail. Fluorescence micrographs showing F-actin (green) and nucleus (blue). H4-Snail-HM cells show long protrusions. 200x total magnification. Scale bar is 50 μm.

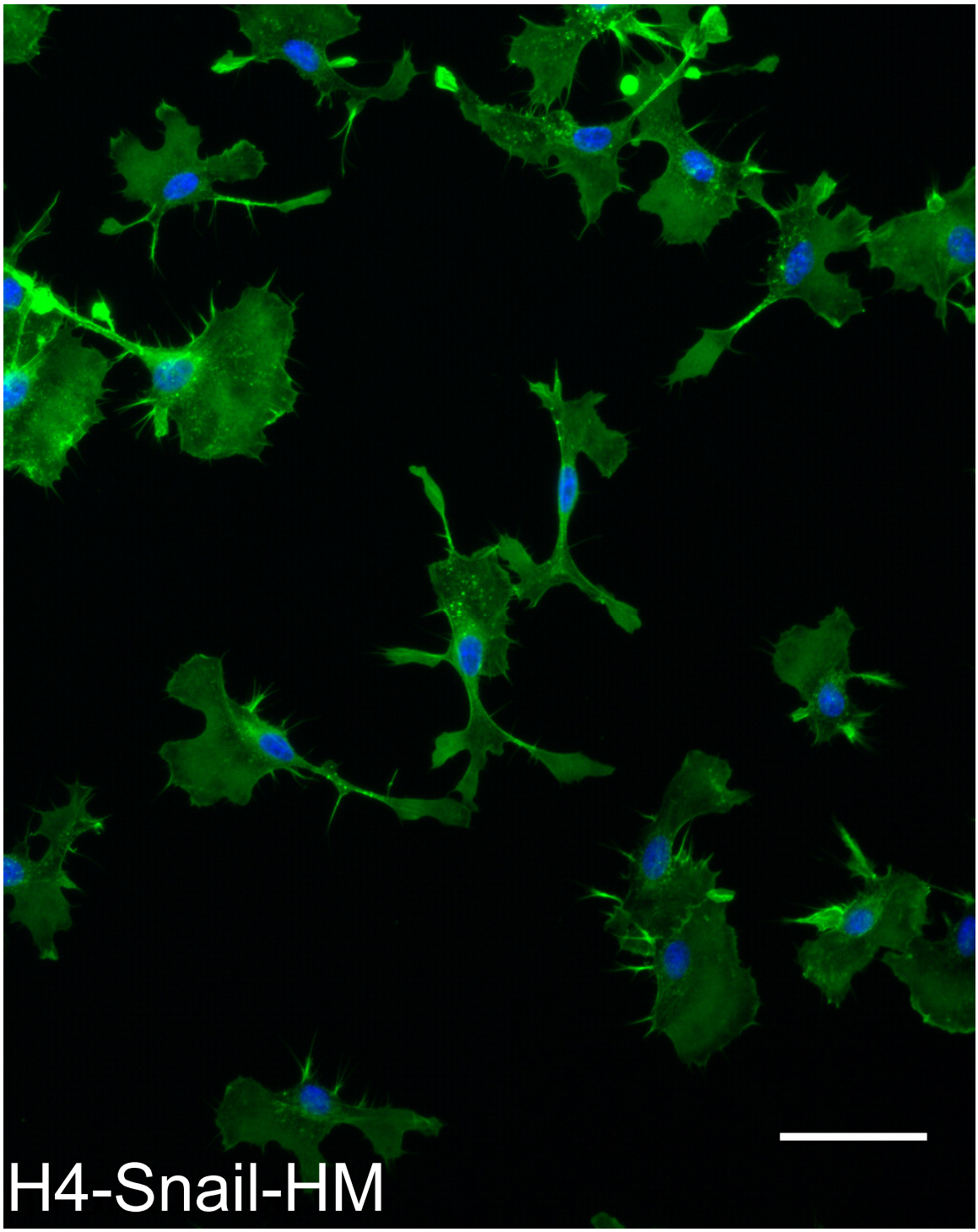

Figure 2.21a: Highly migratory vector control cells do not exhibit similar changes to the actin cytoskeleton as seen in HBEC-Snail cells. The actin cytoskeleton (green) and nucleus (DAPI, blue) shown for H3mut-Vector cells. Scale bar is 50 microns. 200x total magnification.

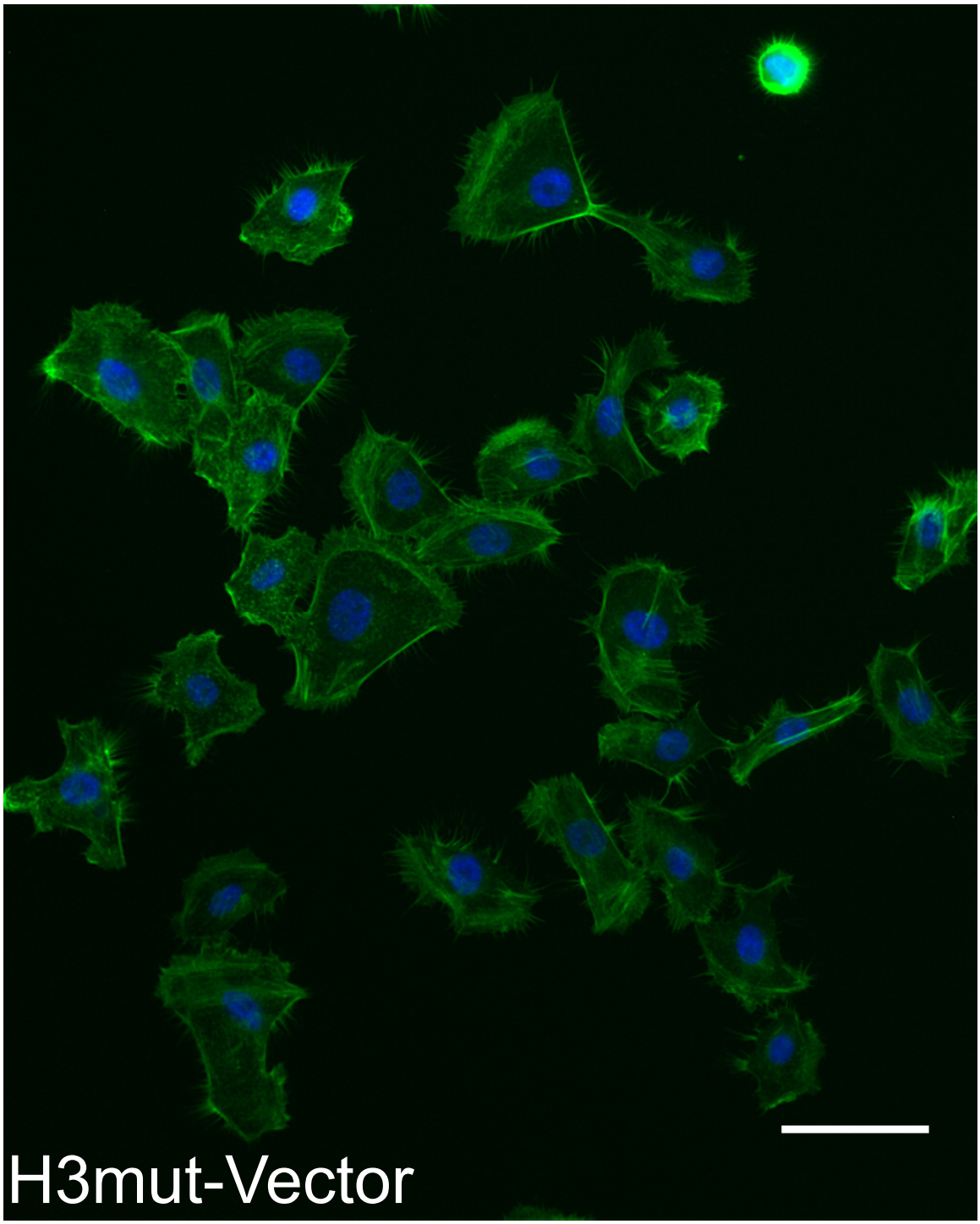

Figure 2.21b: Highly migratory vector control cells do not exhibit similar changes to the actin cytoskeleton as seen in HBEC-Snail cells. The actin cytoskeleton (green) and nucleus (DAPI, blue) shown for H3mut-Vector-HM. Scale bar is 50 μm. 200x total magnification.

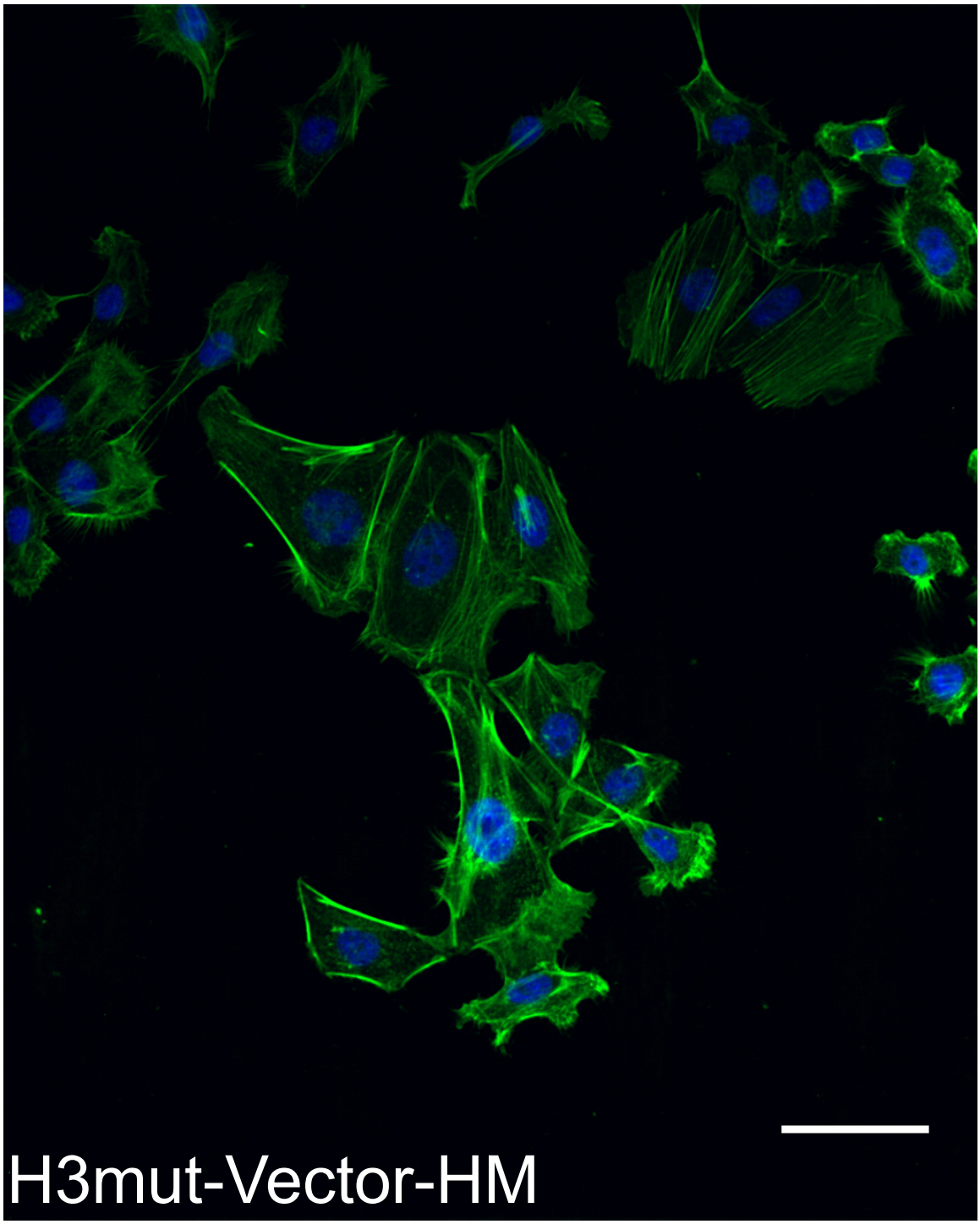

Figure 2.21c: Highly migratory vector control cells do not exhibit similar changes to the actin cytoskeleton as seen in HBEC-Snail cells. The actin cytoskeleton (green) and nucleus (DAPI, blue) shown for H4-Vector cells. Scale bar is 50 microns. 200x total magnification.

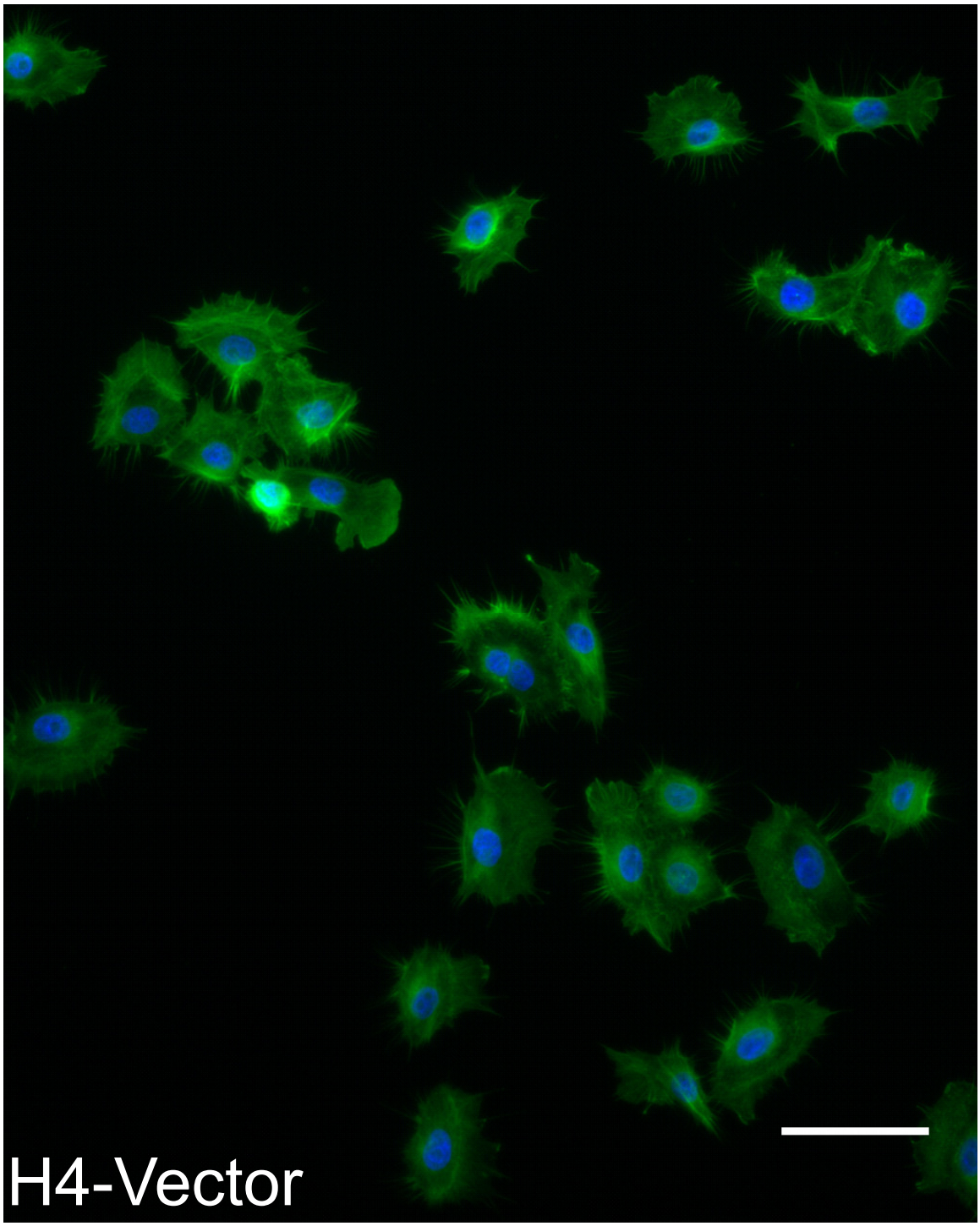

Figure 2.21d: Highly migratory vector control cells do not exhibit similar changes to the actin cytoskeleton as seen in HBEC-Snail cells. The actin cytoskeleton (green) and nucleus (DAPI, blue) shown for H4-Vector-HM cells. Scale bar is 50 microns. 200x total magnification.

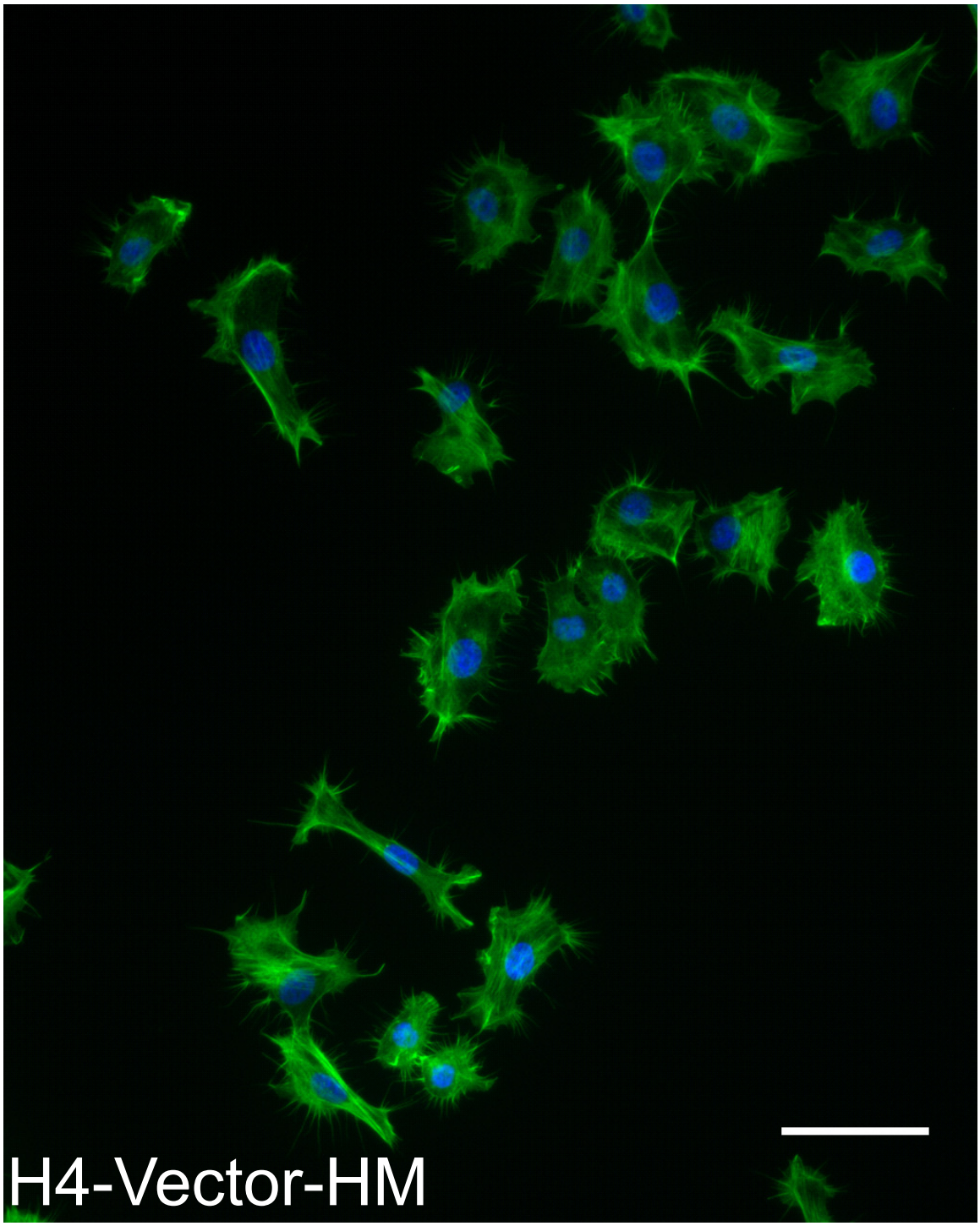

Figure 2.22a: Activated myosin localizes to F-actin filaments in highly migratory cells that express Snail. Immunofluorescence of phospho-myosin light chain II (pMLC2) in H3mut-Snail cells shows a perinuclear localization. H3mut-Snail-HM cells show pMLC2 distributed to the cell periphery, localizing with the F-actin arcs. Cells counterstained with DAPI. 200x total magnification. Scale bar is 20 microns.

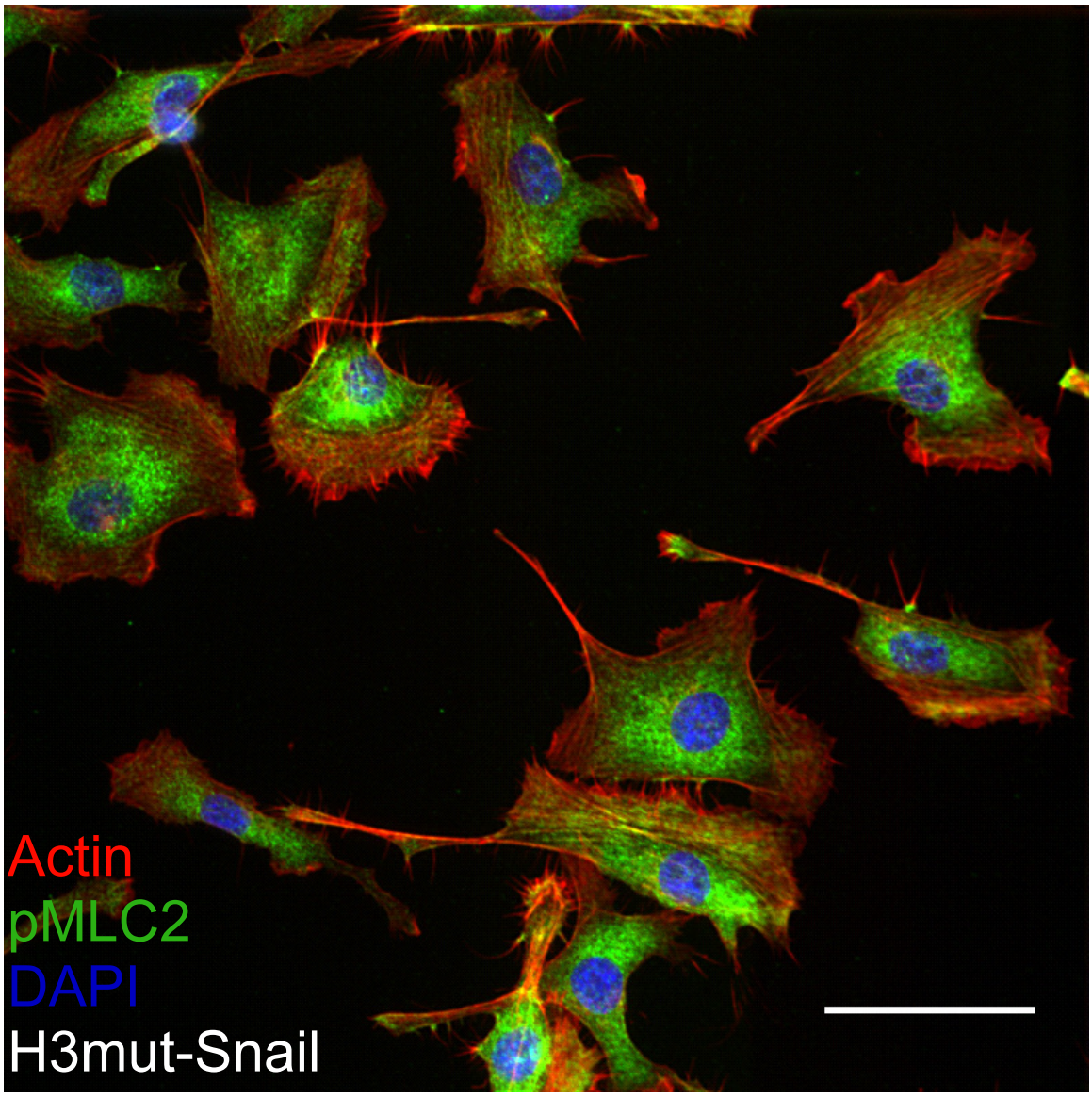

Figure 2.22b: Activated myosin localizes to F-actin filaments in highly migratory cells that express Snail. Immunofluorescence of phospho-myosin light chain II (pMLC2) in H3mut-Snail cells shows a perinuclear localization. H3mut-Snail-HM cells show pMLC2 distributed to the cell periphery, localizing with the F-actin arcs. Cells counterstained with DAPI. 200x total magnification. Scale bar is 20 microns.

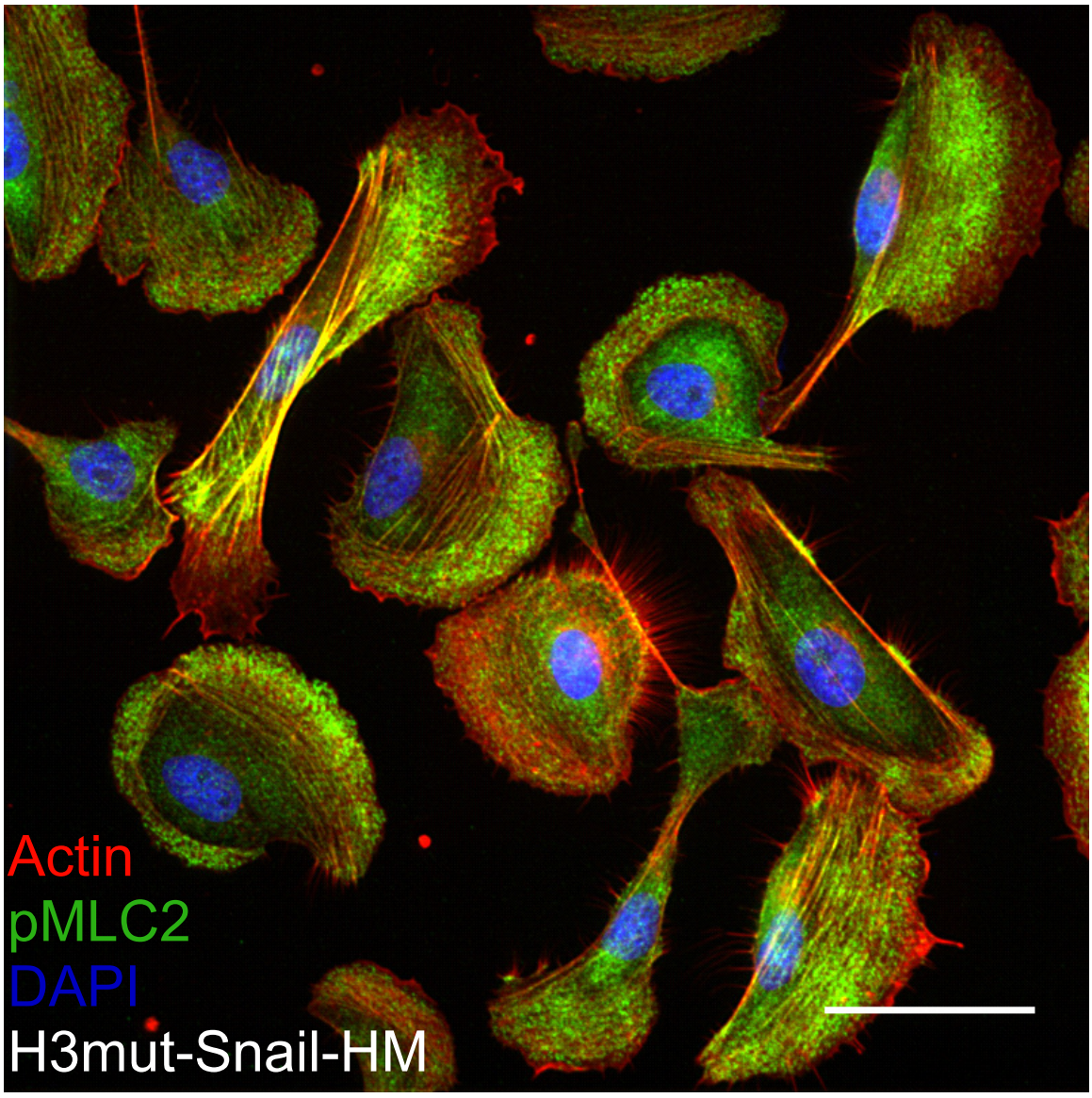

Figure 2.23a: Activated myosin localizes to actin filaments in the periphery of highly migratory cells that express Snail. Pixel intensity mapping of H3mut-Snail cells shows three distinct peaks for myosin (green), actin (red), and DAPI (blue). The line through the cells in the photomicrograph is represented on the X-axis as “distance” from left to right, and the Y-axis represents the corresponding pixel intensity value (unitless). Color arrows approximate peak maximums. 200x total magnification.

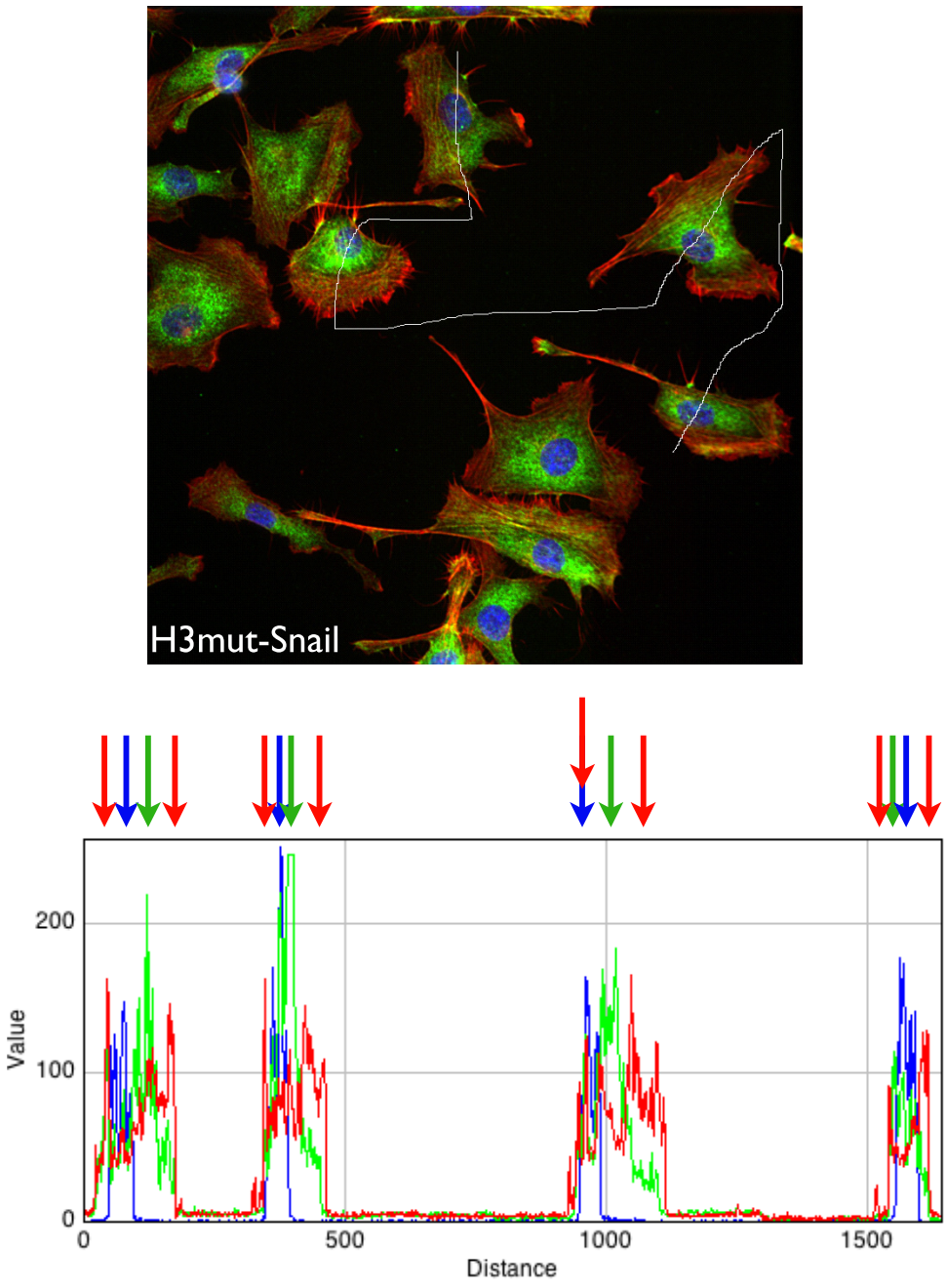

Figure 2.23b: Activated myosin localizes to actin filaments in the periphery of highly migratory cells that express Snail. Pixel intensity mapping of H3mut-Snail-HM cells shows overlap between actin (red) and myosin (green) peaks that are separate from the nuclear peak (blue). The line through the cells in the photomicrograph is represented on the X-axis as “distance” from left to right, and the Y-axis represents the corresponding pixel intensity value (unitless). Color arrows approximate peak maximums. 200x total magnification.

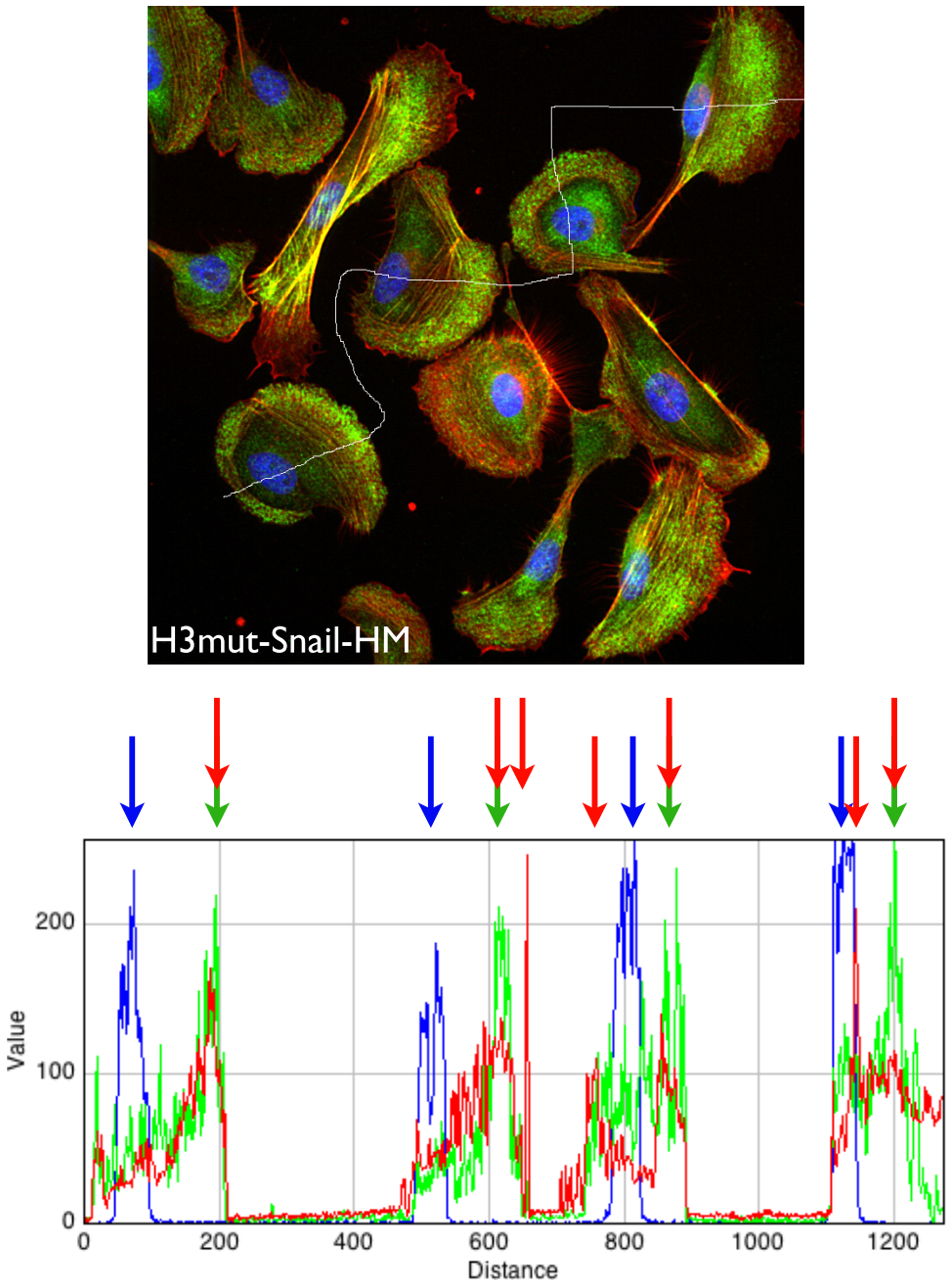

Figure 2.24: Highly migratory cells that over-express Snail have increased active Rac1. Pull-down assay for GTP-bound RhoA, Rac1 and Cdc42 show no change in GTP-bound RhoA or Cdc42, but ~2-fold increase in Rac1-GTP levels in H3mut-Snail-HM cells.

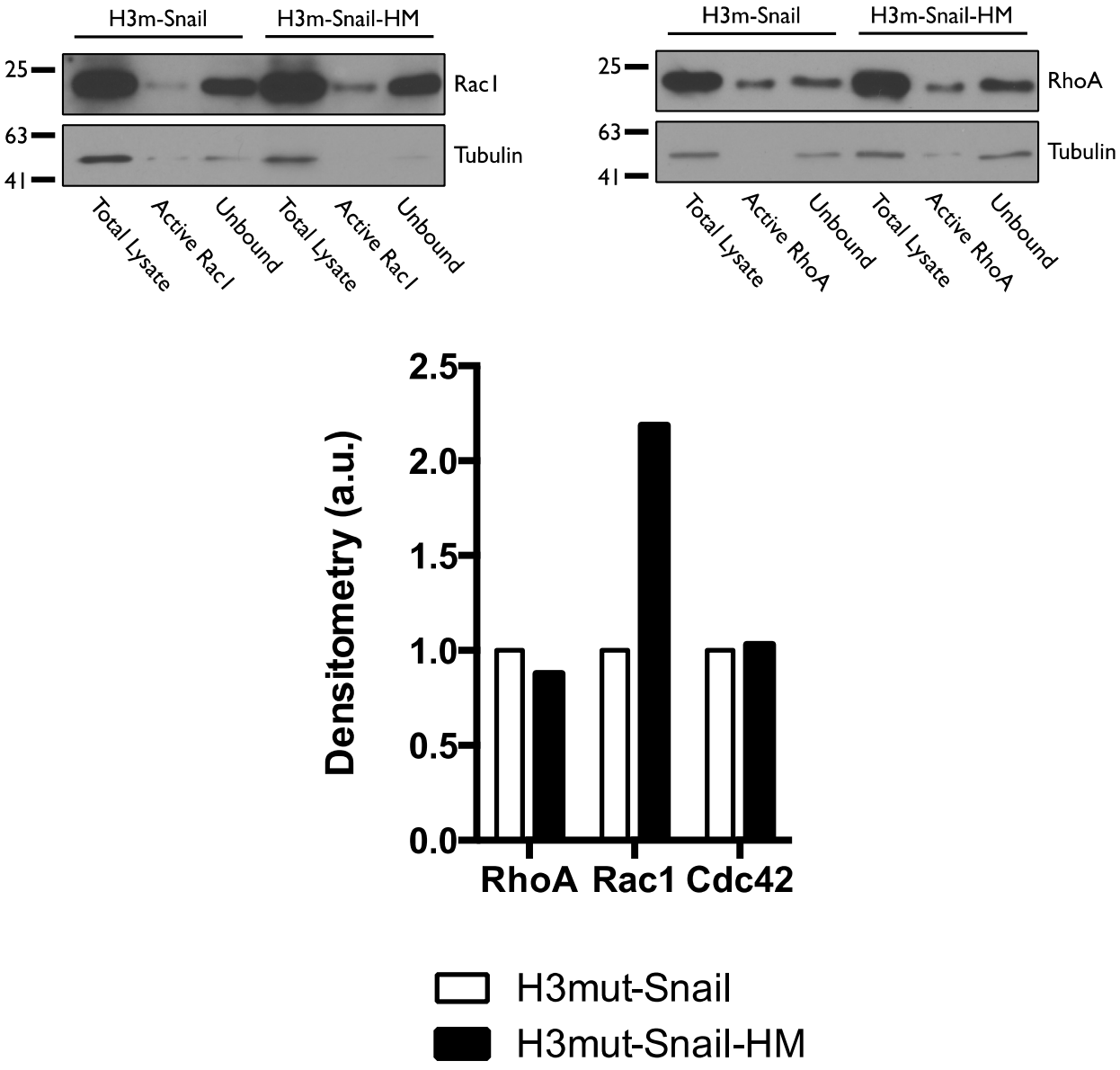

Figure 2.25: The Rac1 inhibitor NSC-23766 has concentration-dependent effects on cell proliferation. The effects on cell migration would likely be perturbed if proliferation was altered, and as such concentrations of inhibitor in migration assays were selected based on maximum inhibitor concentration with no effect on growth (10 μM).

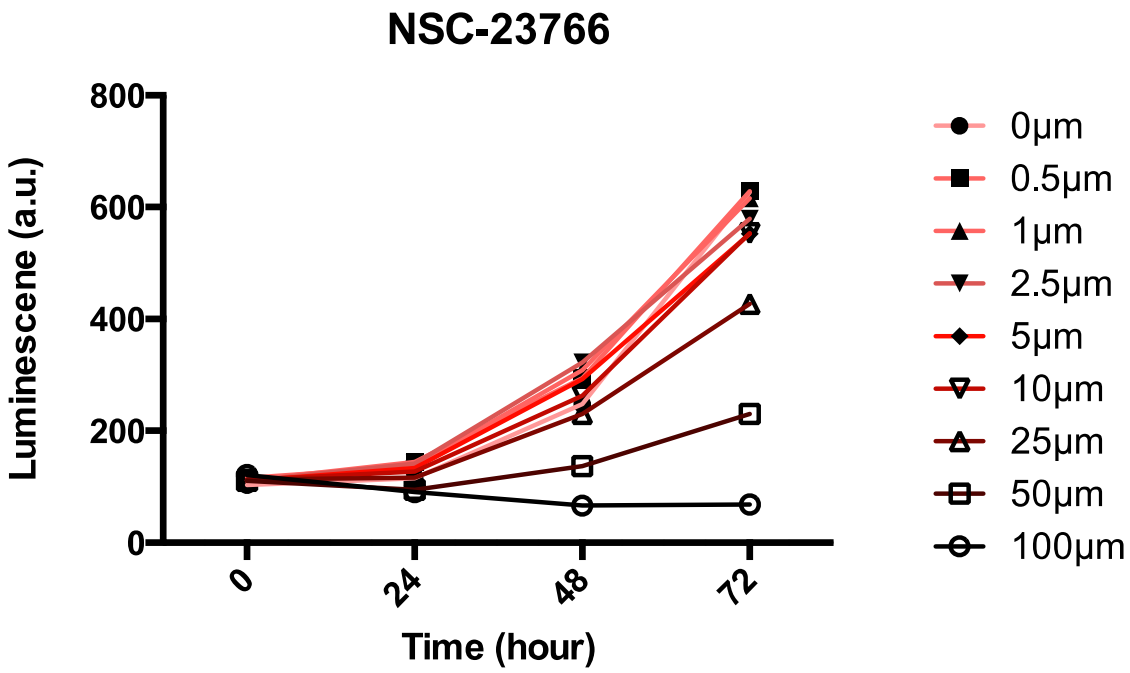

Figure 2.26: High migratory rate facilitated in part through Rac1 activity. Treatment with NSC-23766, an inhibitor of Rac1 activation, perturbs migration through 5 micron pores in highly migratory cells.

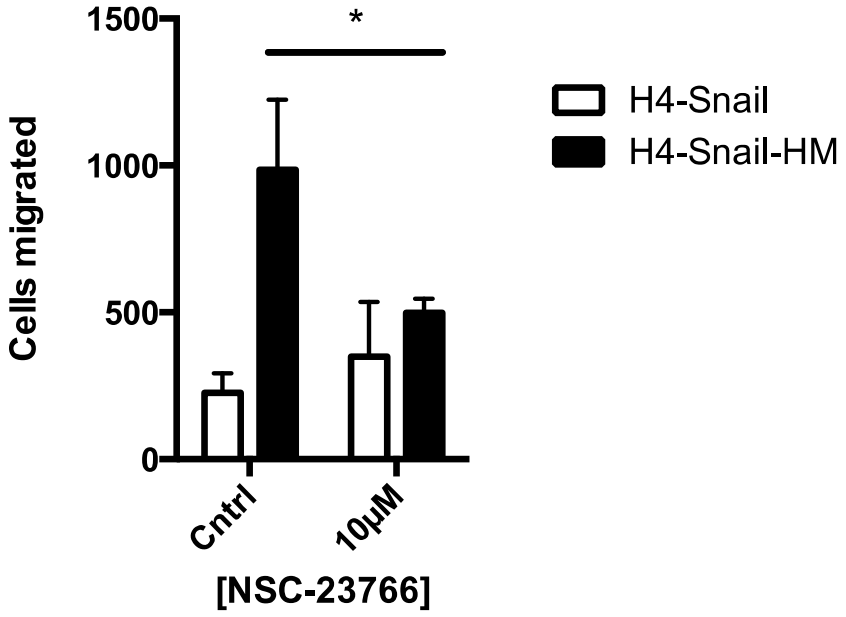

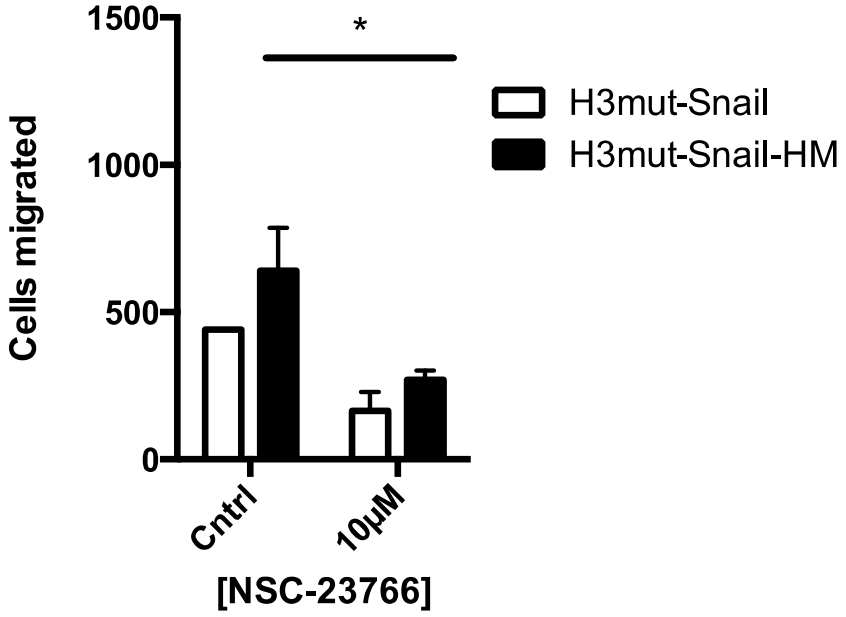

Figure 2.27: Heat maps of gene expression in *SNAI1* over-expressing HBECs. In the left panel, gene expression was normalized based on corresponding vector cell lines, and represents gene expression most influenced by *SNAI1* expression. The right panel represents ratios between highly migratory (HM) and corresponding parental *SNAI1* over-expressing HBECs, and represents gene expression most associated with high mobility.

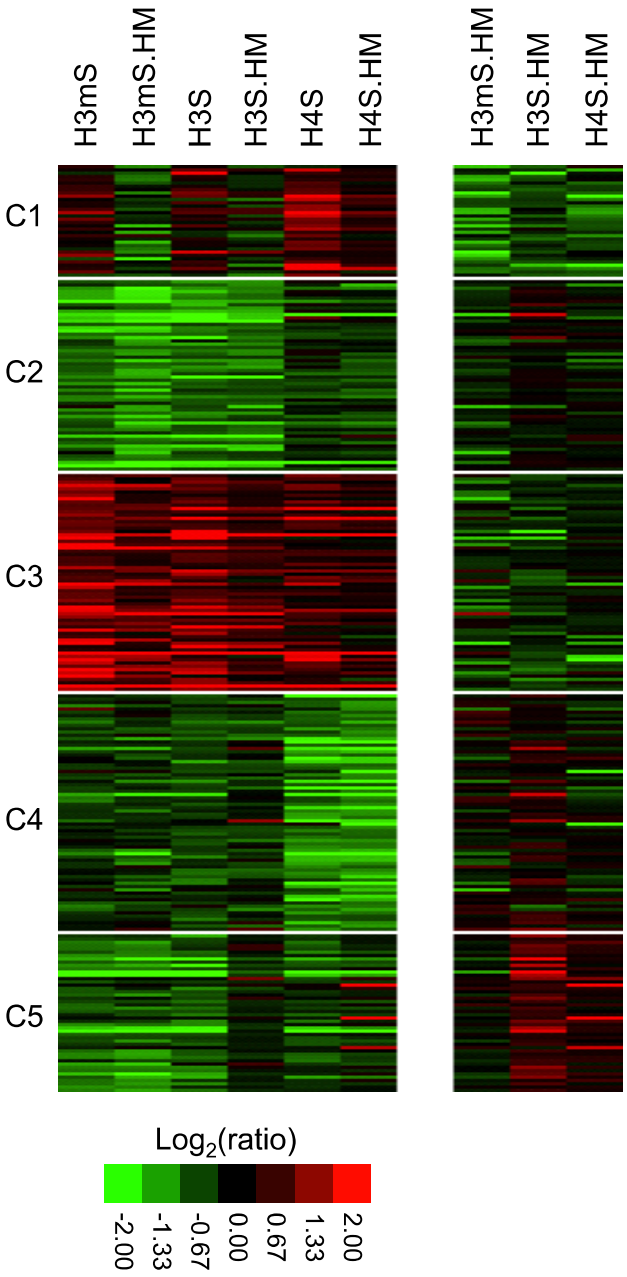

Figure 2.28: Gene set enrichment analysis reveals correlation between genes associated with high migration rates and poor survival in non-small cell lung cancer and breast cancer or melanoma recurrence. Enrichment plot of two gene sets significantly (FDR q-value < 0.01) associated with high mobility *SNAI1* HBECs as compared to non-selected parental cell lines.

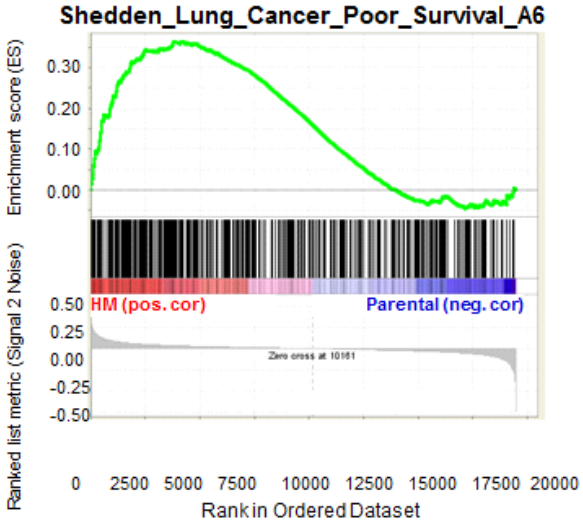

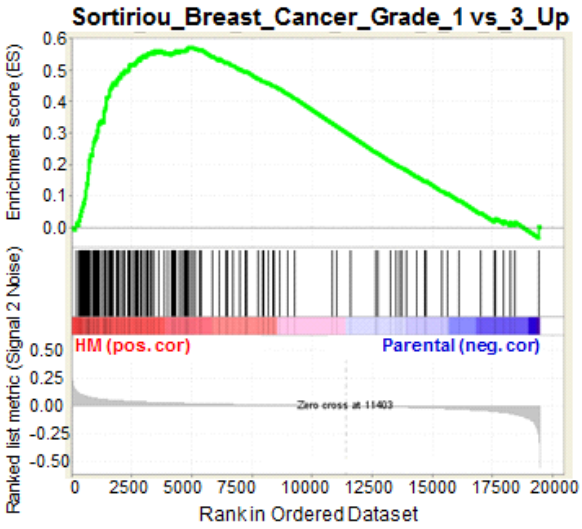

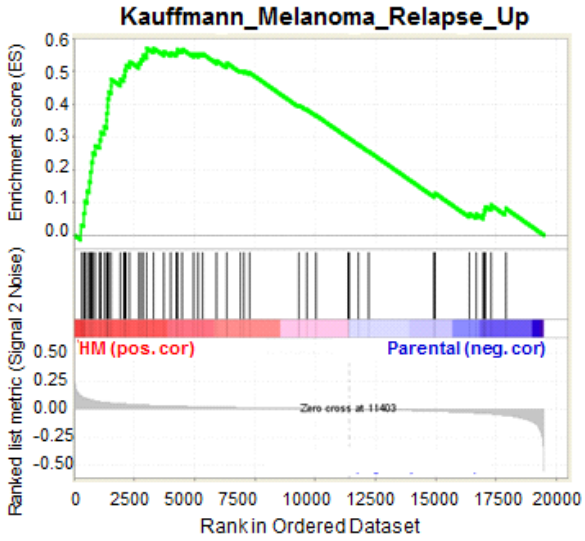

References

1. Sugimura H, Nichols FC, Yang P, Allen MS, Cassivi SD, Deschamps C, Williams BA, Pairolero PC. Survival after recurrent nonsmall-cell lung cancer after complete pulmonary resection. Ann Thorac Surg 2007;83(2):409-17; discussioin 17-8.

2. Tanaka F, Yoneda K, Kondo N, Hashimoto M, Takuwa T, Matsumoto S, Okumura Y, Rahman S, Tsubota N, et al. Circulating tumor cell as a diagnostic marker in primary lung cancer. Clin Cancer Res 2009;15(22):6980-6.

3. Okumura Y, Tanaka F, Yoneda K, Hashimoto M, Takuwa T, Kondo N, Hasegawa S. Circulating tumor cells in pulmonary venous blood of primary lung cancer patients. Ann Thorac Surg 2009;87(6):1669-75.

4. Mani SA, Guo W, Liao MJ, Eaton EN, Ayyanan A, Zhou AY, Brooks M, Reinhard F, Zhang CC, et al. The epithelial-mesenchymal transition generates cells with properties of stem cells. Cell 2008;133(4):704-15.

5. Rhim AD, Mirek ET, Aiello NM, Maitra A, Bailey JM, McAllister F, Reichert M, Beatty GL, Rustgi AK, et al. EMT and dissemination precede pancreatic tumor formation. Cell 2012;148(1-2):349-61.

6. Sanchez-Garcia I. The crossroads of oncogenesis and metastasis. N Engl J Med 2009;360(3):297-9.

7. Husemann Y, Geigl JB, Schubert F, Musiani P, Meyer M, Burghart E, Forni G, Eils R, Fehm T, et al. Systemic spread is an early step in breast cancer. Cancer Cell 2008;13(1):58-68.

8. Podsypanina K, Du YC, Jechlinger M, Beverly LJ, Hambardzumyan D, Varmus H. Seeding and propagation of untransformed mouse mammary cells in the lung. Science 2008;321(5897):1841-4.

9. Rausenberger J, Kollmann M. Quantifying origins of cell-to-cell variations in gene expression. Biophys J 2008;95(10):4523-8.

10. Liu YJ, Le Berre M, Lautenschlaeger F, Maiuri P, Callan-Jones A, Heuze M, Takaki T, Voituriez R, Piel M. Confinement and low adhesion induce fast amoeboid migration of slow mesenchymal cells. Cell 2015;160(4):659-72.

11. Ruprecht V, Wieser S, Callan-Jones A, Smutny M, Morita H, Sako K, Barone V, Ritsch-Marte M, Sixt M, et al. Cortical contractility triggers a stochastic switch to fast amoeboid cell motility. Cell 2015;160(4):673-85.

12. Welch MD. Cell migration, freshly squeezed. Cell 2015;160(4):581-2.

13. Cross SE, Jin YS, Tondre J, Wong R, Rao J, Gimzewski JK. AFM-based analysis of human metastatic cancer cells. Nanotechnology 2008;19(38):384003.

14. Xu W, Mezencev R, Kim B, Wang L, McDonald J, Sulchek T. Cell stiffness is a biomarker of the metastatic potential of ovarian cancer cells. PLoS One 2012;7(10):e46609.

15. Cross SE, Jin YS, Rao J, Gimzewski JK. Nanomechanical analysis of cells from cancer patients. Nature nanotechnology 2007;2(12):780-3.

16. Zhang W, Kai K, Choi DS, Iwamoto T, Nguyen YH, Wong H, Landis MD, Ueno NT, Chang J, et al. Microfluidics separation reveals the stem-cell-like deformability of tumor-initiating cells. Proc Natl Acad Sci U S A 2012;109(46):18707-12.

17. Windler-Hart SL, Chen KY, Chenn A. A cell behavior screen: identification, sorting, and enrichment of cells based on motility. BMC Cell Biol 2005;6(1):14.

18. Seo M, Lee WH, Suk K. Identification of novel cell migration-promoting genes by a functional genetic screen. FASEB J 2010;24(2):464-78.

19. Patsialou A, Wang Y, Lin J, Whitney K, Goswami S, Kenny PA, Condeelis JS. Selective gene-expression profiling of migratory tumor cells in vivo predicts clinical outcome in breast cancer patients. Breast cancer research : BCR 2012;14(5):R139.

20. Ramirez RD, Sheridan S, Girard L, Sato M, Kim Y, Pollack J, Peyton M, Zou Y, Kurie JM, et al. Immortalization of human bronchial epithelial cells in the absence of viral oncoproteins. Cancer Res 2004;64(24):9027-34.

21. Sato M, Larsen JE, Lee W, Sun H, Shames DS, Dalvi MP, Ramirez RD, Tang H, DiMaio JM, et al. Human lung epithelial cells progressed to malignancy through specific oncogenic manipulations. Mol Cancer Res 2013;11(6):638-50.

22. Kalluri R, Weinberg RA. The basics of epithelial-mesenchymal transition. J Clin Invest 2009;119(6):1420-8.

23. Yanagawa J, Walser TC, Zhu LX, Hong L, Fishbein MC, Mah V, Chia D, Goodglick L, Elashoff DA, et al. Snail promotes CXCR2 ligand-dependent tumor progression in non-small cell lung carcinoma. Clin Cancer Res 2009;15(22):6820-9.

24. Grant JL, Fishbein MC, Hong LS, Krysan K, Minna JD, Shay JW, Walser TC, Dubinett SM. A novel molecular pathway for Snail-dependent, SPARC-mediated invasion in non-small cell lung cancer pathogenesis. Cancer prevention research 2013.

25. Sato M, Vaughan MB, Girard L, Peyton M, Lee W, Shames DS, Ramirez RD, Sunaga N, Gazdar AF, et al. Multiple oncogenic changes (K-RAS(V12), p53 knockdown, mutant EGFRs, p16 bypass, telomerase) are not sufficient to confer a full malignant phenotype on human bronchial epithelial cells. Cancer Res 2006;66(4):2116-28.

26. Scherber C, Aranyosi AJ, Kulemann B, Thayer SP, Toner M, Iliopoulos O, Irimia D. Epithelial cell guidance by self-generated EGF gradients. Integrative biology : quantitative biosciences from nano to macro 2012;4(3):259-69.

27. Weiss L. Cancer cell traffic from the lungs to the liver: an example of metastatic inefficiency. Int J Cancer 1980;25(3):385-92.

28. Luzzi KJ, MacDonald IC, Schmidt EE, Kerkvliet N, Morris VL, Chambers AF, Groom AC. Multistep nature of metastatic inefficiency: dormancy of solitary cells

after successful extravasation and limited survival of early micrometastases. The American journal of pathology 1998;153(3):865-73.

29. Chambers AF, Naumov GN, Vantyghem SA, Tuck AB. Molecular biology of breast cancer metastasis. Clinical implications of experimental studies on metastatic inefficiency. Breast cancer research : BCR 2000;2(6):400-7.

30. Malek A, Catapano CV, Czubayko F, Aigner A. A sensitive polymerase chain reaction-based method for detection and quantification of metastasis in human xenograft mouse models. Clin Exp Metastasis 2010;27(4):261-71.

31. Schneider CA, Rasband WS, Eliceiri KW. NIH Image to ImageJ: 25 years of image analysis. Nat Methods 2012;9(7):671-5.

32. Gossett DR, Tse HT, Lee SA, Ying Y, Lindgren AG, Yang OO, Rao J, Clark AT, Di Carlo D. Hydrodynamic stretching of single cells for large population mechanical phenotyping. Proc Natl Acad Sci U S A 2012;109(20):7630-5.

33. Sit ST, Manser E. Rho GTPases and their role in organizing the actin cytoskeleton. J Cell Sci 2011;124(Pt 5):679-83.

34. Sotiriou C, Wirapati P, Loi S, Harris A, Fox S, Smeds J, Nordgren H, Farmer P, Praz V, et al. Gene expression profiling in breast cancer: understanding the molecular basis of histologic grade to improve prognosis. J Natl Cancer Inst 2006;98(4):262-72.

35. Kauffmann A, Rosselli F, Lazar V, Winnepenninckx V, Mansuet-Lupo A, Dessen P, van den Oord JJ, Spatz A, Sarasin A. High expression of DNA repair pathways is associated with metastasis in melanoma patients. Oncogene 2008;27(5):565-73.

36. Director's Challenge Consortium for the Molecular Classification of Lung A, Shedden K, Taylor JM, Enkemann SA, Tsao MS, Yeatman TJ, Gerald WL, Eschrich S, Jurisica I, et al. Gene expression-based survival prediction in lung adenocarcinoma: a multi-site, blinded validation study. Nat Med 2008;14(8):822-7.

37. Walser T, Yanagawa J, Luo J, Liu M, Goodglick L, Hong L-S, Fishbein M, Shay J, Minna J, et al. Abstract PR-11: Snail-induced and EMT-mediated early lung cancer development: Promotion of invasion and expansion of stem cell populations. Cancer prevention research 2008;1(7 Supplement):PR-11.

38. Tse HT, Gossett DR, Moon YS, Masaeli M, Sohsman M, Ying Y, Mislick K, Adams RP, Rao J, et al. Quantitative diagnosis of malignant pleural effusions by single-cell mechanophenotyping. Sci Transl Med 2013;5(212):212ra163.

39. Wirtz D, Konstantopoulos K, Searson PC. The physics of cancer: the role of physical interactions and mechanical forces in metastasis. Nat Rev Cancer 2011;11(7):512-22.

40. Radisky DC, Levy DD, Littlepage LE, Liu H, Nelson CM, Fata JE, Leake D, Godden EL, Albertson DG, et al. Rac1b and reactive oxygen species mediate MMP-3-induced EMT and genomic instability. Nature 2005;436(7047):123-7.

41. Dirat B, Ader I, Golzio M, Massa F, Mettouchi A, Laurent K, Larbret F, Malavaud B, Cormont M, et al. Inhibition of the GTPase Rac1 Mediates the Antimigratory Effects of Metformin in Prostate Cancer Cells. Molecular cancer therapeutics 2014.

42. Reymond N, d'Agua BB, Ridley AJ. Crossing the endothelial barrier during metastasis. Nat Rev Cancer 2013;13(12):858-70.

43. Yokota J. Tumor progression and metastasis. Carcinogenesis 2000;21(3):497-503.

44. Sidani M, Wyckoff J, Xue C, Segall JE, Condeelis J. Probing the microenvironment of mammary tumors using multiphoton microscopy. Journal of mammary gland biology and neoplasia 2006;11(2):151-63.

45. Meijering E, Dzyubachyk O, Smal I. Methods for cell and particle tracking. Methods in enzymology 2012;504:183-200.

46. Arsic N, Bendris N, Peter M, Begon-Pescia C, Rebouissou C, Gadea G, Bouquier N, Bibeau F, Lemmers B, et al. A novel function for Cyclin A2: control of cell invasion via RhoA signaling. J Cell Biol 2012;196(1):147-62.

47. Sollier E, Murray C, Maoddi P, Di Carlo D. Rapid prototyping polymers for microfluidic devices and high pressure injections. Lab on a chip 2011;11(22):3752-65.

48. Sharma S, Santiskulvong C, Bentolila LA, Rao J, Dorigo O, Gimzewski JK. Correlative nanomechanical profiling with super-resolution F-actin imaging reveals novel insights into mechanisms of cisplatin resistance in ovarian cancer cells. Nanomedicine : nanotechnology, biology, and medicine 2012;8(5):757-66.

CHAPTER THREE: Phenotypic and molecular properties of micropore-selected highly migratory cells

Introduction

A prerequisite to study the object of rare biological phenomena (for example, a circulating tumor cell in the context of cancer metastasis) can be the study of that object in isolation, which is required in order to eliminate confounding contributions from unwanted players within that system. The selection of highly migratory cells from an otherwise non-migratory population allows us to focus on this behavior in isolation at the phenotypic and molecular levels, and to be confident that what we are analyzing is an enriched trait. Herein, we describe various cell-biological traits associated with the highly migratory phenotype in human bronchial epithelial cells, as well as the results of genetic and molecular screens in these cells. Connections to other's findings described in the literature are made based on multiple independent observations that provide worthwhile paths for further research. The work described in this final chapter opens the study of enhanced epithelial cell motility and metastatic behavior to a variety of directions that may prove fruitful.

Results

Heterogeneity in motility observed amongst premalignant lung epithelial cells

Much of the work described in this dissertation was originated from a variety of observations in cell motility. First, we observed that the motile response to external stimuli (TGFβ treatment) in NSCLC cells was different at the single-cell level. Individual H358 adenocarcinoma cells within the population either remained stationary or commenced movement (**Figure 3.1, Video 3.1**). Second, when comparing motility in a scratch assay using NSCLC and HBEC lines, we noticed: a) gap closure occurred in the

HBECs in a third of the time and b) NSCLC cells move with collective cell motility (a cohesive sheet of cells moving as one) whereas HBECs move independently from one another (**Figure 3.2, Video 3.2**). Importantly, within the HBEC population, there seemed to be vast heterogeneity in motility: cells that were multiple “rows” back had the desire to move to the leading edge, while others were content to remain stationary or move back into the jammed cell space (**Figure 3.3, Video 3.3**). Third, we found that mutations typically found in premalignant lesions resulted in enhanced 2-dimensional motility (**Figure 3.4**). While our observation of the highly motile and invasive capacity of epithelial cells relative to tumor cells may appear counterintuitive, these findings are actually consistent with those in the recent literature that document the profoundly motile capacity of epithelial cells (1-3). Overall, there appeared to be a heterogeneous capacity for movement in our model of early stage disease that was not apparent in NSCLC cell lines, which caused us to focus on migration and metastasis in our premalignant HBEC model.

Identification of highly migratory cells in the parental HBEC population based on morphology

A question we had asked was whether or not the highly migratory phenotype was one that existed in the general population, or what that had arisen *de novo* as a result of migration through constrictive space. One could imagine irreversible DNA damage to migrating cells that could lead to advantageous migration if a susceptible gene was perturbed. Because of the unique morphology described in H4-Snail-HM cells in chapter two, we decided to look for these cells in the unselected “parental” population.

Unselected H4-Snail cells were seeded in 6-well plates and incubated for 48 hours. Cells were fixed and stained with Hoechst, and multiple fields were scanned using an automated microscope. We then manually searched each field for a cell with the “highly migratory” morphology, which is a cell containing multiple protrusions. Hoechst staining allowed us to quantify all cells analyzed in order to quantify the abundance of the highly migratory subpopulation. Of 25 adjacent fields containing nearly 900 cells, only one cell representing the highly migratory phenotype was identified (**Figure 3.5**). This suggests that the highly migratory phenotype existed prior to selection at relatively low abundance (approximately 0.1% of the parental population), and that selection did not cause enhanced migration. Additional experiments that would support this claim would be the identification of molecular markers that identify the highly migratory phenotype in order to provide an alternative method for isolation (immunomagnetic isolation or fluorescence activated cell sorting based on a surface antigen, for example).

Down-regulation of cell adhesion molecules in highly migratory cells is Snail-related

Because EMT is known to drive migration in epithelial cells (4), we wanted to determine if up-regulation of mesenchymal markers could be the cause for enhanced migration. Microarray data and western blot for various EMT markers showed no apparent change in transcript or protein levels in H3mut-Snail-HM/H3mut-Vector-HM cells. However, N-cadherin levels (*CDH2*) were substantially decreased in all the highly migratory Snail cell lines (**Figure 3.6 and Figure 3.7**). N-cadherin is a calcium-dependent homotypic cell adhesion molecule. The extracellular domain interacts with N-cadherin on other cell membranes, and the intracellular domain is coupled to the actin

cytoskeleton via catenin linkers. To test the influence of N-cadherin on motility, we measured the velocity cells at low density (25 cells/mm^2) and high density (confluent monolayer scratch assay). Theoretically, cells should move slower when more N-cadherin-mediated cell-to-cell contacts are established (high density), and faster in the absence of N-cadherin-mediated contacts. In this instance, H3mut-Snail-HM cells moved at the same velocity as unselected lines when plated at low density, where N-cadherin adhesions are minimized. However, at high density the H3mut-Snail-HM cells moved with 27% greater velocity (**Figure 3.8, Video 3.4**). This suggests, at least in 2-dimensional motility, that the highly motile phenotype is related to the absence of N-cadherin. Additional studies to verify this phenomenon, such as calcium depletion or genetic reversal of *CDH2*, are required.

Focal adhesion-associated proteins are involved in cell adhesion to the extracellular environment. They can nucleate around the intracellular domain of integrins and allow for the association with the actin cytoskeleton. Focal adhesions can be composed of hundreds of different proteins and cell migration requires their regulated, dynamic assembly/disassembly cycle to be spatially and temporally coupled to lamellipodium formation (5). Nascent adhesions (<0.25 μm diameter) form as the cell body protrudes forward, and as migration continues some disassemble and others mature into focal complexes (~0.5 μm diameter) and further to focal adhesions (1-5 μm diameter). This increase in size corresponds to increased tensional strength. These adhesions are transient, lasting between 1 and 5 minutes). At this point, focal adhesions can disassemble or further mature into fibrillar adhesions (> 5 μm diameter), which no longer promote cell migration (6). Because of their critical relationship with motility, we

decided to look at focal adhesions in highly migratory cells. We chose to look at phospho-paxillin (pPXN) as it is present in focal complexes and adhesions, as well as fibrillar adhesions. We found a Snail-dependent reduction in both the number and size of adhesions containing pPXN (**Figure 3.9**). The reduction in size of the focal adhesions in highly migratory cells suggests rapid turnover, which is typical of cells on the move.

Nuclear lamina composition and the highly migratory phenotype

Our studies involving N-cadherin and pPXN have been in 2-dimensional non-constrictive space, and while they provide important information about the functionality of these molecules in the context of cell-cell interaction and motility, 2-dimensional space is rarely (if ever) encountered by a cell *in situ*. Others have shown that nuclear lamin composition dictates migration through constrictive space in 3-dimensions, which may have implications in metastatic ability and cell survival (7-9). We examined nuclear lamin composition by western blotting for four main lamin isoforms: lamin A, B1, B2, and C. Our results show that lamin A levels are increased and lamin B1 levels are decreased in highly migratory cells, while lamin B2 and C are unchanged (**Figure 3.10**). These results are consistent with literature reports that the lamin A:B ratio is increased in cells with greater rates of migration.

RNA analysis, Luminex assay, and cytoskeleton phosphoprotein arrays identify unique genetic and molecular attributes in highly migratory cells

We have isolated a previously unidentified subpopulation of highly migratory cells, of which very little is known about the global genetic and molecular make-up. mRNA microarray data presented in chapter two show the majority of deregulated

genes in highly migratory cells are in fact down-regulated. There are multiple mechanisms by which genes can be down-regulated, including transcriptional repressors, DNA and histone methylation, and micro-RNA (miRNA). Because so many genes were down-regulated, and because we had mRNA data for comparison, we decided to look at miRNA. Total RNA was isolated from unselected and highly migratory cell lines and library preparation was performed by performing size fractionation followed by adapter ligation. We found the majority of deregulated miRNAs were also down-regulated (**Figure 3.11**), suggesting that cause of mRNA down-regulation might be occurring by different mechanisms (for example, histone or DNA methylation). To add to this, principle component analysis of transcript data shows that Snail expression is a predominant factor related to changes in the gene expression profile amongst the cell lines tested, and the difference in gene expression between high and low migratory cells is quite small (**Figure 3.12**). These results suggest that cells may only require slight changes at the RNA level for enhanced migration. This idea is echoed in recent opinions that different migration modes can arise in very similar cell types, probably based on subtle molecular differences (10,11).

Secreted factors, such as cytokines and chemokines, are well described drivers of motility and migration. One driver of the motile phenotype could be differentially secreted cytokines. In order to determine differences in cytokine/chemokine secretion in high versus low migratory cells we collected supernatants and cell lysates from highly migratory and parental cell lines and ran these on a multi-plex Luminex bead array. This technology works by using antibodies to a cytokine conjugated to a bead containing quantum dots of a particular color. Different antibody-quantum dot combinations allows

you to screen a variety of targets simultaneously using a single color for excitation (quantum dots absorb at the same wavelength, but emit light at different wavelengths depending on their size/structure). Bead mixtures are incubated with lysate, washed, and incubated with a biotinylated antibody to the same target. Streptavidin-PE (SAPE) is then added such that both beads and protein concentration (SAPE intensity) can be simultaneously measured. Results show unique cytokine profiles for each highly migratory cell with some areas of overlap (**Figure 3.13**). Reports in literature have shown that GROα (CXCL1) affects anchorage independent cell growth (AIG) (12), and GROα secretion is down-regulated in Snail-HM cells. To test this hypothesis, we plated H3mut-Snail and H3mut-Snail-HM cells in an AIG assay. We found that highly migratory Snail-cells produced noticeably fewer and smaller colonies (**Figure 3.14**). This corroborates descriptions in the literature of a "grow-versus-go" phenotype, where cells are said to either divide or invade (13,14). To verify this occurs in our system, we took the AIG assay one step further. Established colonies were stained with Hoechst and we performed time-lapse fluorescent microscopy. The colonies produced by H3mut-Snail cells were large and had very little cellular movement. However, while colonies produced by H3mut-Snail-HM cells were smaller, the cells within the colony moved rapidly (**Figure 3.15, Video 3.5**).

While gene expression data can provide important information about the transcriptional program of the cell, the motility program is largely regulated at the post-translational level through protein modification, mainly phosphorylation. To determine the state of a variety of cytoskeleton-related proteins simultaneously, we utilized a cytoskeleton phospho-protein antibody array, which contains multiple antibodies against

various proteins and their phosphorylated counterparts (15). While the abundance and phosphorylation states of the proteins on the array varied amongst the cell lines tested (**Figure 3.16**), there were some commonalities. For example, cortactin levels did not change in the datasets, but phospho-cortactin levels (Y421 and Y466) were increased in both cell lines (**Table 3.1**). Recent work from the Condeelis group has shown that phosphorylation of cortactin is required for invasion, and that expression of a dominant negative mutant cortactin (lacking tyrosine phosphorylation sites) exhibited severe defects in migration (16,17). Cortactin is phosphorylated in a Rac1-GTP dependent manner by PKN2. We have shown increased levels of Rac1-GTP in some highly migratory cells (**Figure 3.17**) and that these cells lose migratory capacity upon Rac1 pathway inhibition. Together, these data support a Rac1 pathway activation-mediated enhanced migration.

Inhibitors to RhoA/Rac1 pathway components show various effects on migration

Rac1-GTP is elevated in highly migratory cells, and we wanted to determine if inhibition of Rac1 could attenuate migration. We decided to test a variety of inhibitors at different points in the pathway due to the “high-throughput” nature of a 96-well migration assay (**Table 3.2**). Prior to performing the assay, we carried out a proliferation assay to determine the optimum concentration of inhibitor that would hit the target but would minimize anti-proliferative or otherwise cytotoxic effects (**Figure 3.18**). Inhibiting RhoA activation by Rhosin, which targets a RhoA GEF, showed an increase in migration rate at low concentrations. Inhibition of the RhoA effector myosin light chain kinase by ML-7 showed little effect on migration. However, inhibition of ROCK, another RhoA effector,

showed a slight increase in migration at low concentrations (**Figure 3.19**). Because RhoA activity is known to perturb Rac1 activity, these results support the conclusion that high rates of migration are obtained as a result of Rac1-pathway activation.

Discussion and Future Directions

While each of the studies described in this chapter admittedly does not investigate any one particular mechanism at substantial depth, its purpose was twofold: first, it was part of the intense characterization of the subpopulation of highly migratory cells which show unique metastatic properties in an otherwise non-metastatic line, and second, it provides a launching pad for future exploration.

Our early observation that premalignant cells move faster and with greater persistence than lung cancer cell lines was truly a fascinating discovery. Up until this point, the majority of the field believed that cell motility related to metastasis mainly occurred in large, established tumors. However, this motile capacity is consistent with the movement characteristics of epithelial cells in embryonic development and wound closure. In a teleological view, these profound capacities endowed by the genetic programs of EMT are inherent in embryonic development and wound closure (18), which are requisite phenotypes whose evolutionary histories apparently far exceed that of malignancy. While an interesting question to answer would be why HBECs move faster than NSCLC cell lines, the greatest obstacle in studying this phenomenon is the fact that we know very little about the genetic landscape of cancer cell lines. Now that more information is known about the molecular makeup of highly migratory HBECs, we can apply this newfound knowledge to make meaningful comparisons in the context of

malignancy. Our lab has access to HBEC and cancer cells from the same patient. Isolating highly migratory cells from each of these populations may give us a better understanding of how the motility program progresses by making observations concerning early and late stage disease in the same patient background.

The idea that cell adhesion molecules, including N-cadherin, are down-regulated in all highly migratory Snail cells strongly suggests the importance of this molecule in regulating motility. With the exception that adhesion might prevent a cell from moving at full capacity because it is anchored down by other cells, at this point we do not fully understand the implications of N-cadherin loss and enhanced migration. While it is true that it is difficult do “treat” patients due to loss of function abnormalities, N-cadherin also acts to regulate Wnt and Akt signaling. N-cadherin sequesters β-catenin to the cell membrane, a molecule canonically involved in activation of TCF/LEF transcription factors. N-cadherin also binds LRP5/6 on the cell surface, and prevents interaction with the FZD receptor and Wnt ligands (19-21). Many of the players in these pathways are currently under clinical investigation for inhibiting tumor growth and could perhaps be investigated pre-clinically in our highly migratory model system to prevent metastasis. Analyzing β-catenin levels and sub-cellular localization or using a reporter system such as the TOPflash/FOPflash assay, which indicates TCF/LEF activity, would be important first steps in determining the mechanism of *CDH2*-mediated enhanced migration.

Another cytoskeleton-related molecule, cortactin, was found to have increased phosphorylation in our highly migratory cells. Besides having an extensive literature following (15-17), the cortactin gene is amplified in many cancer types, is up-regulated

in over 15% of squamous lung cancers, and results in decreased disease free survival in patients with this disease, according to The Cancer Genome Atlas (TCGA) data (**Figure 3.20**) (22). Cortactin is phosphorylated in an activated Rac1-dependent manner; however, it is unknown whether the constitutively active Rac1 splice variant, Rac1b (23,24), can also lead to cortactin phosphorylation. Our microarray data show that *ESRP1* (epithelial splicing regulatory protein 1) is decreased in highly migratory cells, and recently others have shown that decreased *ESRP1* results in elevated Rac1b levels (25). This suggests a Rac1 – ESRP1 – Cortactin regulatory axis may be important for enhanced migration, although more work needs to be performed.

Nuclear lamins have been shown to play a critical role in cell migration (7,8). Our studies show that selected highly migratory cells have an increase in the lamin A:B ratio (**Figure 3.10**), which others have shown is critical for survival following movement through constrictive space (9). We have also demonstrated that post-migration viability is compromised in cells that have not undergone micropore selection. While my data is suggestive of a lamin-based survival method in highly migratory cells, further experiments will need to be performed to verify this is valid, including genetically manipulating the amounts of lamin expression in highly migratory and unselected cells. More importantly, determining the mechanisms that regulate lamin expression/maintenance in highly migratory cells might allow for therapeutic intervention. It is known that lamin phosphorylation occurs prior to nuclear envelope breakdown during mitosis and protein kinase C (PKC) has been implicated in this process as a mediator of lamin disassembly and reduction (26-29). In unrelated studies, PKC signaling in the context of apoptosis resistance has been found to be a

distinguishing feature of high versus low metastatic cells (30). These four true facts (highly migratory cells have increased Lamin A:B ratio, lamins are regulated in mitosis via PKC signaling, PKC signaling is critical in shear-stress related apoptosis resistance during metastasis, and enhanced metastatic survival as a result of migration selection) make a compelling case for further exploration. Not much is known about post-translational modification of lamins and its relationship to enhanced migration and metastatic efficiency; however, utilizing the highly migratory model system and investigating PKC pathway activation may provide the missing links.

The study of motility in NSCLC and HBECs detailed in this dissertation yields a profound observation that few in the field appreciate: non-transformed cells move faster than cancer cells. This has implications for how we view lung cancer progression in the earliest stages of disease pathogenesis. Sanchez-Garcia theorized in the *New England Journal of Medicine* that cells within pre-malignant lesions have the capacity to "metastasize" prior to and concomitant with tumor formation (31), a process dubbed the parallel-progression model for lung cancer (**Figure 3.21**). If these cells indeed have the capacity to move in a premalignant state *in situ*, as our work in support of this theory suggest, then efforts to thwart movement must be a top priority, lest these cells spread the impending malignancy.

Materials and Methods

Cytokine Treatment and NSCLC Cell Motility

H358 lung adenocarcinoma cells were cultured according to standard methods. Cells were harvested, counted, and plated in 24-well plates at 10^4 cells/well. The next day, we replaced medium with that containing 15 ng/mL TGFβ or BSA (control). Cells were incubated 48 hours prior to imaging. Images were taken at 20 minute intervals for 24 hours on a temperature, humidity, and CO_2 controlled stage. 9 adjacent fields were imaged on a Nikon Eclipse Ti inverted microscope at 100x total magnification (Nikon 10x PlanFluor, 0.30 NA). Images were taken with a Cascade II EM-CCD (Photometrics, Tucson, AZ) at a 30 ms exposure with maximum gain, controlled by Nikon Elements AR software.

Selection of Non-migratory cell population

Cells were plated in 6-well transwells as described in chapter 2 (8 μm pore only), except using 100,000 cells per well. Cells were allowed to migrate for 5 days, with media changes each day. In addition, the bottoms of the transwells were swabbed with a cotton swab each day to prevent migraotry cells from moving back to the upper chamber. On the fifth day, cells were washed in PBS, and harvested using trypsin as described earlier. Cells underwent 5 rounds of selection and are denoted “NM” for non-migratory.

Scratch Assay

Cells were plated at high density (70% confluence) in a 12-well plate and incubated in complete medium until confluent. A scratch was made using a p10 pipette tip in three locations across the well, followed by three rinses in complete medium to remove floating cells. Cells were imaged as described above, except using 10 minute intervals for 8-12 hours. For velocity analysis image series were imported into ImageJ and the change in position of each cell was tracked through successive frames using the Manual Track plugin, which utilizes an XY-mapping system. Using the distance formula, the lengths each cell traveled between frames could be calculated. Dividing by time yields velocity, which is expressed in microns per minute.

Phenotypic identification of highly migratory cells in parental background

H4-Snail cells were harvested and plated in 6-well plates at low density (~75 cells/mm^2) and incubated for 24 hours. Prior to imaging, cells were fixed and stained with Hoechst as described before. 25 adjacent fields were imaged with 10% overlap (stitching) using a Nikon inverted microscope with electromechanical X,Y,Z-stage and 10x objective, controlled by Nikon Elements AR software. Both phase contrast and fluorescent techniques were utilized, as described previously. Stitched images were manually scanned qualitatively for cells that expressed the highly migratory phenotype (cells with extensive protrusions). To determine the total cell number, fluorescent images were converted to binary in ImageJ, and quantified using the “analyze particle” function.

Microarray and miRNA Sequencing

HBECs were cultured in 10 cm dishes for 3 days, or until 70-80% confluent. Lysates were harvested using 700 µL Qiazole (Qiagen) and RNA extracted according to

manufacturer's protocol. RNA was purified using miRNeasy kit (Qiagen). Total RNA was provided to the UCLA Clinical Microarray Core, where library preparation and sequencing was performed on an Illumina system. Gene expression was investigated by Affymetrix GeneChip HTA 2.0 Array at the UCLA Clinical Microarray Core. Normalization at gene-based level was done by Affymetrix Expression Console using RMA approach. Non-annotated transcripts were then filtered out from the data before further analysis. Bioconductor *limma* package was used for gene expression analysis. A gene was defined as being differentially expressed by two conditions, (1) its fold change was greater than 1.5 and (2) two-tail t-test p-value was less than 0.1. Cluster 3.0 was used for clustering analysis.

EMT marker and nuclear lamin analysis

Cells grown to 80% confluence in T25 flasks were washed with ice-cold PBS and lysed with RIPA buffer using standard methods. Twenty µg of each cell lysate was loaded per lane, and proteins were resolved by SDS-PAGE and transferred to an Immobilon-P Transfer Membrane (Millipore, Billerica, MA). The membranes were blocked with 5% milk and then incubated with primary antibodies diluted in blocking solution according to the manufacturer's recommendations. Horseradish peroxidase-conjugated secondary antibodies (Bio-Rad, Hercules, CA) and enhanced chemiluminescence (ECL) reagent (Amersham Biosciences, Piscataway, NJ) were used for protein detection. Primary antibodies were from the following sources: TUBULIN, SNAIL, LAMIN A/C, LAMIN B2 (Cell Signaling Technologies, Danvers, MA); N-CADHERIN (Becton Dickenson,

Milpitas, CA); LAMIN B1 (AbCam, Cambridge, MA). Densitometry performed in ImageJ using the “Analyze Gels” function

Paxillin Immunofluorescence

Cells were grown on uncoated 12 mm glass cloverslips (Electron Microscopy Sciences, Hatfield, PA) in complete medium. Cells were fixed and permeabilized using freshly diluted 4% PFA (10% stock solution, Electron Microscopy Sciences) and 0.1% Triton X-100 using standard methods. Cells were blocked for 30 minutes in 1% BSA. Cells were labeled in blocking buffer with 1:100 rabbit anti-phospho-paxillin (Cell Signaling, Danvers, MA) overnight at 4°C, followed by 3x5 minute 0.5% Tween-20/PBS washes. Cells were stained for 30 minutes at room temperature in secondary antibody (goat anti-rabbit Alexafluor488, Life Technologies), then washed in 0.5% Tween-20/PBS. Cells were stained with phalloidin-AlexaFluor647 (Life Technologies) and counterstained with DAPI according to the manufacturer’s instructions. ProLong Gold (Life Technologies) was used to mount the coverslips. Cells were imaged at room temperature using a Nikon Eclipse 90i upright fluorescent microscope and 10x or 20x objective (Nikon 10x PlanFluor DIC L/N1, 0.30 NA; Nikon 20x Plan Apo VC DIC N2, 0.75 NA). Images were captured using a Nikon Digital Sight DS-Qi1Mc camera at 1024x1024 or 1280x1024 pixel resolution. To quantify focal adhesions, individual cells within each image were thresholded using ImageJ. The “analyze particles” function was used to determine the number and size distribution of focal adhesions. At least 60 cells of each type were analyzed for nuclear size.

Luminex Assay

Cells were plated in 6-well plates and grown for 3 days, or until 75% confluent. Supernatants were collected and centrifuged for 5 minutes at 1000 x g, then transferred to a new tube and frozen at -80°C. Cells were rinsed twice in ice-cold PBS and lysates were collected as previously described and a BCA assay was performed to determine protein concentration. Luminex assay was performed according to manufacturer's specification using human Group I and II cytokines kit (Bio-rad, Hercules, CA). Data was normalized to lysate concentration.

Anchorage independent cell growth assay

Cells were harvested and suspended in 500 µL complete medium and placed in a 37°C water bath. 500µL 2x DMEM was then mixed the cell suspension, followed by addition of 500 µL 1.6% 55°C molten agar, and 100 µL was quickly added on top of an existing 0.6% agar bed in a 96-well plate. Once the agar solidified, 100 µL complete medium was added to each well. Cells were imaged that day (time 0) and monitored for 4 weeks (medium exchange every 5 days). Wells were imaged using an inverted microscope with automated X, Y, and Z-stage at 100x total magnification. Z-stacks were acquired at 25 µm step intervals for the height of the cell-layer, and focused images were prepared using the "extended depth of focus" function in Nikon Elements AR software. Colonies were counted manually. For fluorescent studies, colonies grown in agar were labeled with 10 µg/mL Hoechst-33324 for 3 hours at 37°C. Three 30 minute washes were performed using complete medium at 37°C. Cells were imaged at 20x magnification on the Nikon Ti inverted microscope as described previously for 10 hours at 5 minute intervals.

Cytoskeleton phospho-protein array

Cytoskeleton phospho-protein arrays were purchased from Full Moon Biosystems (Sunnyvale, CA) and lysates prepared according to protocol. Briefly, lysates were collected on ice in lysis buffer containing phosphatase inhibitor cocktail (Sigma Aldrich, St. Lois, MO) and clarified by centrifugation. Buffer exchange into “labeling buffer” was performed using ion exchange chromatography in a microcentrifuge tube format, followed by BCA assay to determine concentration. Protein lysate was then biotinylated and added to the pre-blocked array chip (microscope slide format) and incubated for 2 hours, followed by extensive wash steps. Detection reagent (Cy3-streptavidin solution) was incubated on the slides for 20 minutes, followed by more washing. Slides were dried then imaged using GenePix 4100 automated microarray scanner (Molecular Devices, Sunnyvale, CA) and analysis performed using GenePix software. Normalization was performed using on-chip β-actin or GAPDH control spots.

Rho-family GTPase activation assay

RhoA, Rac1 and Cdc42 GTPases were quantified using G-LISA kits (Cytoskeleton Inc, Denver, CO). Lysates were collected in GTPase specific lysate buffer and snap frozen in liquid nitrogen and subsequently stored at -80°C until needed. Concentration was determined by BCA assay. Lysates were rapidly thawed in a room-temperature water bath and equilibrated with lysate buffer so all concentrations were equal. GLISA was performed according to manufacturer protocol.

Proliferation Assay

1500 H3mut-Snail cells per well were added to four replicate white-wall/bottom 96-well plates in 100 µL volume and incubated at 37°C. The next day (time 0) and at 24, 48 and 72 hours, 100 µL of ATPlite solution was added to each well according to manufacturer's recommendations (Perkin Elmer, Waltham, MA) and luminescence was read by a plate reader. The ATPlite readout is of ATP levels in the cell, which directly correlates to cell number.

Migration assay with inhibitors

10,000 cells per well were seeded in 96-well transwells (Corning Inc, Corning, NY). After overnight attachment, media in the top and bottom compartments was decanted and replaced with medium containing inhibitor of various concentrations. ML-7 (myosin light chain kinase inhibitor), Y-27632 (Rho associated kinase/ROCK inhibitor), and NSC-23766 (Rac1-GEF inhibitor) were all from Caymen Chemical (Ann Arbor, MI). Rhosin (RhoA-GEF inhibitor) was purchased from EMD Millipore (Billerica, MA). After additional 24 hour incubation in the presence of inhibitor, the tops of the transwells were swabbed, and cells were fixed, stained and imaged as described earlier (Hoechst). Values were normalized to plating density from a separate 96-well plate fixed following overnight attachment.

Cortactin Analysis using TCGA Data

cBioportal for Cancer Genomics is developed and maintained by the Center for Molecular Oncology and the Computational Biology Center at Memorial Sloan-Kettering Cancer Institute (32,33). The cortactin gene (*CTTN*) was queried in "All Datasets" or the "Lung Squamous Cell Carcinoma – TCGA Provisional" dataset using default

parameters. Cross-cancer alteration summary and survival data was exported in vector format using endogenous cBioportal export functions.

Statistical Analysis

Samples were plated and run in triplicate, unless otherwise indicated, and all experiments were performed at least three times. Statistical analyses were performed on all data sets, and results from one representative experiment or image are shown. All statistical analyses were performed in Prism 6 (GraphPad, La Jolla, CA) unless noted. All results are reported as mean ± SEM, unless indicated. The statistical significance of these data was determined using an unpaired, parametric *t*-test with 95% confidence interval. The statistical significance of the viability data set was determined using the Mann-Whitney test (two-tailed, 95% confidence interval). Data were reported significant as follows: * if $p \leq 0.05$, ** if $p \leq 0.01$, and *** if $p \leq 0.001$.

Acknowledgments

The authors wish to acknowledge the UCLA Genotyping/Sequencing Core for miRNA sequencing and microarray services. We would like to thank the CTSI, as well as the UCLA California Nanosystems Institute Advanced Light Microscopy/Spectroscopy Cores for microscopy resources.

Figures and Tables

Figure 3.1: Differential response to cytokine treatment in NSCLC cell line. Most H358 adenocarcinoma cells exposed to TGFβ remain stationary. However, in some cells and induced-motility response occurs. Green line indicates the movement of a cell over the course of the study. 100x total magnification.

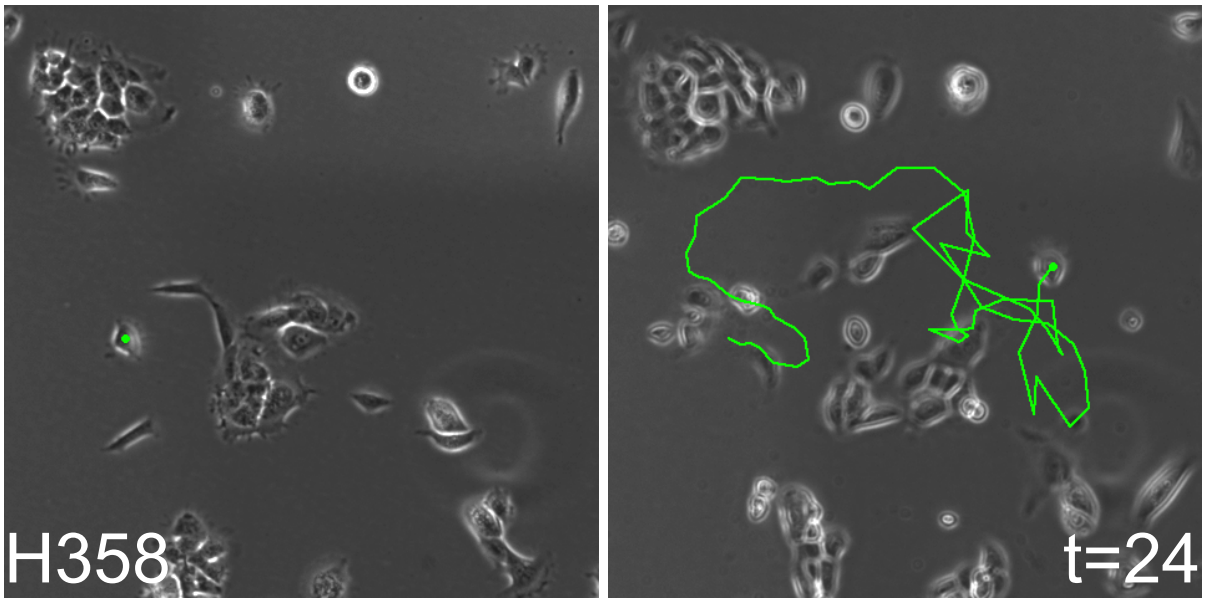

Figure 3.2: Premalignant cells move faster than fully-malignant NSCLC cells. In a scratch assay, A549 cells move slowly and as a collective sheet of cells in which cell-cell contacts are maintained. HBECs, on the other hand, move irrespective of surrounding cells and at higher speeds. 100x total magnification.

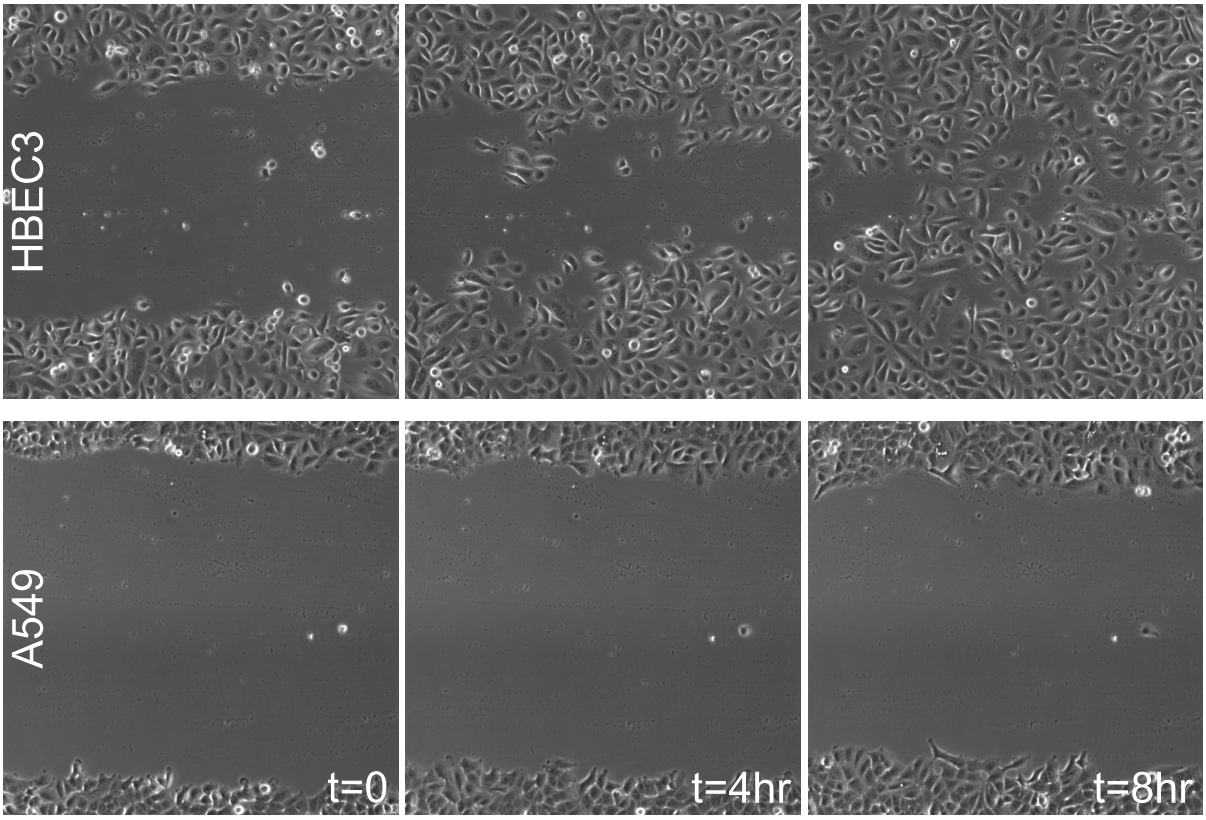

Figure 3.3: Heterogeneity in motile behavior is apparent in HBECs. In a typical scratch assay, cells at the leading edge are the first to enter the scratched area. However, HBECs multiple “rows” back push their way to the front (magenta mark), whereas a cell in the front gradually retreats (yellow mark). 8 hours between time points shown.

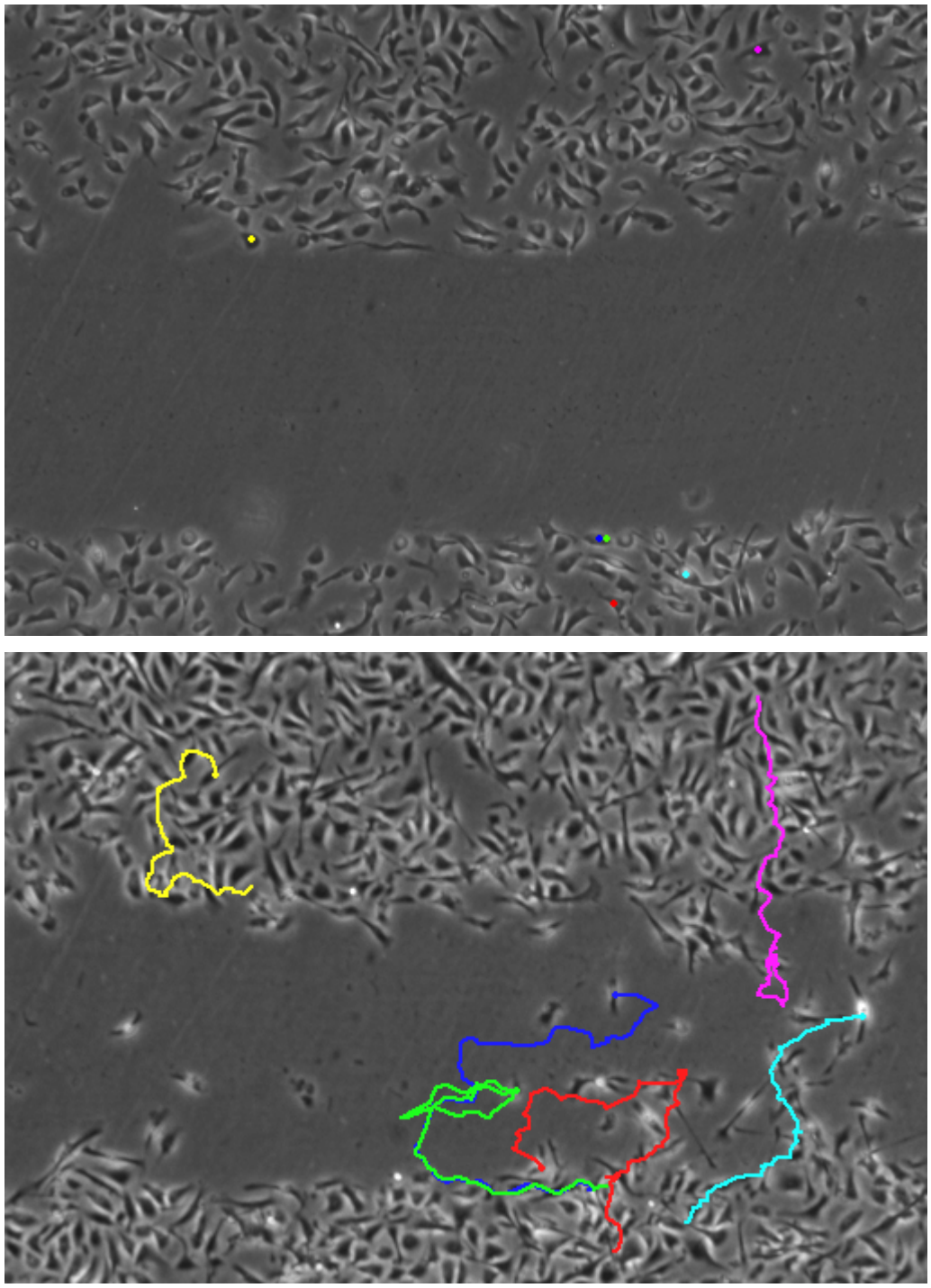

Figure 3.4: Oncogenic mutations found in premalignancy and NSCLC increase cell speed. Expression of p53 shRNA and KRAS^{V12D} enhances HBEC movement on tissue culture plastic. Shown are cell tracks after 8-hours of movement (top panel) and velocity distribution (bottom).

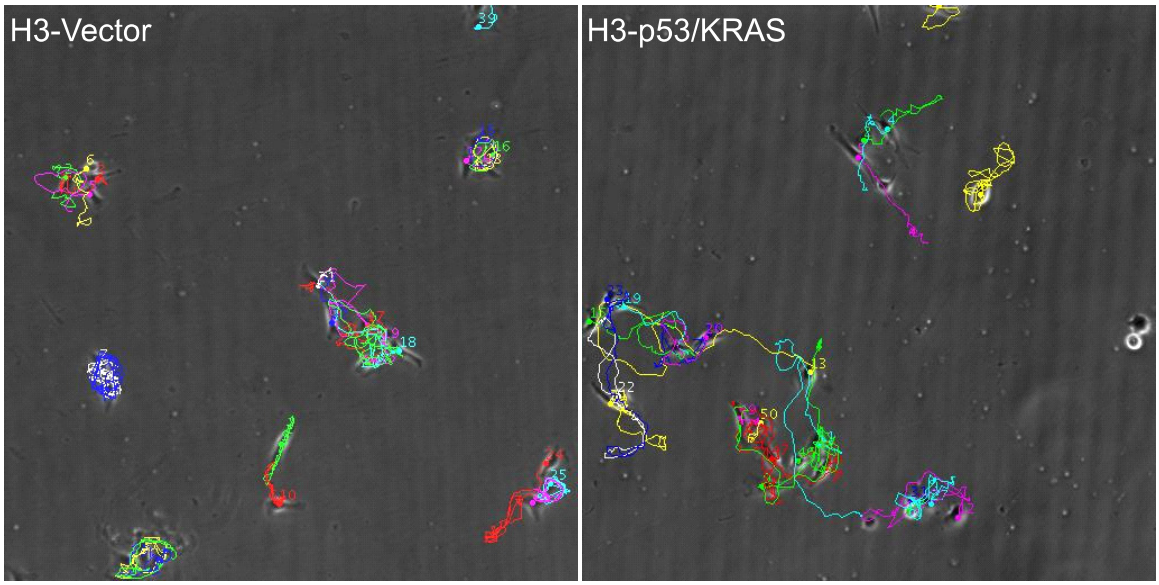

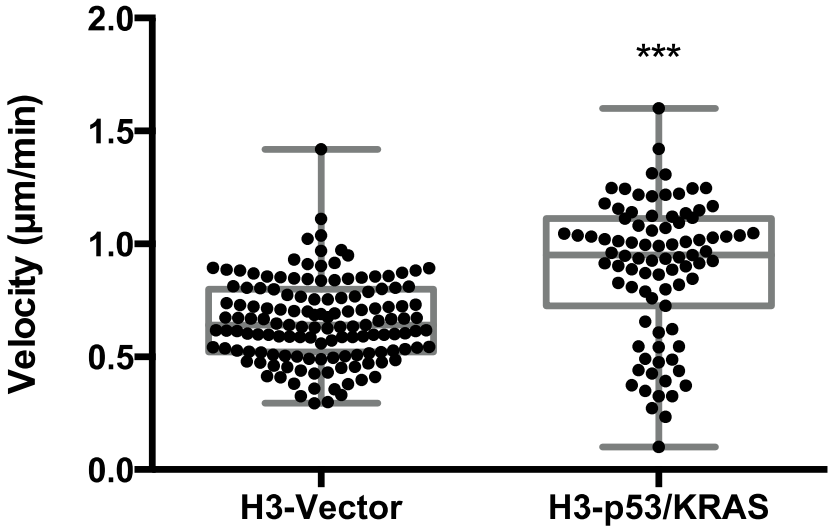

Figure 3.5: Highly migratory cells are a rare subpopulation. Phase contrast images showing the presence of a morphologically distinct highly migratory cell in unselected HBEC4-Snail cells. Inset shows a cell with identical morphology to H4-Snail-HM cells. 25 adjacent fields at 200x total magnification.

Figure 3.6: Heat map from microarray and western blot showing relative abundance of EMT markers in H3mut-Snail/Vector micropore-selected highly migratory cells. Heat map reflects the Log_2 fold-change in transcript levels of highly migratory to unselected cells.

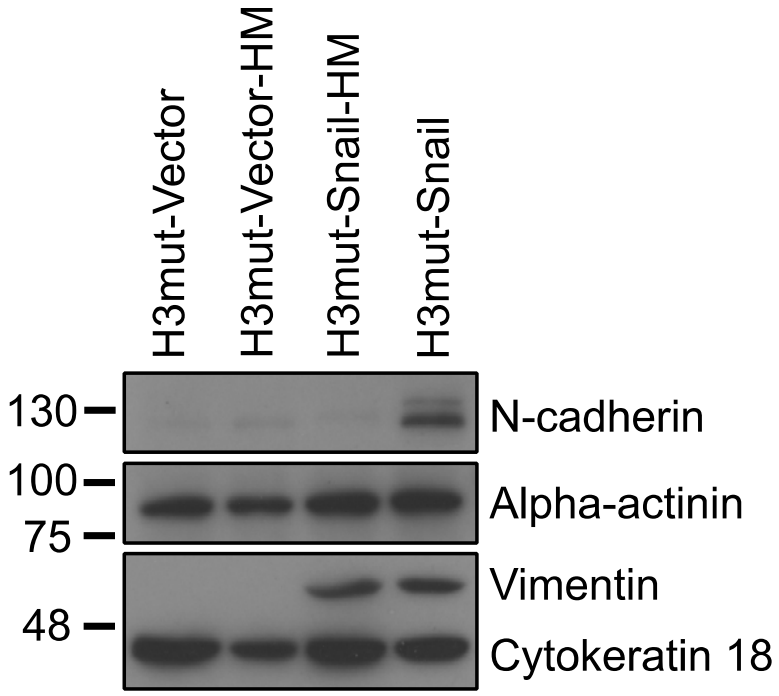

	H3m-Snail-HM	H3-Snail-HM	H4-Snail-HM
E-cadherin	-0.42	0.25	-0.12
Cytokeratin 18	0.08	0.18	0.24
Cytokeratin 26	-0.12	0.18	-0.16
N-cadherin	-1.32	-0.57	-1.97
Vimentin	-0.13	-0.65	-0.35

Log(2) Ratio

Figure 3.7: N-cadherin loss is a common event among micropore-selected highly migratory cells. N-cadherin (*CDH2*) transcript levels are decreased (microarray heatmap) and protein levels are decreased (western blot) in highly migratory cells that express Snail. Heat map reflects the Log_2 fold-change in transcript levels of highly migratory to unselected cells

	H3-Snail-HM	H4-Snail-HM	H3m-Snail-HM	A549-Snail-HM
N-cadherin	-0.57	-1.97	-1.32	-2.31

Log(2) Ratio

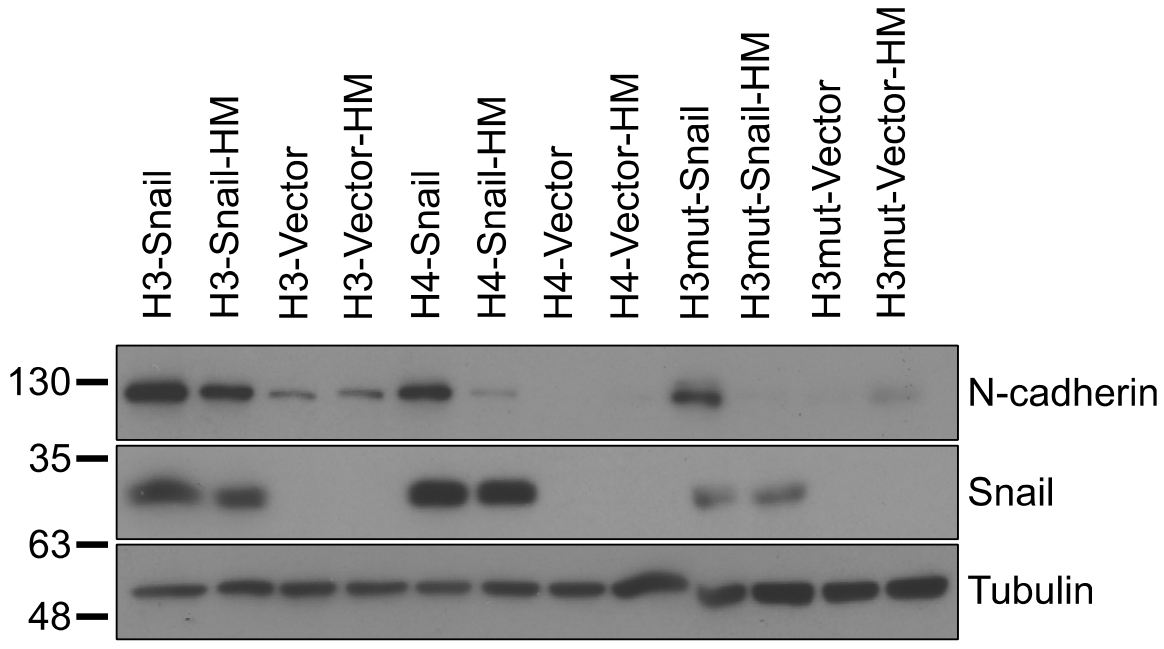

Figure 3.8a: N-cadherin loss is associated with increased cellular speed in high cell density circumstances. H3mut-Snail-HM cells (*CDH2*^{low}) move faster than H3mut-Snail cells (*CDH2*^{hi}). 100x total magnification. Shown are time 0 (left figures) and 5 hours post-scratch (right figures).

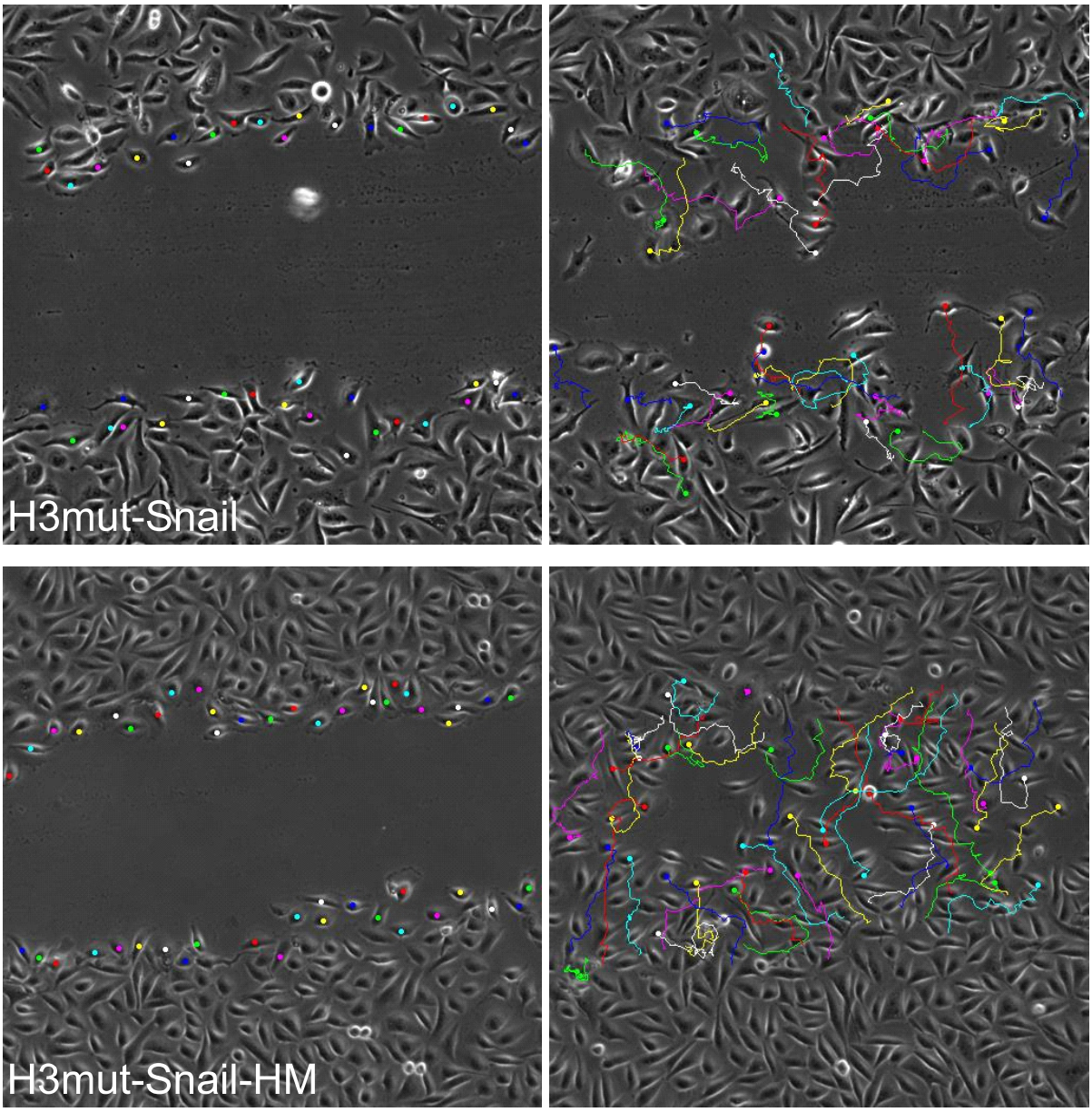

Figure 3.8b: N-cadherin loss is associated with increased cellular speed in high cell density circumstances. H3mut-Snail-HM cells (*CDH2*^{low}) move faster than H3mut-Snail cells (*CDH2*^{hi}). Note: both H3mut-Vector/H3mut-Vector-HM cells are *CDH2*^{low}.

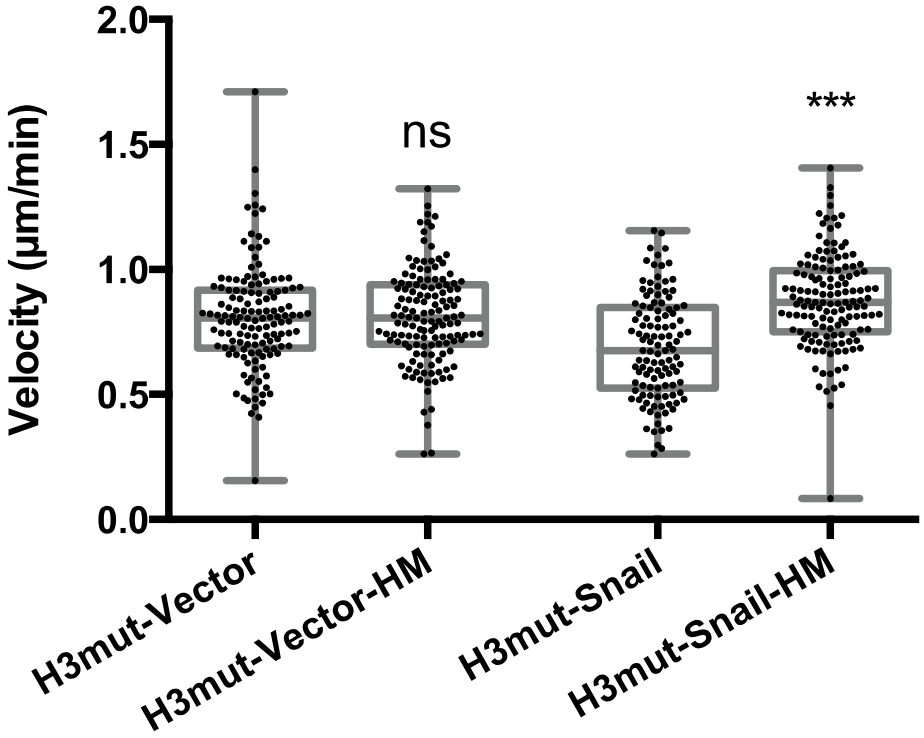

Figure 3.9: The highly migratory phenotype is associated with fewer and smaller adhesion structures in a Snail-dependent manner. Highly migratory Snail cells have a reduced number of focal adhesions (FA) per cell and reduced average adhesion size. In the H4-Snail-HM cells, size is reduced to a level typical of “nascent adhesions” (<1 μm) which have rapid turnover and are typically present in high-mobility cells). 400x total magnification.

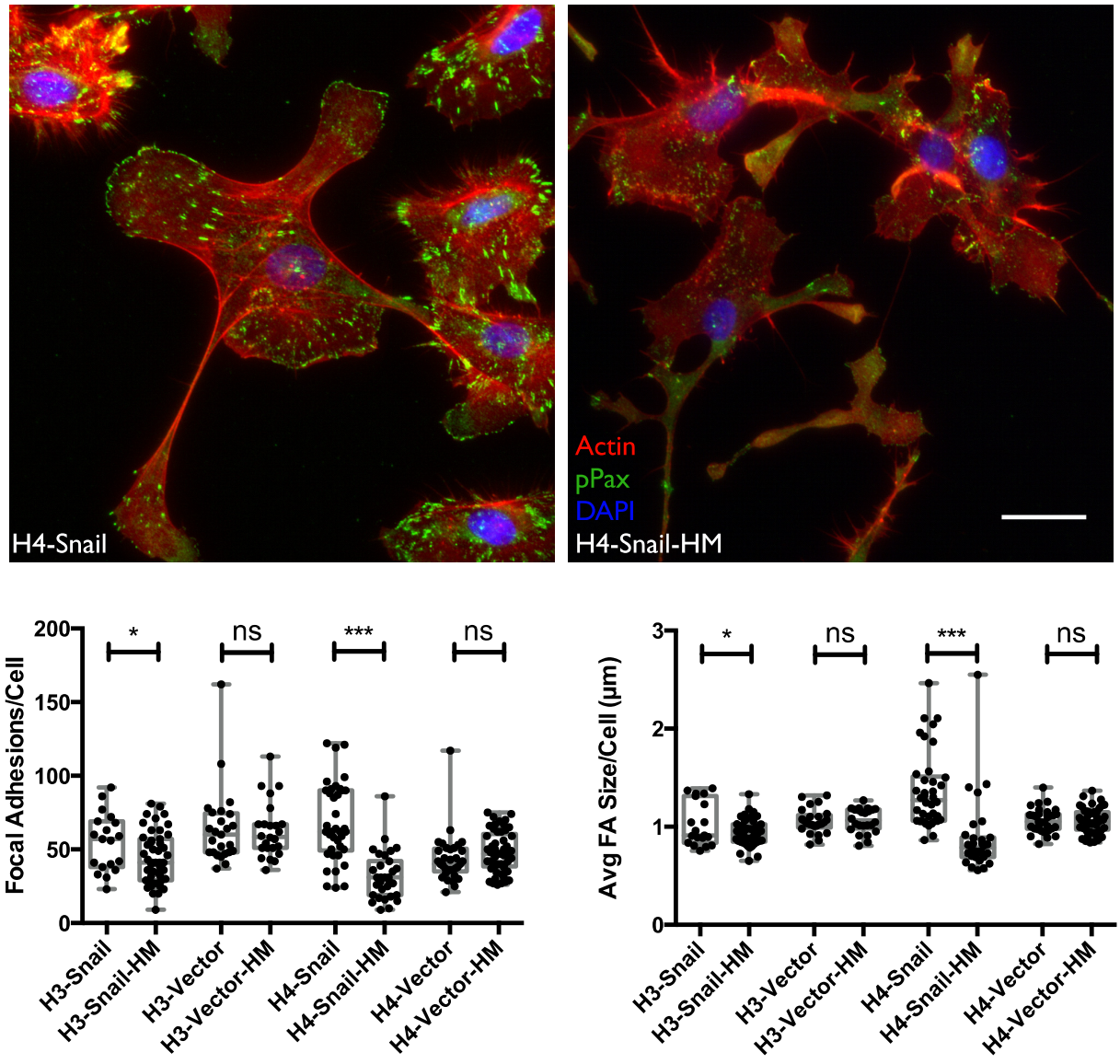

Figure 3.10: Increased lamin A:B ratio is linked to the highly migratory behavior. Western blot and densitometry analysis reveal increased lamin A and decreased lamin B levels, which is typical of cells capable of migrating confined space.

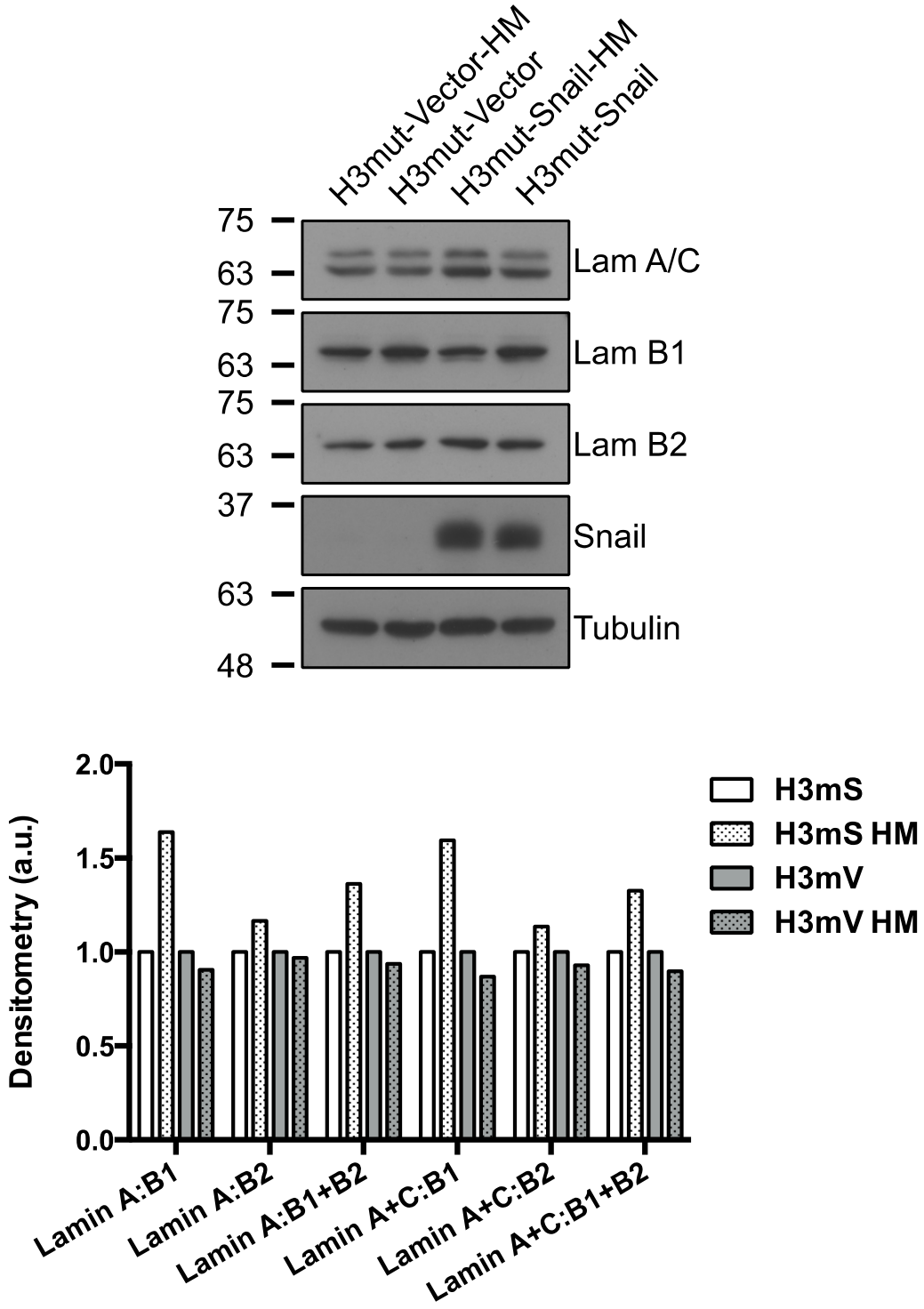

Figure 3.11: miRNA expression pattern matches mRNA expression in highly migratory cells. Previous data show the majority of deregulated mRNA is down-regulated. A similar trend is seen with miRNA, suggesting an alternate form of epigenetic regulation in selected cells. Note: S/V = Snail versus Vector; S-HM/P = Snail-HM versus Snail-Parental (unselected).

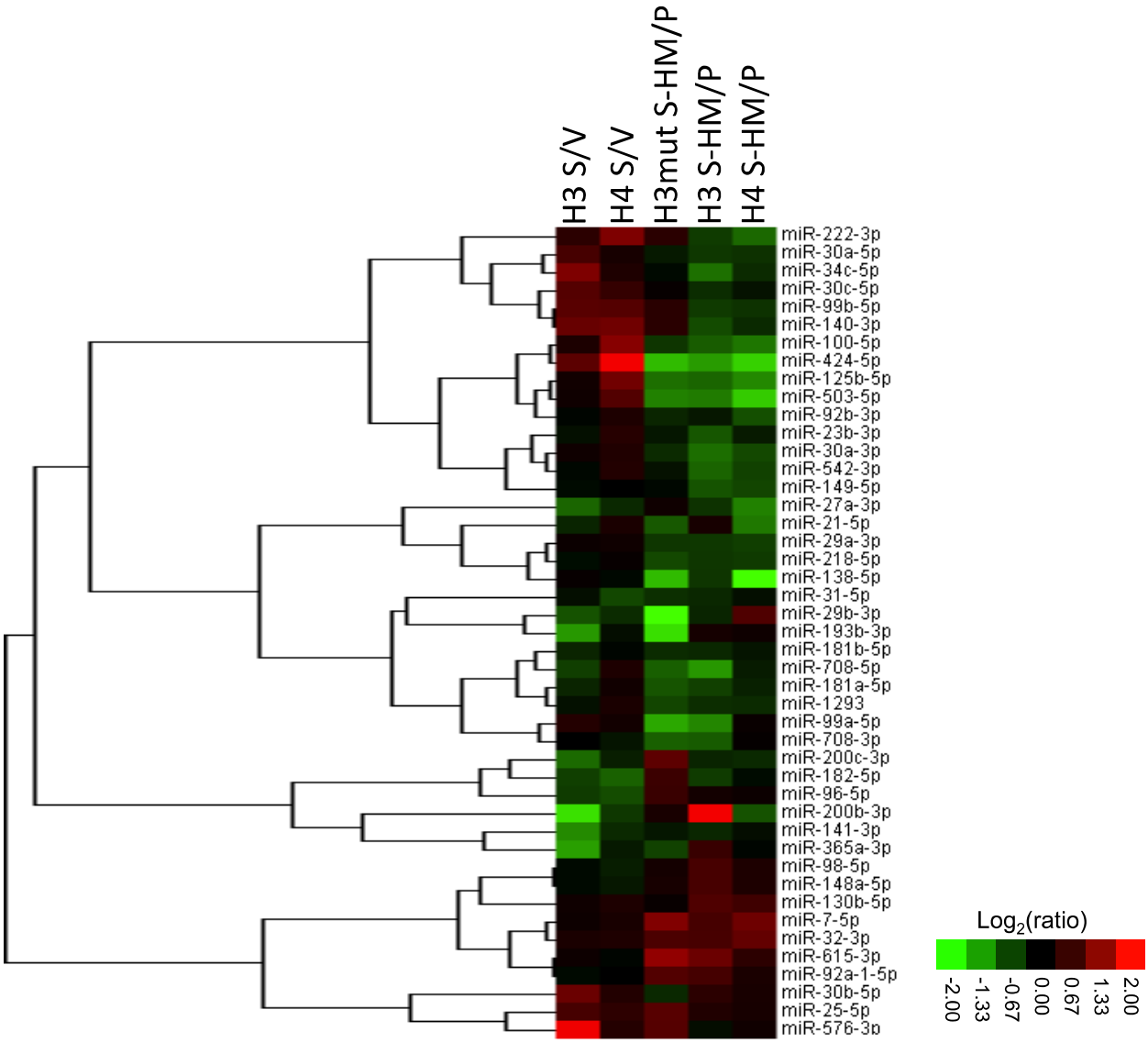

Figure 3.12: Changes in gene expression are more heavily influenced by Snail expression rather than high-versus-low migration. Principle component analysis shows cell lines “organize” based on Snail-versus-vector, and genes related to the highly migratory phenotype have only subtle effects on this arrangement. (HM = highly migratory; LM = low migratory/unselected parental population)

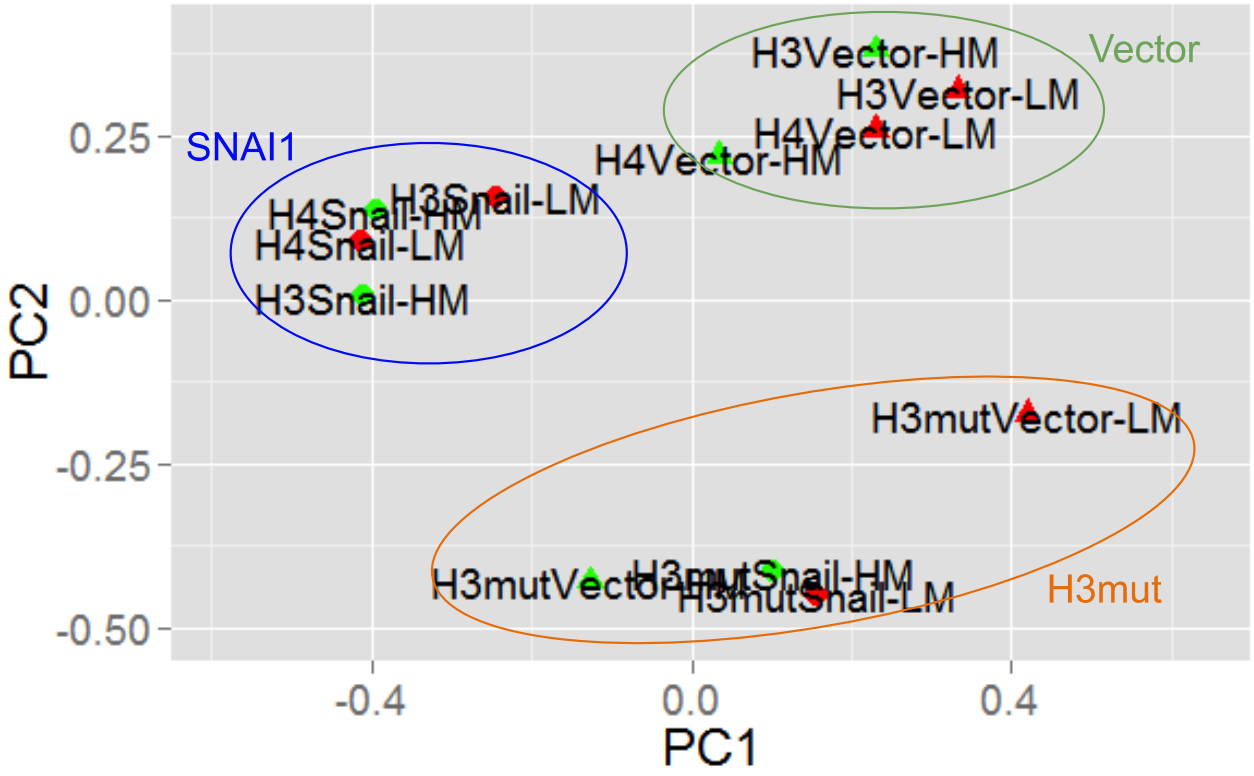

Figure 3.13: Cytokine profile in highly migratory cells. Heat map showing relative expression of secreted cytokines (green is up- and red is down-regulated).

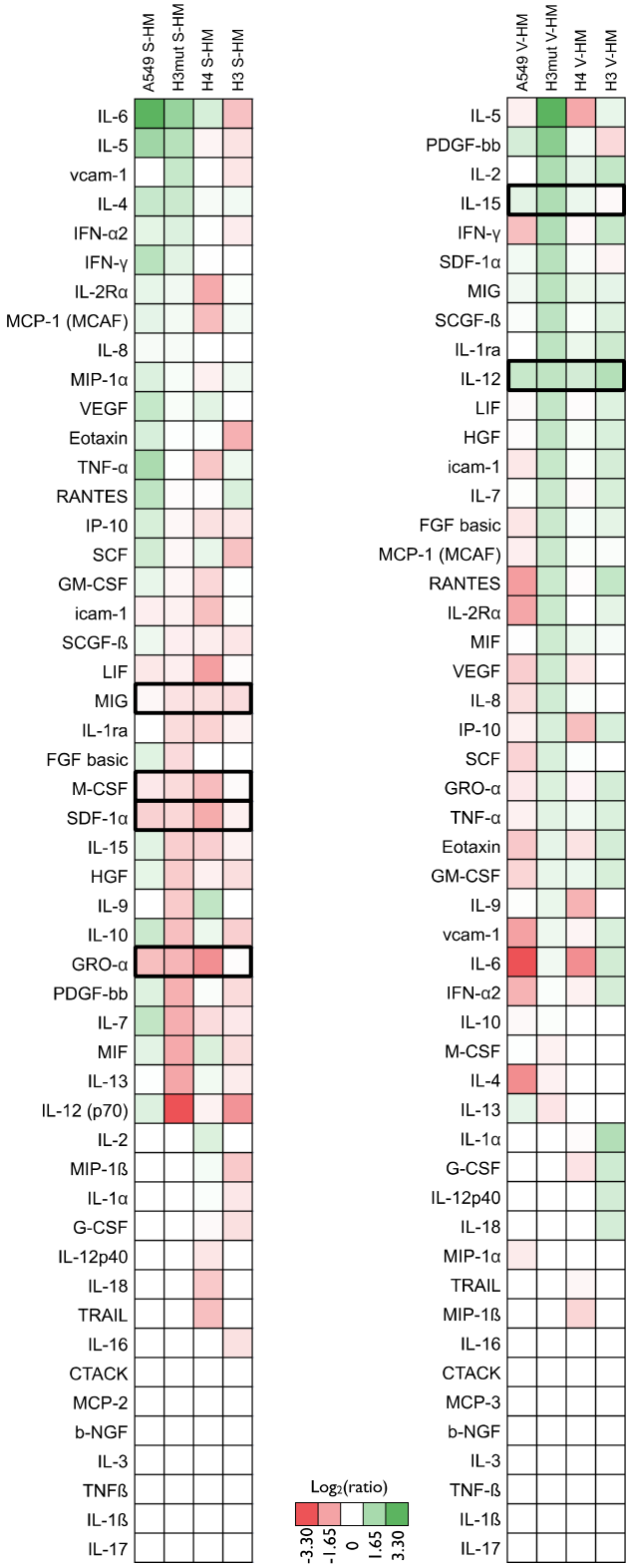

Figure 3.14a: Reduction in anchorage-independent cell growth as a result of micropore selection. H3mut-Snail cells have robust colony formation in soft agar, a trait that is lost in highly migratory cells. This suggests a “grow or go” phenotype. Representative images from 10 replicate wells per cell line.

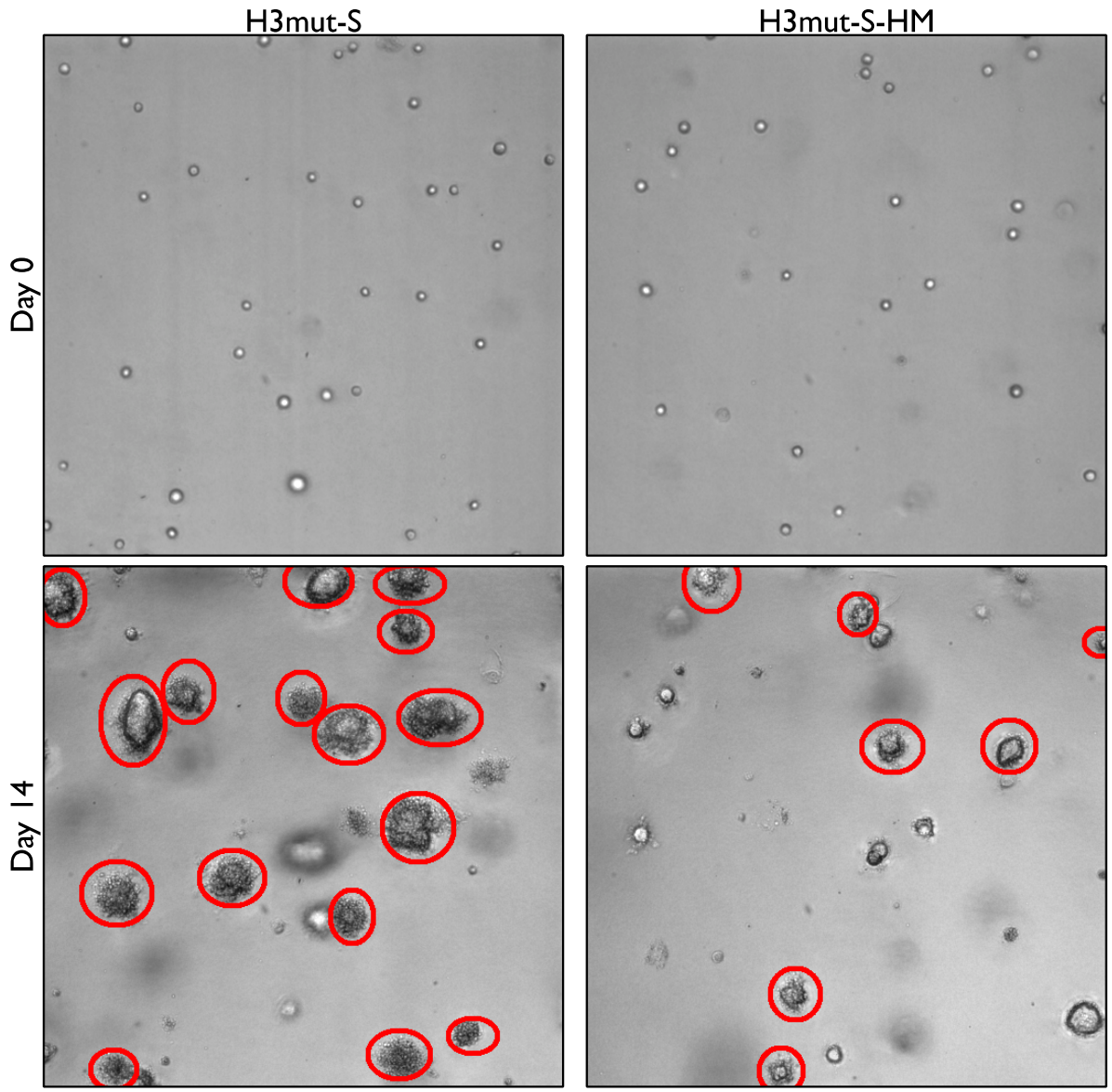

Figure 3.14b: Reduction in anchorage-independent cell growth as a result of micropore selection. H3mut-Vector cells have no change in anchorage-independent cell growth following micropore selection.

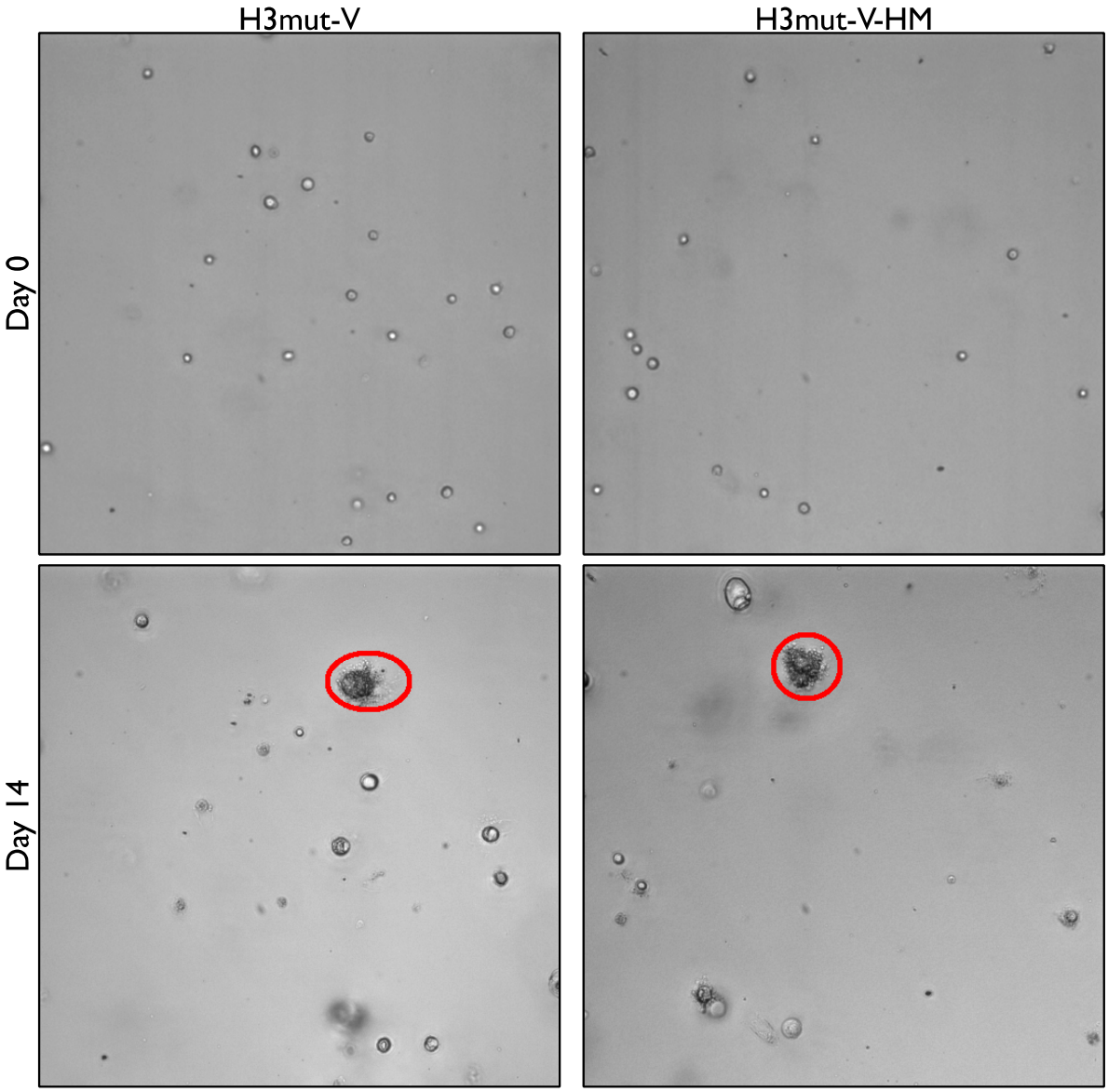

Figure 3.14c: Reduction in anchorage-independent cell growth as a result of micropore selection. H3mut-Snail cells have robust colony formation in soft agar, a trait that is lost in highly migratory cells. This suggests a “grow or go” phenotype. No change in AIG was observed in H3mut-Vector cells following micropore selection. Error bars are SD.

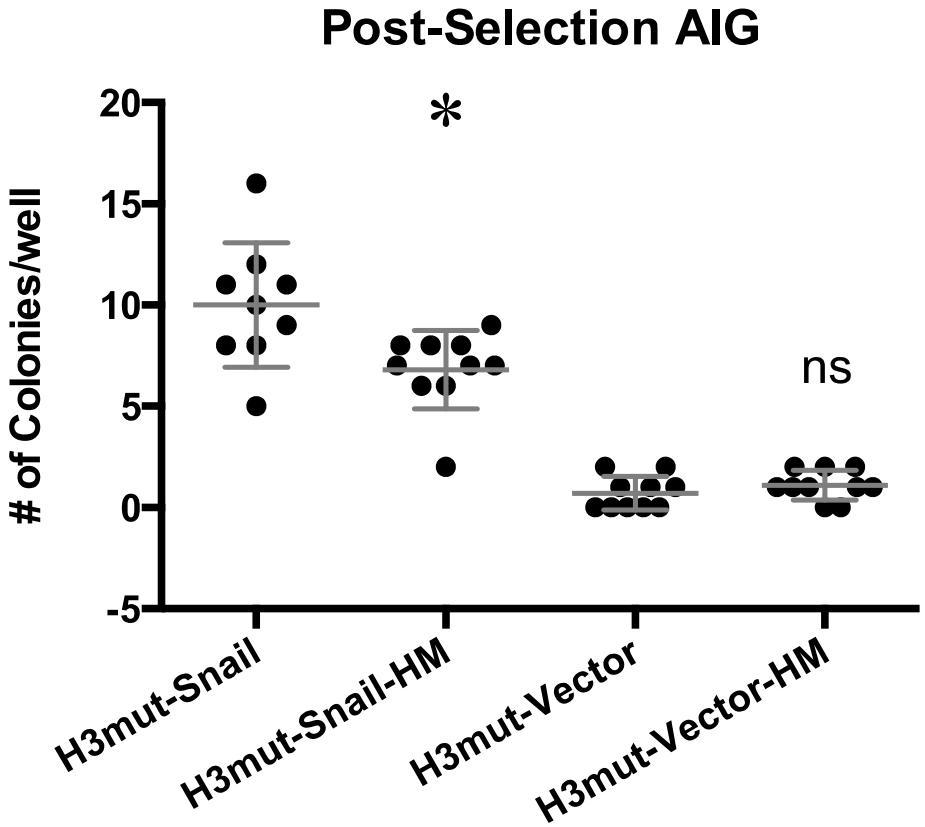

Figure 3.15: Time-lapse fluorescent imaging reveals individual cells within a colony formed by micropore-selected cells move quickly. Colonies grown in agar were stained with Hoechst (DNA) after 21 days and imaged for 10 hours at 5 minute intervals by time-lapse fluorescent microscopy. Tracking was performed in ImageJ using the manual tracking plugin.

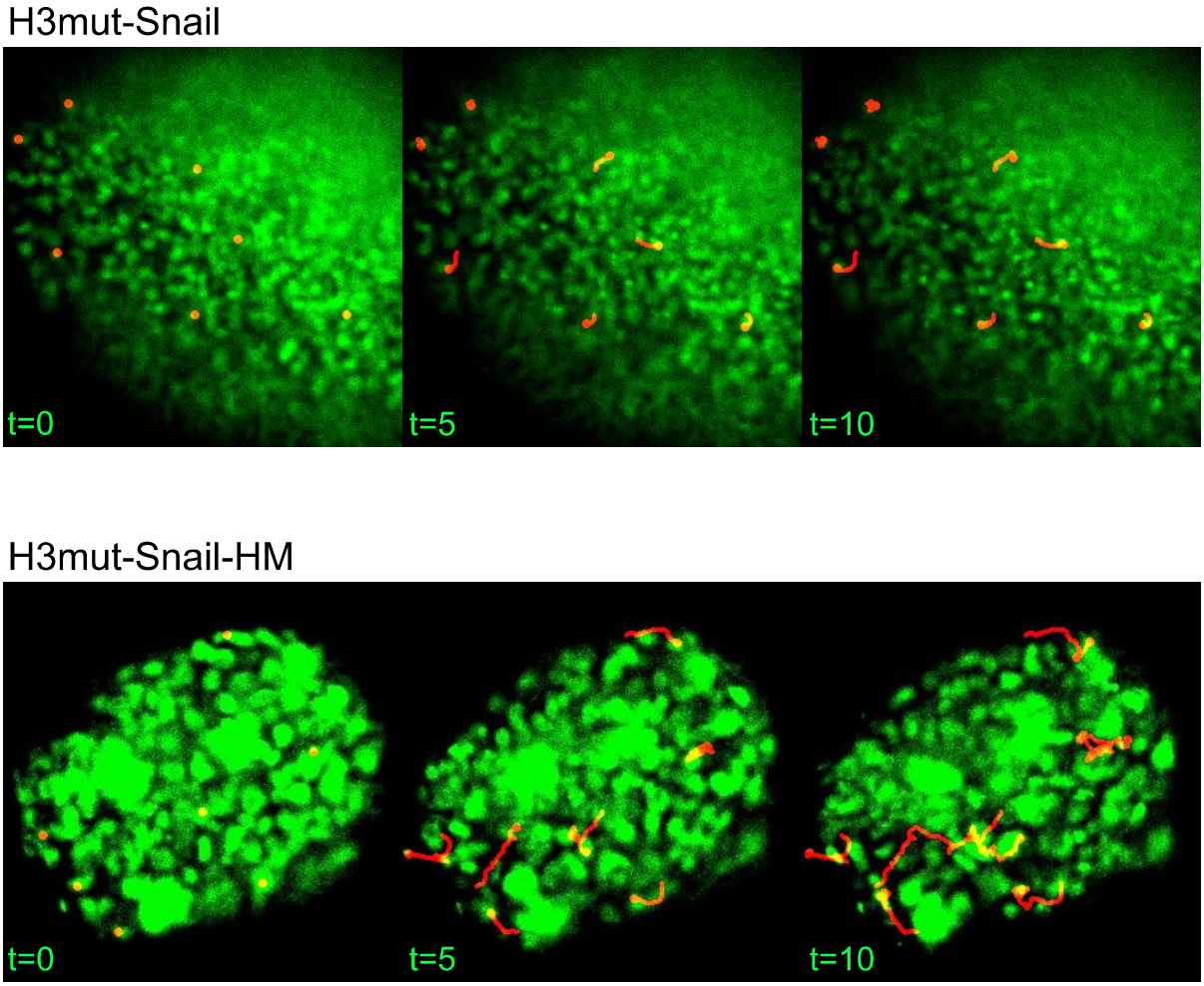

Figure 3.16: Cytoskeleton phospho-protein array. Phospho-protein antibody array focused on various cytoskeleton proteins show differential expression in Snail-HM cells. Points on graph represent the fold-change in phospho-proteins of 67 different proteins. H3mut-Snail-HM cells show an overall decrease whereas H4-Snail-HM show an overall increase in phosphorylation (blue lines).

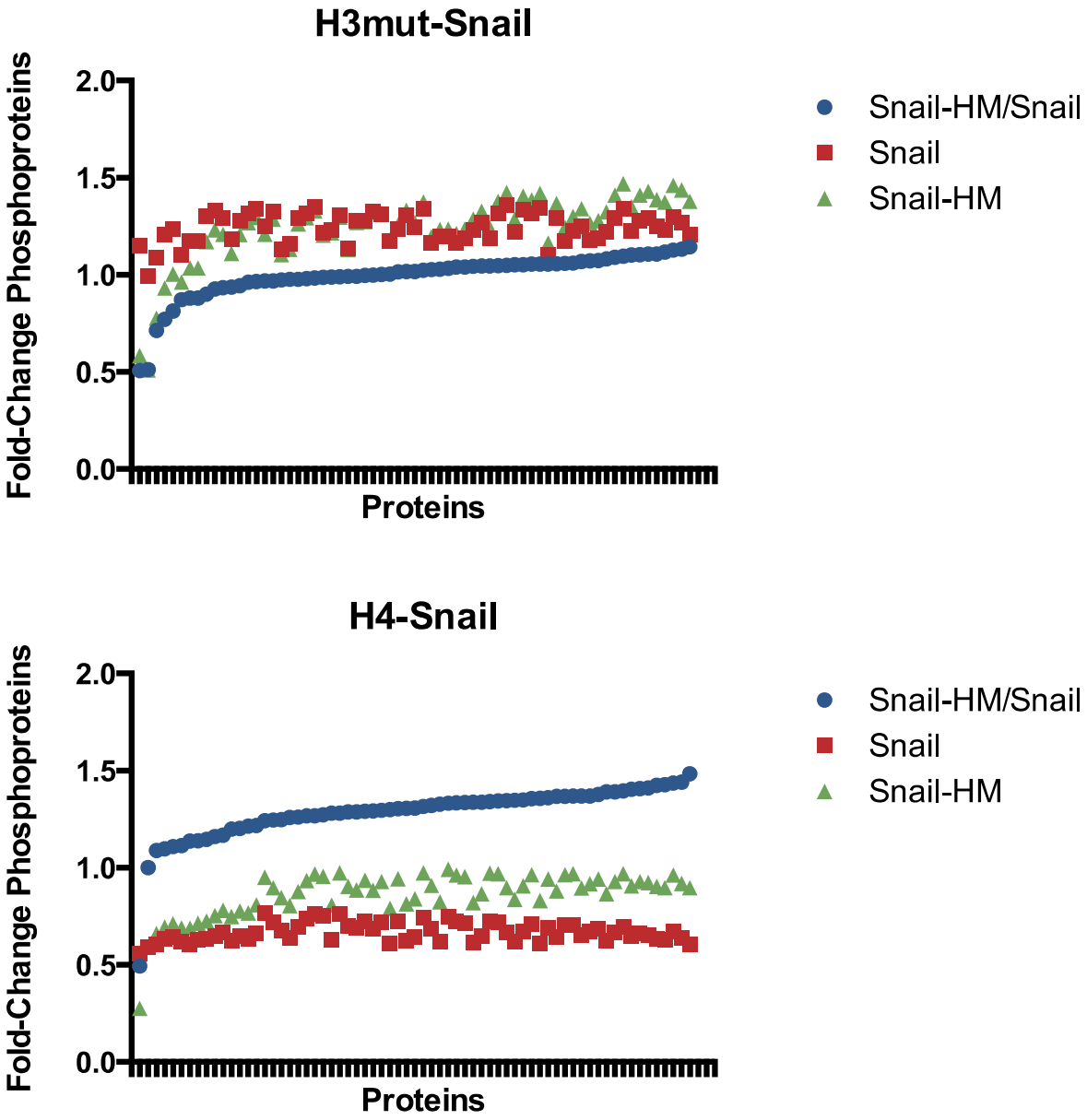

Table 3.1: Table showing fold-change in cytoskeleton protein phosphorylation and protein function (Uniprot).

Phospho-protein	H4-Snail Fold Change	H3m-Snail Fold Change	Function (Uniprot)
MKK3/MAP2K 3 (pThr222)	0.50	0.51	Dual specificity kinase; activated by cytokines and environmental stress;
CrkL (pTyr207)	1.24	1.14	May mediate the transduction of intracellular signals;
CrkII (pTyr221)	1.27	1.13	Mediates attachment-induced MAPK8 activation, membrane ruffling, and cell motility in a Rac-dependent manner;
Merlin (pSer518)	1.29	1.13	Probable regulator of hippo signaling; may act as a membrane stabilizing protein;
Filamin A (pSer2152)	1.28	1.10	Promotes orthogonal branching of actin filaments; links actin to membrane glycoproteins;
Rho/Rac GEF (pSer885)	1.33	1.12	Activates Rho-family GTPases; may be involved in epithelial barrier permeability, cell motility and polarization, cancer, etc;
ERK1 (pThr202)	1.32	1.11	Essential component in the MAP kinase signal transduction pathway;
Cortactin (pTyr466) (pTyr421)	1.33 1.31	1.11 1.14	Contributes to actin cytoskeleton organization and cell shape; Helps in lamellipodium formation and migration.
MEK-2 (pThr394)	1.33	1.10	Catalyzes concomitant phosphorylation of Thr and Tyr residues on MAP kinases. Activates ERK1 and ERK2.

Figure 3.17: Highly migratory cells show heterogeneity in activated GTPase levels. Heat map showing fold-change in levels of GTP-bound (active) RhoA, Rac1, and Cdc42 in Snail versus vector (top) or Highly Migratory versus Unselected (bottom) cells as determined by GLISA (ELISA-type assay that uses Rhotekin or p21-activated kinase as affinity capture reagents for GTP-bound RhoA or Rac1/Cdc42, respectively). Green denotes increased and red denotes reduced levels of activation.

	RhoA	Rac1	Cdc42
H3-Snail	1.31	1.39	0.97
H3mut-Snail	0.83	1.56	0.78
H4-Snail	1.03	1.43	1.27

	RhoA	Rac1	Cdc42
H3 Snail-HM	0.78	0.82	0.72
H3 Vector-HM	0.80	1.10	0.85
H3m Snail-HM	0.99	1.10	1.31
H3m Vector-HM	0.80	1.28	1.02
H4 Snail-HM	1.32	0.91	0.69
H4 Vector-HM	0.98	1.04	0.70

Table 3.2: Table showing five different inhibitors of various points in the motility program, along with their target and IC_{50} value.

Inhibitor	Target	IC_{50}
ML-7	Myosin light chain kinase (MLCK)	6 μM
Y-27632	Rho associated kinase (ROCK)	0.8 μM
Rhosin/G04	RhoA guanine nucleotide exchange factor	10 μM
NSC-23766	Rac1 guanine nucleotide exchange factor	50 μM

Figure 3.18: Determining the optimal concentration of inhibitor using a proliferation assay. Dose-dependent changes in proliferation rate as a result of incubation with compounds affecting RhoA (Rhosin), Rac1 (NSC-23766), ROCK (Y-27632), and MLCK (ML-7).

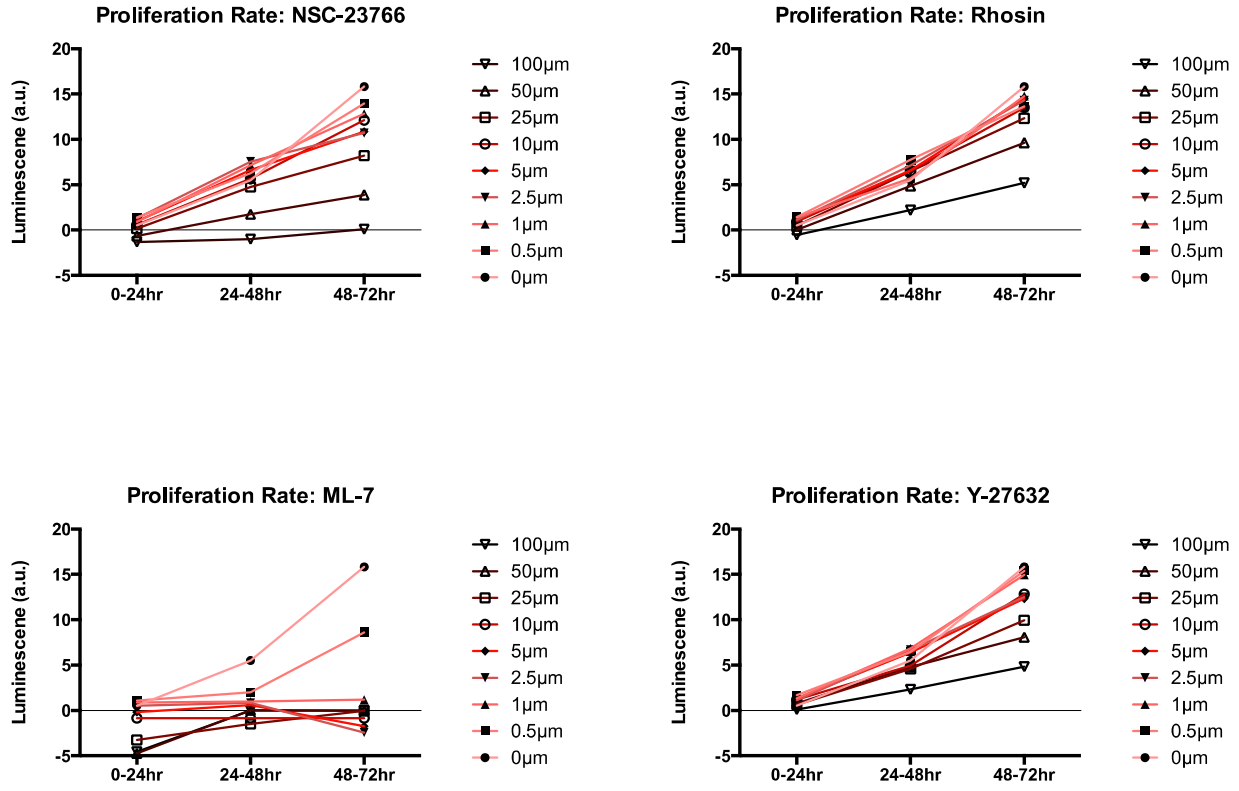

Figure 3.19: Inhibitors have differential effects on migration. Quantitative results from migration assays using inhibitors to enhance or attenuate migration in HM and unselected cells. Inhibition of Rac1 (NSC-23766) results in decreased migration. Inhibition of RhoA (Rhosin) or ROCK (Y-27632), negative regulators of the Rac1 pathway, enhance migration at low inhibitor concentrations.

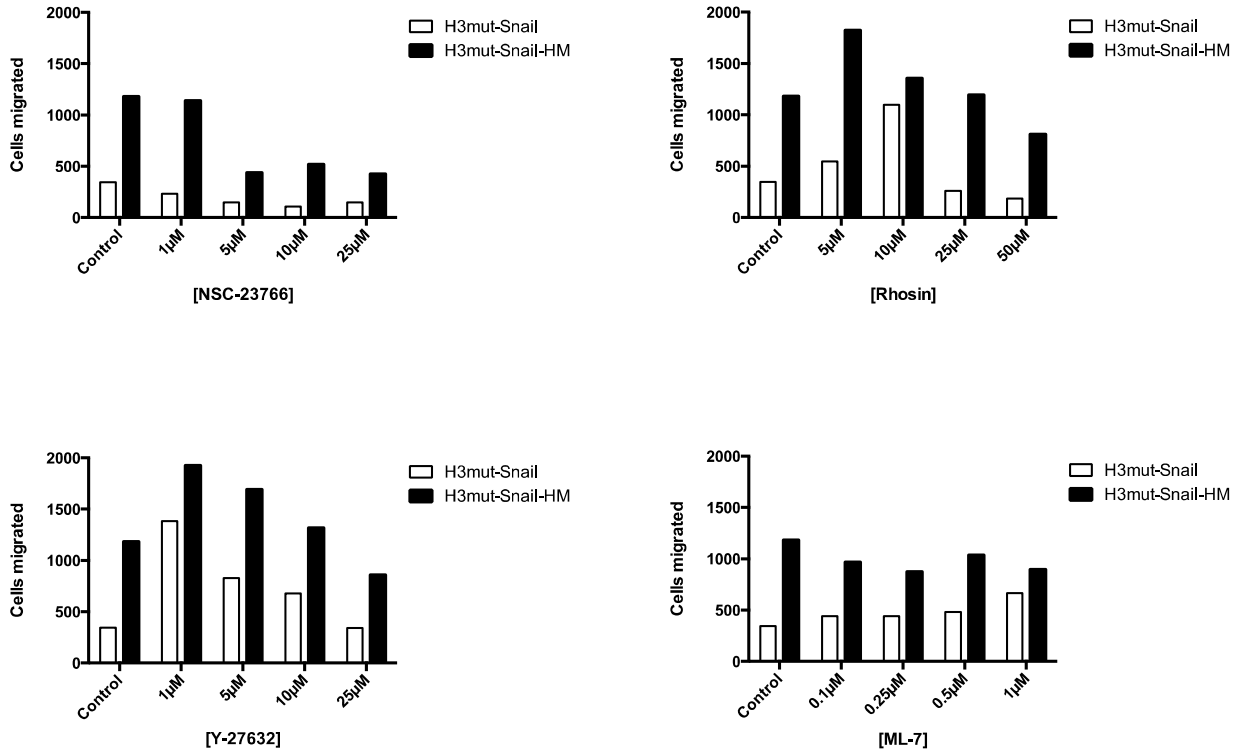

Figure 3.20a: Cortactin (*CTTN*) is deregulated in cancer patient samples. Data from The Cancer Genome Atlas (TCGA) shows *CTTN* deregulation in several cancers types, including lung squamous cell carcinoma.

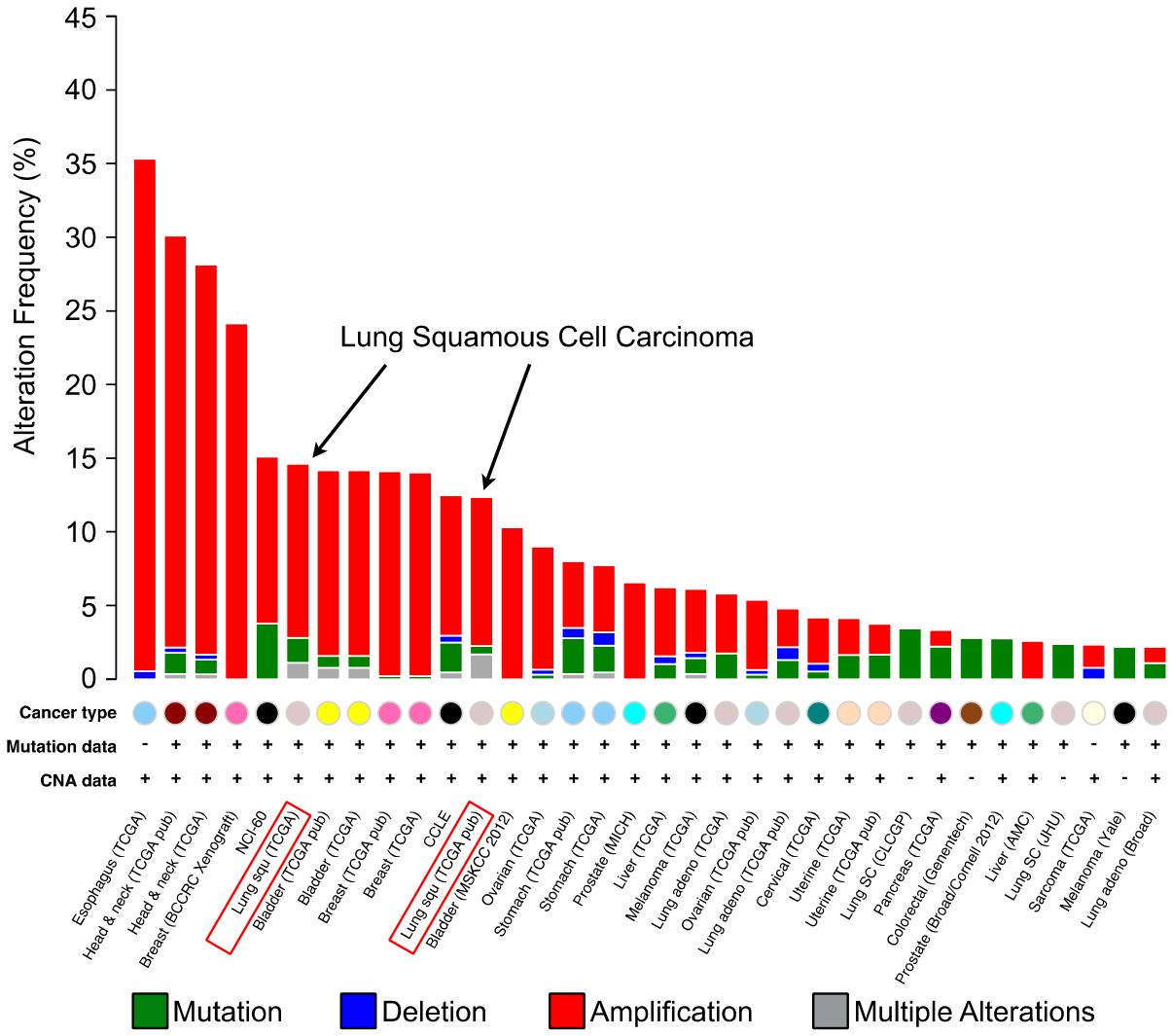

Figure 3.20b: Cortactin (*CTTN*) is deregulated in cancer patient samples. Data from The Cancer Genome Atlas (TCGA) shows the median disease free survival in lung squamous cell carcinoma is significantly reduced in patients with *CTTN* altercation.

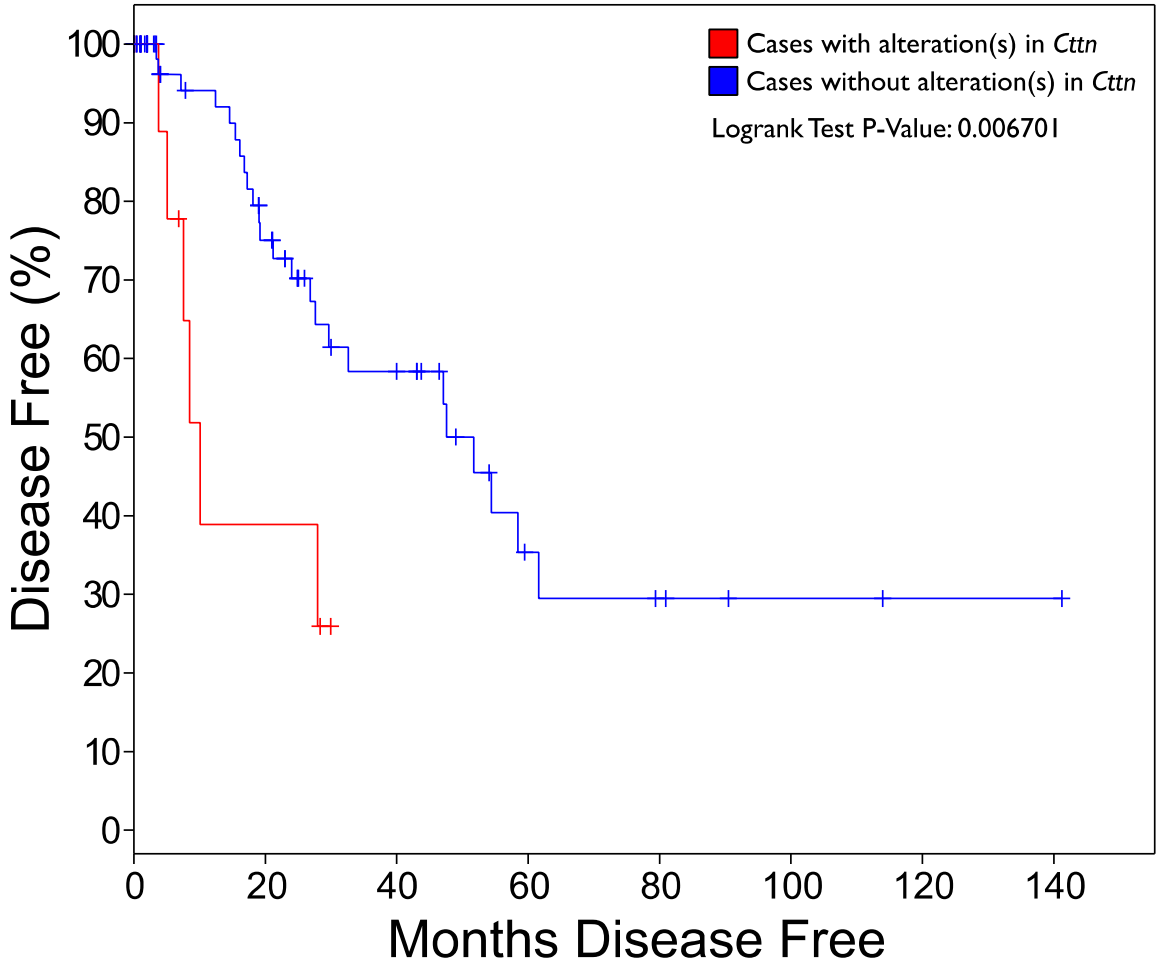

Cases	# of Total Cases	# of Cases Relapsed	Median time disease free
w/ *CTTN* alteration	16	6	10.05 months
w/o *CTTN* alteration	71	24	51.74 months

Figure 3.21: Parallel progression model for lung cancer as it relates to motility. Genes are activated very early on in premalignancy that simultaneously facilitate tumorigenesis and drive enhanced motility. Adapted from Sanchez-Garcia *NEJM* 2009. Reproduced with permission from (31) Copyright Massachusetts Medical Society.

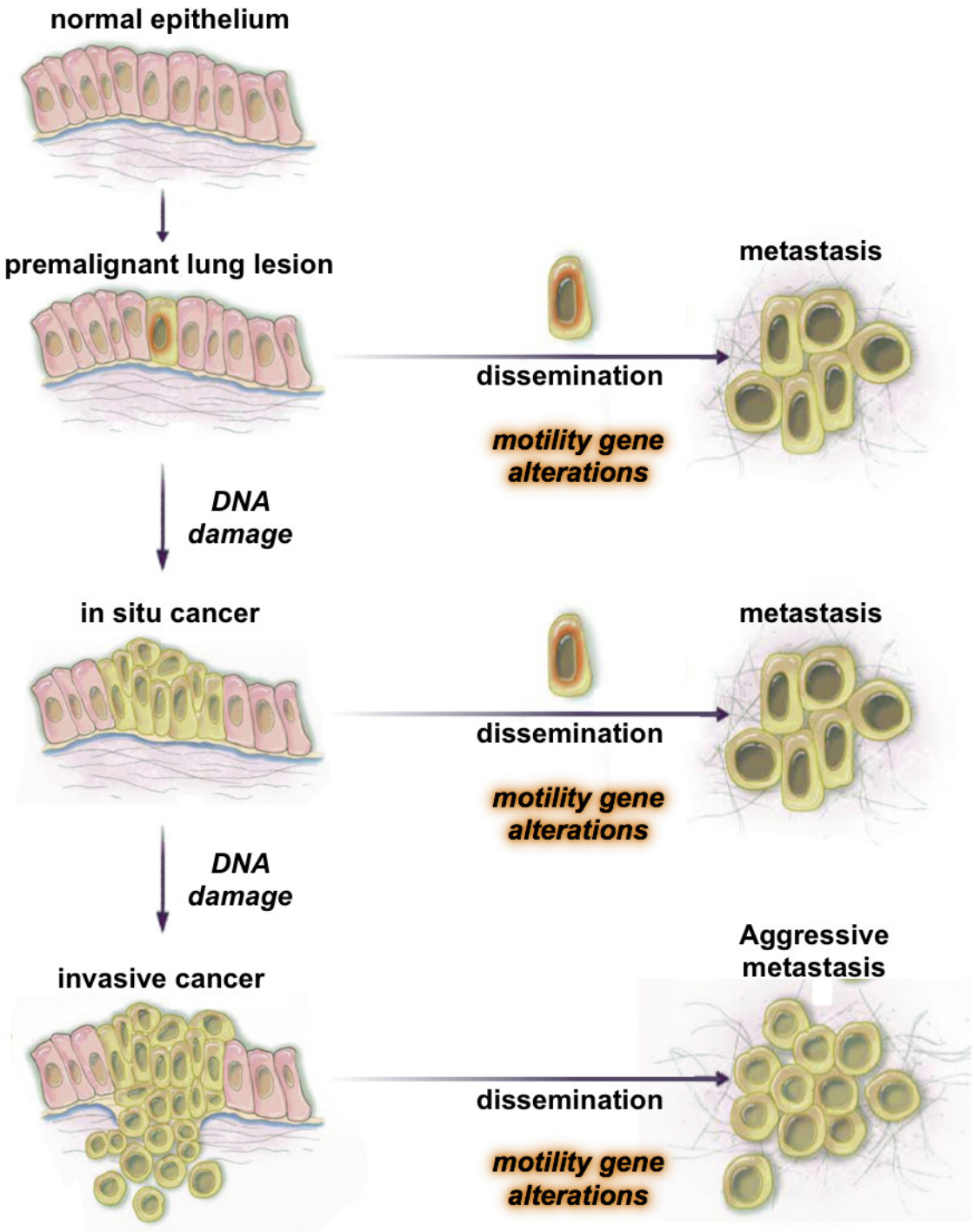

References

1. Rhim AD, Mirek ET, Aiello NM, Maitra A, Bailey JM, McAllister F, Reichert M, Beatty GL, Rustgi AK, et al. EMT and dissemination precede pancreatic tumor formation. Cell 2012;148(1-2):349-61.
2. Podsypanina K, Du YC, Jechlinger M, Beverly LJ, Hambardzumyan D, Varmus H. Seeding and propagation of untransformed mouse mammary cells in the lung. Science 2008;321(5897):1841-4.
3. Husemann Y, Geigl JB, Schubert F, Musiani P, Meyer M, Burghart E, Forni G, Eils R, Fehm T, et al. Systemic spread is an early step in breast cancer. Cancer Cell 2008;13(1):58-68.
4. Kalluri R, Weinberg RA. The basics of epithelial-mesenchymal transition. J Clin Invest 2009;119(6):1420-8.
5. Gardel ML, Schneider IC, Aratyn-Schaus Y, Waterman CM. Mechanical integration of actin and adhesion dynamics in cell migration. Annu Rev Cell Dev Biol 2010;26:315-33.
6. Zaidel-Bar R, Ballestrem C, Kam Z, Geiger B. Early molecular events in the assembly of matrix adhesions at the leading edge of migrating cells. J Cell Sci 2003;116(Pt 22):4605-13.
7. Rowat AC, Jaalouk DE, Zwerger M, Ung WL, Eydelnant IA, Olins DE, Olins AL, Herrmann H, Weitz DA, et al. Nuclear Envelope Composition Determines the Ability of Neutrophil-type Cells to Passage through Micron-scale Constrictions. Journal of Biological Chemistry 2013;288(12):8610-18.
8. Davidson PM, Denais C, Bakshi MC, Lammerding J. Nuclear Deformability Constitutes a Rate-Limiting Step During Cell Migration in 3-D Environments. Cell Mol Bioeng 2014;7(3):293-306.
9. Harada T, Swift J, Irianto J, Shin JW, Spinler KR, Athirasala A, Diegmiller R, Dingal PCDP, Ivanovska IL, et al. Nuclear lamin stiffness is a barrier to 3D

migration, but softness can limit survival. Journal of Cell Biology 2014;204(5):669-82.

10. Liu YJ, Le Berre M, Lautenschlaeger F, Maiuri P, Callan-Jones A, Heuze M, Takaki T, Voituriez R, Piel M. Confinement and low adhesion induce fast amoeboid migration of slow mesenchymal cells. Cell 2015;160(4):659-72.

11. Welch MD. Cell migration, freshly squeezed. Cell 2015;160(4):581-2.

12. Liclican EL, Walser TC, Hazra S, Krysan K, Park SJ, Pagano PC, Gardner BK, Larsen JE, Minna JD, et al. Loss of miR125a expression in a model of K-ras-dependent pulmonary premalignancy. Cancer prevention research 2014;7(8):845-55.

13. Gil-Henn H, Patsialou A, Wang Y, Warren MS, Condeelis JS, Koleske AJ. Arg/Abl2 promotes invasion and attenuates proliferation of breast cancer in vivo. Oncogene 2013;32(21):2622-30.

14. Patsialou A, Wang Y, Lin J, Whitney K, Goswami S, Kenny PA, Condeelis JS. Selective gene-expression profiling of migratory tumor cells in vivo predicts clinical outcome in breast cancer patients. Breast cancer research : BCR 2012;14(5):R139.

15. Woollard SM, Li H, Singh S, Yu F, Kanmogne GD. HIV-1 induces cytoskeletal alterations and Rac1 activation during monocyte-blood-brain barrier interactions: modulatory role of CCR5. Retrovirology 2014;11:20.

16. Mader CC, Oser M, Magalhaes MA, Bravo-Cordero JJ, Condeelis J, Koleske AJ, Gil-Henn H. An EGFR-Src-Arg-cortactin pathway mediates functional maturation of invadopodia and breast cancer cell invasion. Cancer Res 2011;71(5):1730-41.

17. Magalhaes MA, Larson DR, Mader CC, Bravo-Cordero JJ, Gil-Henn H, Oser M, Chen X, Koleske AJ, Condeelis J. Cortactin phosphorylation regulates cell invasion through a pH-dependent pathway. J Cell Biol 2011;195(5):903-20.

18. Arnoux V, Nassour M, L'Helgoualc'h A, Hipskind RA, Savagner P. Erk5 controls Slug expression and keratinocyte activation during wound healing. Molecular biology of the cell 2008;19(11):4738-49.

19. Howard S, Deroo T, Fujita Y, Itasaki N. A positive role of cadherin in Wnt/beta-catenin signalling during epithelial-mesenchymal transition. PLoS One 2011;6(8):e23899.

20. Hay E, Laplantine E, Geoffroy V, Frain M, Kohler T, Muller R, Marie PJ. N-cadherin interacts with axin and LRP5 to negatively regulate Wnt/beta-catenin signaling, osteoblast function, and bone formation. Mol Cell Biol 2009;29(4):953-64.

21. Zhang J, Shemezis JR, McQuinn ER, Wang J, Sverdlov M, Chenn A. AKT activation by N-cadherin regulates beta-catenin signaling and neuronal differentiation during cortical development. Neural development 2013;8:7.

22. Cancer Genome Atlas Research N. Comprehensive genomic characterization of squamous cell lung cancers. Nature 2012;489(7417):519-25.

23. Radisky DC, Levy DD, Littlepage LE, Liu H, Nelson CM, Fata JE, Leake D, Godden EL, Albertson DG, et al. Rac1b and reactive oxygen species mediate MMP-3-induced EMT and genomic instability. Nature 2005;436(7047):123-7.

24. Stallings-Mann ML, Waldmann J, Zhang Y, Miller E, Gauthier ML, Visscher DW, Downey GP, Radisky ES, Fields AP, et al. Matrix metalloproteinase induction of Rac1b, a key effector of lung cancer progression. Sci Transl Med 2012;4(142):142ra95.

25. Ishii H, Saitoh M, Sakamoto K, Kondo T, Katoh R, Tanaka S, Motizuki M, Masuyama K, Miyazawa K. Epithelial splicing regulatory proteins 1 (ESRP1) and 2 (ESRP2) suppress cancer cell motility via different mechanisms. J Biol Chem 2014;289(40):27386-99.

26. Peter M, Nakagawa J, Doree M, Labbe JC, Nigg EA. In vitro disassembly of the nuclear lamina and M phase-specific phosphorylation of lamins by cdc2 kinase. Cell 1990;61(4):591-602.

27. Heald R, McKeon F. Mutations of phosphorylation sites in lamin A that prevent nuclear lamina disassembly in mitosis. Cell 1990;61(4):579-89.

28. Kochin V, Shimi T, Torvaldson E, Adam SA, Goldman A, Pack CG, Melo-Cardenas J, Imanishi SY, Goldman RD, et al. Interphase phosphorylation of lamin A. J Cell Sci 2014;127(Pt 12):2683-96.

29. Edens LJ, Levy DL. cPKC regulates interphase nuclear size during Xenopus development. J Cell Biol 2014;206(4):473-83.

30. Hong SH, Ren L, Mendoza A, Eleswarapu A, Khanna C. Apoptosis resistance and PKC signaling: distinguishing features of high and low metastatic cells. Neoplasia 2012;14(3):249-58.

31. Sanchez-Garcia I. The crossroads of oncogenesis and metastasis. N Engl J Med 2009;360(3):297-9.

32. Cerami E, Gao J, Dogrusoz U, Gross BE, Sumer SO, Aksoy BA, Jacobsen A, Byrne CJ, Heuer ML, et al. The cBio cancer genomics portal: an open platform for exploring multidimensional cancer genomics data. Cancer Discov 2012;2(5):401-4.

33. Gao J, Aksoy BA, Dogrusoz U, Dresdner G, Gross B, Sumer SO, Sun Y, Jacobsen A, Sinha R, et al. Integrative analysis of complex cancer genomics and clinical profiles using the cBioPortal. Science signaling 2013;6(269):pl1.